

Study of III-V semiconductor nanostructures by cross-sectional scanning tunneling microscopy

Citation for published version (APA):

Offermans, P. (2005). *Study of III-V semiconductor nanostructures by cross-sectional scanning tunneling microscopy*. [Phd Thesis 1 (Research TU/e / Graduation TU/e), Applied Physics and Science Education]. Technische Universiteit Eindhoven. <https://doi.org/10.6100/IR595006>

DOI:

[10.6100/IR595006](https://doi.org/10.6100/IR595006)

Document status and date:

Published: 01/01/2005

Document Version:

Publisher's PDF, also known as Version of Record (includes final page, issue and volume numbers)

Please check the document version of this publication:

- A submitted manuscript is the version of the article upon submission and before peer-review. There can be important differences between the submitted version and the official published version of record. People interested in the research are advised to contact the author for the final version of the publication, or visit the DOI to the publisher's website.
- The final author version and the galley proof are versions of the publication after peer review.
- The final published version features the final layout of the paper including the volume, issue and page numbers.

[Link to publication](#)

General rights

Copyright and moral rights for the publications made accessible in the public portal are retained by the authors and/or other copyright owners and it is a condition of accessing publications that users recognise and abide by the legal requirements associated with these rights.

- Users may download and print one copy of any publication from the public portal for the purpose of private study or research.
- You may not further distribute the material or use it for any profit-making activity or commercial gain
- You may freely distribute the URL identifying the publication in the public portal.

If the publication is distributed under the terms of Article 25fa of the Dutch Copyright Act, indicated by the "Taverne" license above, please follow below link for the End User Agreement:

www.tue.nl/taverne

Take down policy

If you believe that this document breaches copyright please contact us at:

openaccess@tue.nl

providing details and we will investigate your claim.

Study of III–V semiconductor nanostructures by cross-sectional scanning tunneling microscopy

PROEFSCHRIFT

ter verkrijging van de graad van doctor aan de
Technische Universiteit Eindhoven, op gezag van de
Rector Magnificus, prof.dr.ir. C.J. van Duijn, voor een
commissie aangewezen door het College voor
Promoties in het openbaar te verdedigen op
donderdag 15 september 2005 om 16.00 uur

door

Peter Offermans

geboren te Heerlen

Dit proefschrift is goedgekeurd door de promotoren:

prof.Dr. J.H. Wolter
en
prof.Dr. K.H. Ploog

Copromotor:
dr. P.M. Koenraad

CIP-DATA LIBRARY TECHNISCHE UNIVERSITEIT EINDHOVEN

Offermans, Peter

Study of III–V semiconductor nanostructures by cross-sectional scanning
tunneling microscopy / door Peter Offermans. –
Eindhoven : Technische Universiteit Eindhoven, 2005. –
Proefschrift
ISBN 90-386-2281-3
NUR 926

Trefw.: rastertunnelingmicroscopie / 3–5 verbindingen / nanostructuren / elec-
tronenmicroscopisch oppervlakte-onderzoek

Subject headings: scanning tunneling microscopy / III–V semiconductors / atomic
structure / semiconductor quantum dots / semiconductor quantum wells / surface
topography / surface composition / elastic deformation / surface segregation

The work presented in this thesis was carried out at the COBRA Inter-University
Research Institute on Communication Technology at the Eindhoven University
of Technology.

Contents

1	Introduction	7
1.1	Cross-sectional scanning tunneling microscopy	7
1.2	Semiconductor engineering	8
1.2.1	Quantum wells	8
1.2.2	Quantum dots	10
1.2.3	Quantum rings	11
1.3	Scope of thesis	12
2	Cross-sectional scanning tunneling microscopy for nanostructure analysis	15
2.1	Fundamentals of STM	15
2.2	Voltage dependent imaging of surface states	18
2.3	Topographic contrast electronically induced by bulk states	18
2.4	Tip-induced band bending	20
2.5	Suppression of electronic contrast for STM topography	21
2.6	Conclusion	24
3	X-STM topography	25
3.1	Relaxation of a cleaved quantum well	26
3.2	The effect of cubic symmetry on the relaxation of a cleaved quantum well	27
3.3	Relaxation of a cleaved quantum dot	29
3.4	Calculation of the strain field of a cleaved quantum dot	32
3.5	Conclusion	34
4	Growth techniques, experimental setup and preparation procedures	37
4.1	Growth techniques and control	37
4.2	Sample preparation, mounting and cleavage	38
4.3	Tip preparation	40
4.4	The STM unit	41
4.5	The UHV system	43
4.6	Summary	45

5	Indium incorporation in III/V semiconductor structures: an overview	47
5.1	Structural quality of MOVPE grown InP based Quantum Cascade Lasers	47
5.2	InGaAs/AlAsSb Quantum Cascade Lasers	49
5.3	(In,Ga)As sidewall quantum wires on shallow-patterned InP (311)A	49
5.4	Ordered quantum dot molecules formed by self-organized anisotropic strain engineering	52
5.5	Formation of columnar (In,Ga)As quantum dots on GaAs(100) . .	53
5.6	Conclusion	53
6	Annealing of (In,Ga,Al)As digital alloy	55
6.1	Introduction	55
6.2	Sample description	56
6.3	Results	56
6.4	Conclusion	60
7	Digital alloy interface grading of an InGaAs/InAlAs quantum cascade laser structure	61
7.1	Introduction	61
7.2	Sample description	62
7.3	Results	63
7.4	Conclusion	67
8	Formation of InAs wetting layers	69
8.1	Introduction	69
8.2	Sample description	70
8.3	Results	71
8.4	Conclusion	75
9	Atomic-scale structure and photoluminescence of InAs quantum dots in GaAs and AlAs	77
9.1	Introduction	78
9.2	Sample description and experimental setup	78
9.3	Results and Discussion	79
	9.3.1 Structure	79
	9.3.2 Photoluminescence	84
9.4	Conclusion	88
10	Capping process of InAs/GaAs quantum dots	91
10.1	Introduction	91
10.2	Sample description	92
10.3	Results	93

10.4 Conclusion	97
11 Atomic-scale structure of self-assembled (In,Ga)As quantum rings in GaAs	99
11.1 Introduction	99
11.2 Sample description and experimental setup	100
11.3 Results	101
11.4 Conclusion	106
Bibliography	109
List of main results	117
Summary	119
Nederlandse samenvatting	121
Acknowledgements	123
List of publications	125
Curriculum Vitae	129

CONTENTS

1

Introduction

In this thesis, cross-sectional scanning tunneling microscopy (X-STM) has been used to analyse the atomic-scale structural properties of a wide range of III/V compound semiconductor nanostructures, such as quantum wells, wires, dots and rings.

III/V compound semiconductor nanostructures are epitaxially grown structures of compounds formed from the group III and group V elements of the periodic table. These semiconductor nanostructures have nanometer-scale dimensions, which results in the quantization of their electronic states and therefore exhibit interesting optical and electronic properties that are employed in devices such as semiconductor lasers and detectors, light-emitting diodes, highly-efficient solar cells and RF power amplifiers. Areas of application include the wireless and optical telecommunication market, chemical and biological sensing, and illumination.

Knowledge of the shape, size and composition of semiconductor nanostructures is essential in order to unravel the growth processes involved in the formation of these structures and to better understand their opto-electronic properties. One of the few tools that offer a direct visualization and analysis of semiconductor structures at the atomic scale is cross-sectional scanning tunneling microscopy.

1.1 Cross-sectional scanning tunneling microscopy

The scanning tunneling microscope is part of the family of the scanning probe microscopes, which have in common that they are able to provide a direct real space information of a physical property at the atomic scale. This is done by

scanning a probe across the surface of a sample while recording the measured signal, which results in an image of the surface. In the case of scanning tunneling microscopy (STM), invented in 1981 by Binnig and Rohrer, the probe consists of a metallic tip which is brought into tunneling contact with a (semi-)conducting surface.

The quantum mechanical tunneling effect allows the electron to tunnel through the vacuum barrier even when the energy of the electrons is lower than the potential barrier. Since the tunneling current depends exponentially on the distance between tip and sample, an atomic-scale height map of the surface topography can be acquired by adjusting the tip-sample distance during scanning, using a feedback loop that keeps the tunneling current constant.

In cross-sectional scanning tunneling microscopy (X-STM), the direct visualization of nanoscopic structures that are generally embedded in several layers of semiconducting material, is possible by cleaving the sample and thereby exposing the cross-sectional surface of the buried nanostructures.

Another technique that allows the acquisition of images at the atomic scale is (high resolution) cross-sectional transmission electron microscopy (X-TEM). X-TEM is a probeless technique which is extremely sensitive to the crystallographic structure of the bulk of the semiconducting material. However, since it typically averages over about 50 atomic layers, depending on sample thickness, it is not a true surface technique.

1.2 Semiconductor engineering

1.2.1 Quantum wells

A wide range of III/V compound semiconductor materials and their alloys has been investigated in the past for their bulk properties. Two of the important properties of these materials are the band gap and the lattice constant, as shown in Fig. 1.1. The most commonly used III/V semiconductors have a direct band gap, which means that they can emit light by electron-hole recombination across the semiconductor band gap. The band gap determines the wavelength at which the semiconductor emits. This is important, since particular wavelengths are used for different applications. In telecommunications, for example, the wavelengths of $1.3\ \mu\text{m}$ and $1.55\ \mu\text{m}$ are highly desired, since at these wavelengths the losses in optical glass fibers are minimal. The lattice constant determines whether layers of different materials can be grown epitaxially, which is needed in order to produce defect-free structures.

The $\text{Al}_x\text{Ga}_{1-x}\text{As}/\text{GaAs}$ system is an obvious material system for the growth of heterostructures since its compounds have almost the same lattice constant, but a different band gap. This property may be used for the growth of layered structures such as quantum wells, where electrons and holes are confined to the

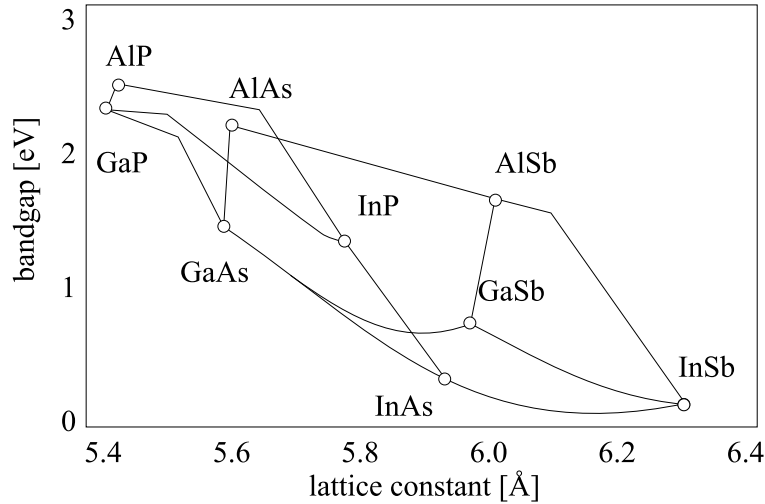


Figure 1.1: The world of the III/V semiconductors. The diagram shows the band gap of the semiconductor as function of the lattice constant. The solid lines connecting two binary alloys indicate the functional dependence of the band gap and lattice constant on the composition of a ternary alloy formed from its binary constituents.

layer with the smallest band gap. For $x < 0.4$, $\text{Al}_x\text{Ga}_{1-x}\text{As}$ has a direct band gap and may be used as the barrier material, while GaAs may be used as the well material. The wavelength of the light emitted by the quantum well can be tuned by changing the width of the well or the composition of the barrier.

$\text{In}_{0.53}\text{Ga}_{0.47}\text{As}/\text{In}_{0.52}\text{Al}_{0.48}\text{As}$ (or shorter: InGaAs/InAlAs) is a well known system that can be used for lattice matched growth on InP substrates. The advantage of this system over AlAs/GaAs is that it traps electrons and holes more effectively. The wavelength of quantum wells grown using this material system can only be changed by tuning the width of the well, since the composition cannot be changed without affecting the lattice constant. This problem can be solved by the growth of a digital alloy, i.e., a material that consists of a sequence of thin layers of $\text{In}_{0.53}\text{Ga}_{0.47}\text{As}$ and $\text{In}_{0.52}\text{Al}_{0.48}\text{As}$, where the number and thickness of each layer determines the average composition.

The use of a digital alloy as the barrier and well material of a $\lambda = 1.3 \mu\text{m}$ multiple quantum well structure is presented in Chapter 6. The mid-infrared ($\lambda = 9.3 \mu\text{m}$) quantum cascade laser structure presented in Chapter 7 serves as an excellent example of a state-of-the-art structure where control of the thickness of a large number of layers is essential in order to achieve the desired inter-subband energy spacings and wave function overlap. For both kind of structures, it is therefore important to have a proper knowledge of the atomic-scale properties like the thickness of the layers and the interface quality.

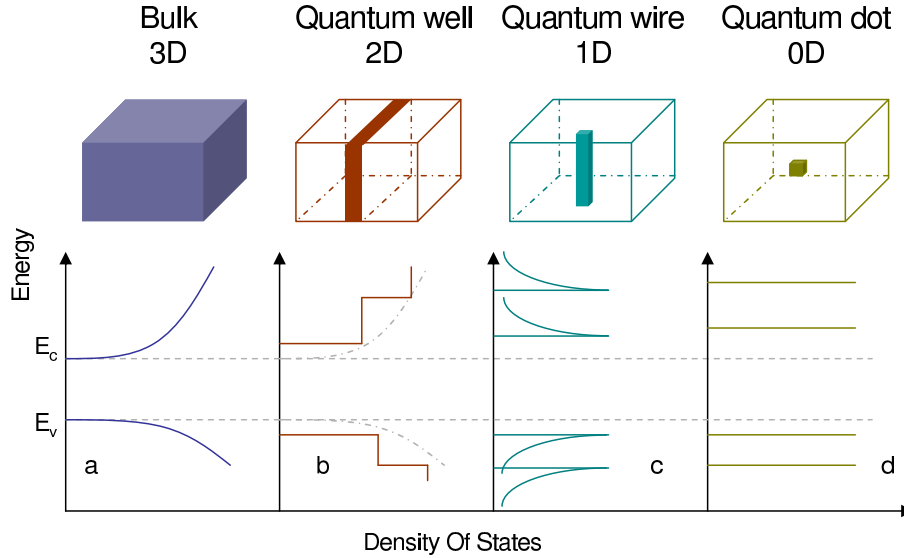


Figure 1.2: Density of states for semiconductor structures with different degrees of confinement.

A much wider range of materials becomes available, if the requirement of lattice matched growth is relaxed and strained thin layers are permitted, see for example the InGaAs/AlAsSb quantum cascade laser in Section 5.2. Strain may even be employed to enhance the optical properties of layered structures, since it affects the band structure, and it can be used to achieve the growth of three-dimensional islands — so-called quantum dots — which exhibit interesting properties of their own.

1.2.2 Quantum dots

Self-assembled MBE-grown semiconductor quantum dots are formed by Stranski-Krastanov growth [1]. In this growth mode, a layer with lattice constant a_1 is grown on a substrate with lattice constant a_2 , where $a_1 > a_2$. Strain builds up with increasing thickness of the pseudomorphic, i.e., lattice-mismatched, layer until it becomes energetically more favorable for the growth of three-dimensional islands to occur. These three-dimensional islands are called quantum dots, since they confine electrons and holes in three dimensions, resulting in a zero-dimensional density of states, i.e., discrete energy levels, see Fig. 1.2. Quantum dots have also been called artificial atoms, since their discrete electronic structure resembles the electron shell structure of atoms.

Quantum dots find an important application in semiconductor laser devices. Because of the delta-function-like density of states and the strong electron-hole confinement in quantum dots, they offer a lower threshold current density J_{th} , less

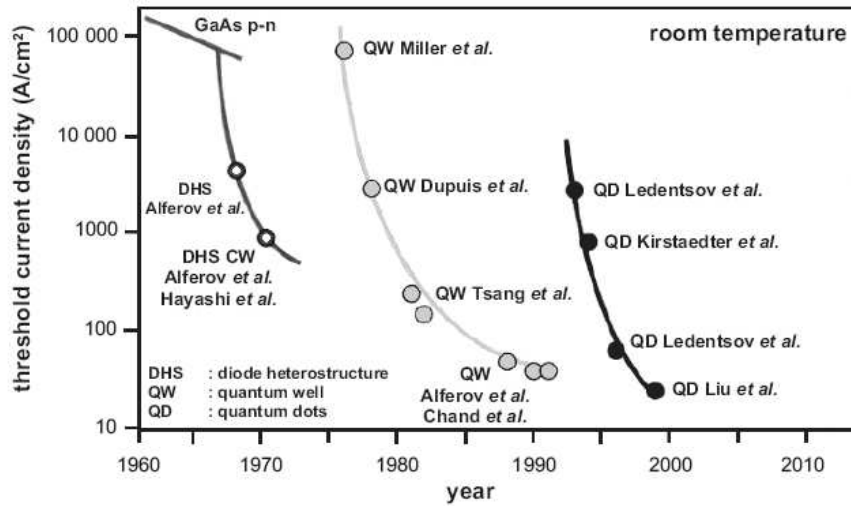


Figure 1.3: Decrease of the threshold current density of semiconductor injection lasers with different dimensionality active regions [2].

temperature sensitivity of J_{th} , and a higher gain compared to quantum wells [2]. Figure 1.3 compares the improvements in the threshold current density of bulk, quantum well and quantum dot lasers. More recently, the emphasis has switched to the possibility of obtaining GaAs-based quantum dot lasers operating in the short-haul $1.3 \mu\text{m}$ telecommunication band. Although GaAs-based quantum dot lasers are now available for $1.3 \mu\text{m}$ applications with superior characteristics to conventional InP based quantum well lasers, it is still desirable to improve the temperature stability of J_{th} further, and to extend operation to the long-haul telecommunication band at $1.55 \mu\text{m}$ [3].

Other areas of application of quantum dots include: normal incidence mid-infrared intersub-level detection [4] and semiconductor optical amplifiers [5]. Furthermore, quantum dots are promising as memory devices [6], single-photon sources for quantum cryptography [7], and as two-level systems for quantum information processing [8]. Finally, in the form of colloidal solutions [9], quantum dots are ideal as tracers [10] for biological applications, because of their optical properties and small size.

1.2.3 Quantum rings

Self-assembled semiconductor quantum rings (QRs) can be realized by the capping of self-assembled QDs grown by Stranski-Krastanov-mode with a layer thinner than the dot height and subsequent annealing [11].

Quantum rings are a special class of nanostructures that have attracted a lot of attention due to the occurrence of the Aharonov-Bohm effect, which is specific to the doubly-connected topology of a ring [12, 13, 14, 15, 16, 17].

The electronic states in QRs can be discussed using the ideal model of a circular, one-dimensional wire, bent into a circle of radius R . The energy levels then follow from the periodic boundary conditions as $E_l = \frac{\hbar^2}{2m^*} k_l^2$ with $k_l = l\frac{1}{R}$ where $l = 0, \pm 1, \pm 2, \dots$, and m^* is the effective mass of the electron. When a magnetic flux $\Phi = \pi R^2 B$ penetrates the interior of the ring, an additional phase is picked up by the electron on its way around the QR (the Aharonov-Bohm effect) which leads to a change in the ground state energy to

$$E_l = \frac{\hbar^2}{2m^* R^2} \left(l + \frac{\Phi}{\Phi_0} \right)^2, \quad l = 0, \pm 1, \pm 2, \dots,$$

with $\Phi_0 = \frac{h}{e}$ being the flux quantum [18]. Therefore, with increasing magnetic field, the electron is able to lower its ground state energy by decreasing its quantum number of the angular momentum l , resulting in a periodic oscillation in the ground state energy. Such oscillations have recently been observed by optical detection of the emission of a charged exciton in a nanoscale lithographically etched QR [15] and by a combination of capacitance-voltage and far-infrared spectroscopy of self-assembled semiconductor QRs [18].

1.3 Scope of thesis

In this thesis, atomic scale structural characterization by X-STM is combined with isotropic elasticity theory for the determination of the composition of cleaved nanostructures. The determination of the size, shape *and* composition of buried nanostructures at the atomic scale, is used in order to unravel the growth processes involved in the formation of various III/V nanostructures, and to better understand their opto-electronic properties. An extensive list of the main results of this thesis can be found on page 117.

This thesis is organized as follows. In Chapter 2 the underlying principles of scanning tunneling microscopy (STM) as a tool for the determination of size, shape and composition of nanostructures are explained. It is shown that STM can operate in two modes which either enable the acquisition of images reflecting electronic contrast or topographic contrast.

In Chapter 3 it is shown how the measurement of the outward displacement and strain (measured by the change in lattice spacing) of the cleaved surface, can be used to determine the indium composition of (In,Ga)As nanostructures, by comparing the experimental data with the calculated relaxation and strain using elasticity theory. It is shown that the use of isotropic elasticity theory leads to a more realistic agreement with experimental data compared to the use of cubic elasticity.

Chapter 4 starts with the description of the techniques that allow the epitaxial growth of different semiconductor compounds for the formation of the nanostructures. It is shown how pieces of the wafer containing the semiconductor nanostructures are prepared for the X-STM measurement and how an atomically flat cross-sectional surface is achieved. The atomic-scale measurement of the nanostructures is only possible by the use of an ultra-high-vacuum environment that keeps the cleaved surface free of contamination, and the reliable positioning and fabrication of STM tips.

The aim of Chapter 5 is to provide the reader with a short overview of different functional structures where indium incorporation plays a key role in the growth, and hence the performance of the device. Indium incorporation determines the sharpness of interfaces and the size, shape and composition of self-assembled nanostructures.

Chapters 6 to 11 each provide a detailed structural analysis of various III/V nanostructures and form the main body of the work. In chapter 6 we investigate the structural properties of as-grown and annealed (750°C and 800°C) digital alloy (In,Ga,Al)As ($\lambda = 1.3 \mu\text{m}$) multiple quantum well laser structures, exploiting the electronic contrast seen with X-STM between layers of different materials.

Chapter 7 shows the use of digital alloy grading to soften the barriers of the active region of a mid-infrared ($\lambda = 9.3 \mu\text{m}$) quantum cascade laser structure. We show that due to alloy fluctuations, softening of the barriers occurs even without the digital grading.

In Chapter 8 we change the focus from two-dimensional to self-assembled three-dimensional structures, with an analysis of the composition of wetting layers. We show that the determination of the composition of the wetting layers by indium counting and by analysis of the outward relaxation of the cleaved surface are in excellent agreement.

Chapter 9 then continues with the determination of the composition of InAs/GaAs and InAs/AlAs quantum dots, using the outward relaxation and the change in lattice constant of the cleaved dot surface. By calculation of the photoluminescence (PL) ground state energies based on the structural analysis, and comparing these to measured PL spectra, we show that X-STM yields very sensible results for the composition of quantum dots. Based on our calculations, we discuss the PL processes in InAs/AlAs dots.

Chapter 10 deals with the formation and the capping process of quantum dots. The effect of partial capping and subsequent annealing has a dramatic effect on the dot size and shape.

Under very specific growth conditions the capping and annealing can be controlled to transform the dots into rings. We show in Chapter 11 that these quantum rings have an asymmetric, indium-rich, crater-like shape with a depression rather than an opening at the center. Although the shape of a buried quantum ring differs strongly from an idealized circular-symmetric open ring structure, we

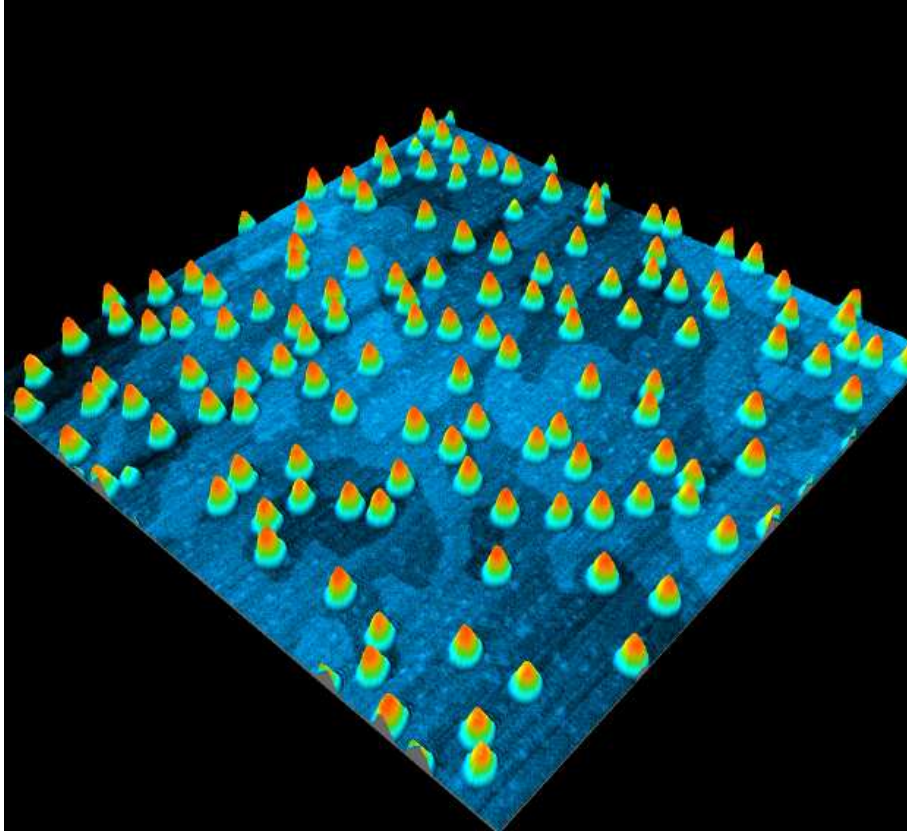


Figure 1.4: $1 \times 1 \mu\text{m}^2$ atomic force microscopy (AFM) image of InAs quantum dots grown on a GaAs surface by Stranski-Krastanov growth mode. Atomic steps on the GaAs surface can be seen in the image. The sample was grown by Klaus Pierz, Physikalisch-Technische Bundesanstalt Braunschweig, Germany.

conclude that there is a chance to observe Aharonov-Bohm-type oscillations in the magnetization.

2

Cross-sectional scanning tunneling microscopy for nanostructure analysis

In this chapter the underlying principles of scanning tunneling microscopy (STM) as a tool for the determination of size, shape and composition of nanostructures are explained. Then, the contribution of electronic and topographic contrast to STM images is discussed. Finally, it is shown how the topography of the cleaved surface can be used to determine the composition of buried nanostructures.

2.1 Fundamentals of STM

In the tunneling process, electrons tunnel through the vacuum between tip and surface, which acts as a potential barrier. The quantum mechanical tunneling effect allows the electron to tunnel through the potential barrier even when the energy of the electrons is lower than the potential barrier. The tunneling current depends on the overlap between the tip state and the sample state through the barrier, and is given to first order in Bardeen's [19] formalism by:

$$I = \frac{2\pi e}{\hbar} \sum_{\mu,\nu} [f_t(E_\mu) - f_s(E_\nu + eV)] |M_{\mu,\nu}|^2 \delta(E_\mu - E_\nu) \quad (2.1)$$

where f_s and f_t are the Fermi distribution functions in the sample and tip, V the applied voltage between tip and sample ($V = V_{\text{sample}} - V_{\text{tip}}$), $M_{\mu,\nu}$ the quantum mechanical tunneling matrix element between the tip state μ and the sample state ν , E_μ and E_ν are the energies of the states μ and ν , and $\delta(E_\mu - E_\nu)$ the

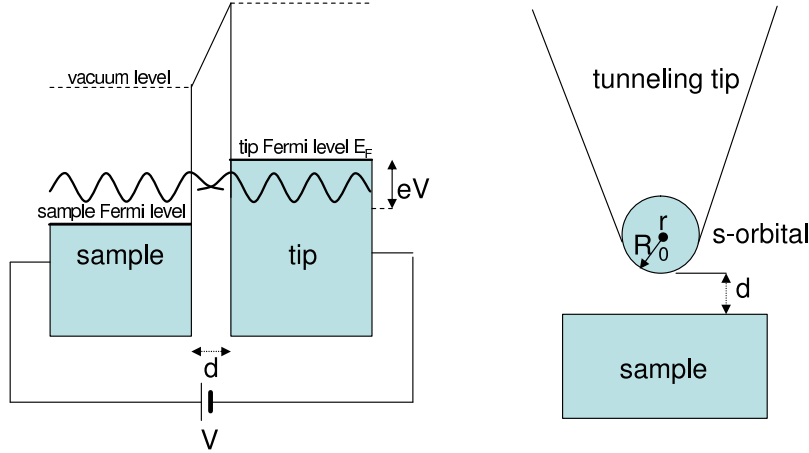


Figure 2.1: (a) Schematic showing the overlap and decay of tip and sample wave functions in the vacuum barrier, (b) Schematic representation of the tunneling geometry in the Tersoff-Hamann model.

Dirac δ function indicating that only tip and sample states with the same energy can tunnel to each other. The tunneling matrix elements are obtained from:

$$M_{\mu\nu} = \frac{\hbar^2}{2m_e} \int d\bar{S} \cdot (\psi_\mu^* \Delta \psi_\nu - \psi_\nu \Delta \psi_\mu^*) \quad (2.2)$$

where the integral is over any surface lying entirely within the vacuum barrier, m_e is the electron mass and ψ_μ (ψ_ν) is the wavefunction of the electron in state μ (ν). By approximating the Fermi distribution by a step function and assuming that the tunneling matrix elements do not change considerably for states between E_F and $E_F + eV$, i.e., low temperature and low voltage, the tunneling current becomes:

$$I = \frac{2\pi e^2}{\hbar} V \sum_{\mu,\nu} |M_{\mu,\nu}|^2 \delta(E_\nu - E_F) \delta(E_\mu - E_F). \quad (2.3)$$

To evaluate $M_{\mu\nu}$, the surface wave functions may be expanded in plane waves parallel to the surface with decaying amplitude into the vacuum:

$$\psi_\nu \sim \sum_G a_G e^{\sqrt{\kappa + |\bar{\kappa}_G|^2} z} e^{i\bar{\kappa}_G \cdot \bar{x}} \quad (2.4)$$

where $\kappa = \hbar^{-1}(2m\Phi)^{1/2}$ is the inverse decay length for the wave functions in vacuum with Φ the work function, and $\bar{\kappa}_G = \bar{\kappa}_\parallel + \bar{G}$, where $\bar{\kappa}_\parallel$ is the surface Bloch wave vector of the state and \bar{G} is a surface reciprocal-lattice vector.

It was shown by Tersoff and Hamann [20] that if the tip wave function is an s -state and modeled using an asymptotic spherical form with $\rho = |\bar{r} - \bar{r}_0|$ and \bar{r}_0 the center of curvature of the tip:

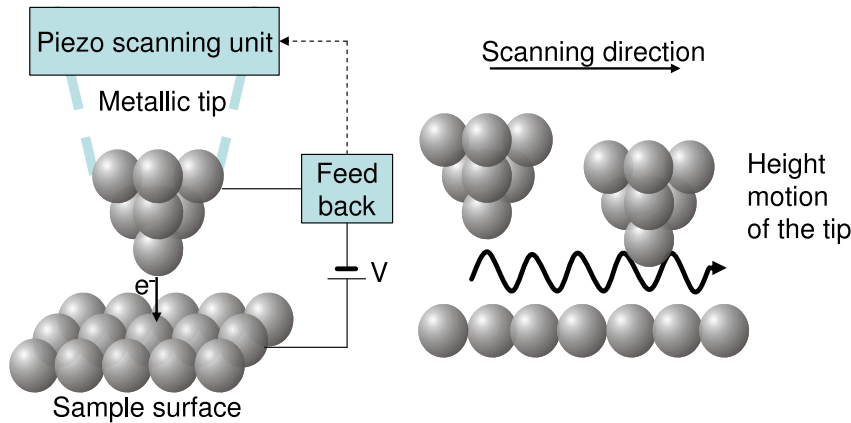


Figure 2.2: Schematic of a scanning tunneling microscopy with feedback loop.

$$\psi_\mu \sim (\kappa\rho)^{-1} e^{-\kappa\rho} \quad (2.5)$$

the tunneling matrix element is proportional to the amplitude of ψ_ν at the center of the tip orbital, and the conductance becomes:

$$dI/dV \sim \sum_\nu |\psi_\nu(\bar{r}_0)|^2 \delta(E_\nu - E_F) \equiv \rho_{\text{sample}}(\bar{r}_0, E_F). \quad (2.6)$$

The quantity on the right reflects the surface local density of states (LDOS) at E_F , i.e., the charge density from states at the Fermi level. Thus the tunneling current is proportional to the surface LDOS at the position of the point probe, and the STM image represents a contour map of constant surface LDOS. If the tip-state is p -like or d -like, the tunneling matrix element is no longer proportional to $\psi_\nu(\bar{r}_0)$ but proportional to a spatial derivative of $\psi_\nu(\bar{r}_0)$, which generally leads to an enhanced corrugation seen on the STM image. Note, in the case of Tungsten tips, the most probable state is a d state.

Since $|\psi_\nu(\bar{r}_0)|^2 \sim e^{-2\kappa(R+d)}$ with R the radius of the tip and d the tip-sample distance, the tunneling current decays in a first approximation exponentially into the vacuum:

$$I \sim \exp(-2\kappa d). \quad (2.7)$$

A height map of the surface can then be acquired by adjusting the tip-sample distance during scanning using a feedback loop that keeps the tunneling current constant. The electronic contribution of the surface LDOS to the apparent height then results in an atomic scale corrugation visible in the STM image.

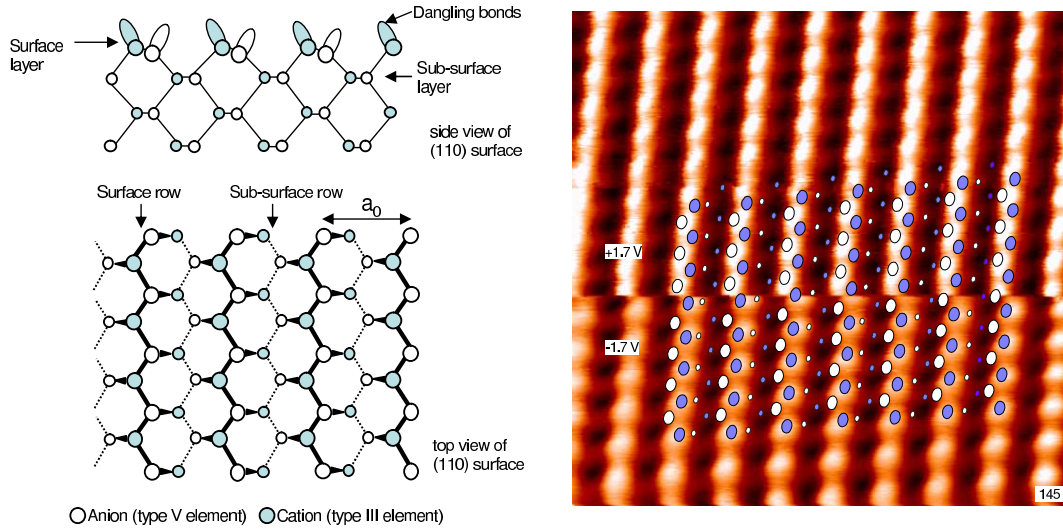


Figure 2.3: (a) Schematic top and side view of III/V semiconductor (110) surface, (b) STM image showing the atomic corrugation at both polarities.

2.2 Voltage dependent imaging of surface states

In cross-sectional scanning tunneling microscopy, semiconductor wafers are cleaved along a natural cleavage plane to expose a cross-section of the epitaxial layers grown on the wafer. In the case of III/V semiconductors, the (110) and $(1\bar{1}0)$ cleavage planes of the zinc-blende crystal, show a 1×1 surface unit cell reconstruction where the group III elements move into the surface while the group V elements move outward. This buckling behavior causes the energetic position of the dangling bond surface states of the type III and the type V elements to move above and below the semiconductor band gap in the bulk, respectively. Therefore, depending on the polarity of the applied bias between tip and sample, either the empty states of the type III elements are imaged ($V_{\text{sample}} > 0$) or the filled states of the type V elements ($V_{\text{sample}} < 0$). Since the (110) and $(1\bar{1}0)$ surface planes contain only half of the (001) layers within the zinc-blende crystal, the atomic rows observed in the cross-sectional STM image are separated by a bi-layer distance in the growth [001] direction, which is equal to the lattice constant a_0 .

2.3 Topographic contrast electronically induced by bulk states

Because there are no surface states present in the band gap of most cleaved III/V semiconductors, the Fermi level at the cleaved surface is unpinned, i.e., it is not

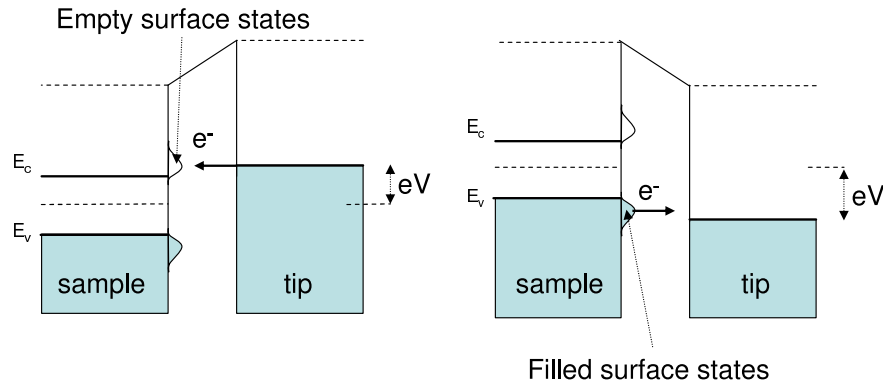


Figure 2.4: Schematic of tunneling into empty and filled surface states.

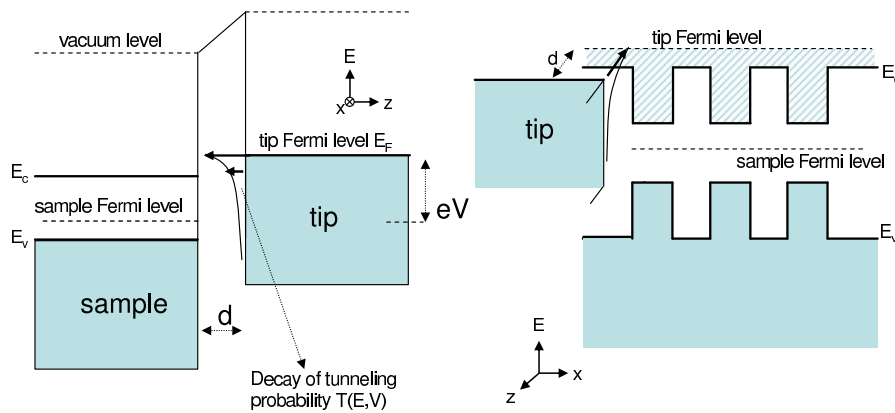


Figure 2.5: (a) At high voltages not only the states near the Fermi energy contribute to the current, but all states between E_F and $E_F + eV$. (b) Current flow in a heterostructure. More states are available for tunneling in the material with the lowest conduction band edge, inducing an electronic contrast in the STM image.

forced to assume a specific value in the band gap independent of its value in the bulk material. This allows the electronic properties of the bulk to be probed at energies near the band gap. The bulk states generally contribute an apparent contrast to STM images that is not related to the actual physical topography of the surface, but governed by factors such as variations in the band gap, doping level and electron affinity.

At non-zero bias voltages, not only states at the Fermi level E_F participate in the tunneling process, but all occupied tip states or sample bulk states between

E_F and $E_F + eV$. Since the spectrum of bulk states in the sample and tip are continuous rather than discrete, the sum in Equation 2.1 may be converted to an integral over all the different electron energies that are allowed to participate in the tunneling process:

$$I(V) \sim \int_{E_{F,\text{tip}}}^{E_{F,\text{tip}}+eV} \rho_t(E) \rho_s(E + eV) [f_t(E) - f_s(E + eV)] T(E, V) dE \quad (2.8)$$

where ρ_t and ρ_s are the bulk densities of states in the tip and sample, and $T(E, V)$ the transmission coefficient which plays a similar role as the tunneling matrix element $M_{\mu\nu}$. The transmission coefficient $T(E, V)$ is expressed in the WKB approximation [21] as [22]:

$$T(E, V) = \exp \left\{ -2\sqrt{2m_e/\hbar^2} \int \sqrt{\Phi(V, z) - E} dz \right\} \quad (2.9)$$

with $\Phi(V, z) - E$ the effective tunneling barrier for states with energy E . The transmission coefficient describes the exponential decay of the tunneling probability as a function of the effective barrier height, due to the decreasing penetration depth of states with lower energy into the vacuum.

In the case of empty states tunneling to a heterostructure where the conduction band edge of one of the layers is lower, more states are available for tunneling in the material with the lower conduction band edge. For injection close to the conduction band edge, this results in a strong difference in tunneling current while scanning across such a heterostructure. Maintaining a constant tunneling current during scanning requires the tip-sample distance to be adjusted, which leads to an apparent height difference. Such cross-sectional STM images can be used to assess alloy fluctuations and interface roughness at the atomic scale, see for example Chapter 6 and Chapter 7.

2.4 Tip-induced band bending

Another effect that contributes to the electronic contrast in the image is tip-induced band bending, which is intrinsically related to the doping level of the semiconductor. When a tip and a semiconductor are brought into tunneling contact in the absence of an applied voltage, a non-equilibrium situation is created, since the Fermi levels of tip and semiconductor are generally not aligned relative to the vacuum level. When the Fermi level of the sample is higher than that of the tip, electrons at the surface of the sample will tunnel to the tip, thereby creating an electric field between semiconductor and tip. The electric field is shielded in the semiconductor by space charge which may be due to ionized donors or acceptors and results in the bending of the conduction and valence bands near the surface, aligning the Fermi level in the semiconductor with that of the tip.

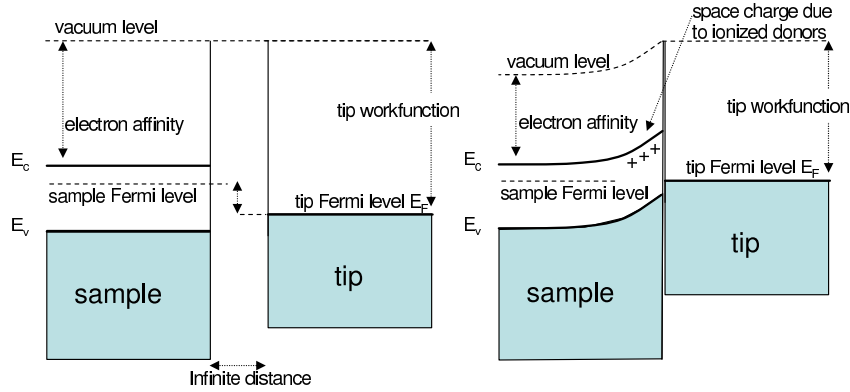


Figure 2.6: (a) Schematic view of tip and n-type semiconductor at infinite distance. (b) Schematic view of a Schottky contact.

In case of physical contact between a metal and a semiconductor, this is called a Schottky contact. The width of the space charge region into the semiconductor depends on the extent of the band bending and the doping level.

Applying a voltage between the tip and the sample increases or decreases the existing electric field which affects the bending of the conduction and valence bands near the surface. When scanning at relatively low voltages, the electrons at the Fermi level of the tip must not only tunnel through the vacuum barrier, but also through the depletion region inside the semiconductor, due to the bending of the conduction and valence bands. Since the width of this region depends on the doping level, the voltage required to tunnel with the same current to the conduction band of a n-type semiconductor differs from that for an undoped or p-type semiconductor. This results in an apparent height contrast in a constant-current STM image, which enables the visualization of structures like pn-junctions.

2.5 Suppression of electronic contrast for STM topography

The electronic contribution to the apparent height in the STM image due to band offsets and tip-induced band bending can be suppressed to a large extent by scanning at high voltages [23, 24]. Since the tunneling probability decays exponentially with the height of the effective tunneling barrier $\Phi(V, z) - E$, the states with the highest energy contribute most to the tunneling current. If a sufficiently large voltage is applied during empty state imaging of a heterostructure, the states contributing most to the tunneling current have energies far above the conduction band edge and the contribution of the lower lying states is negligible.

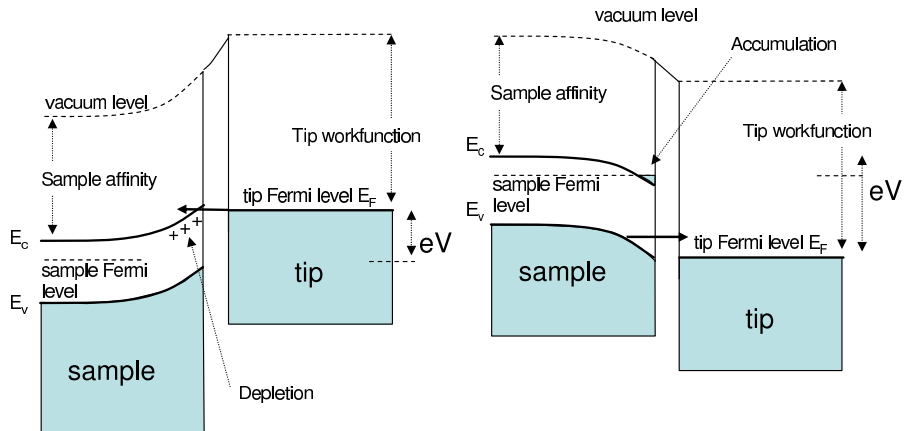


Figure 2.7: Schematic view of tunneling into the conduction band of a n-type semiconductor at both polarities and relatively low voltage.

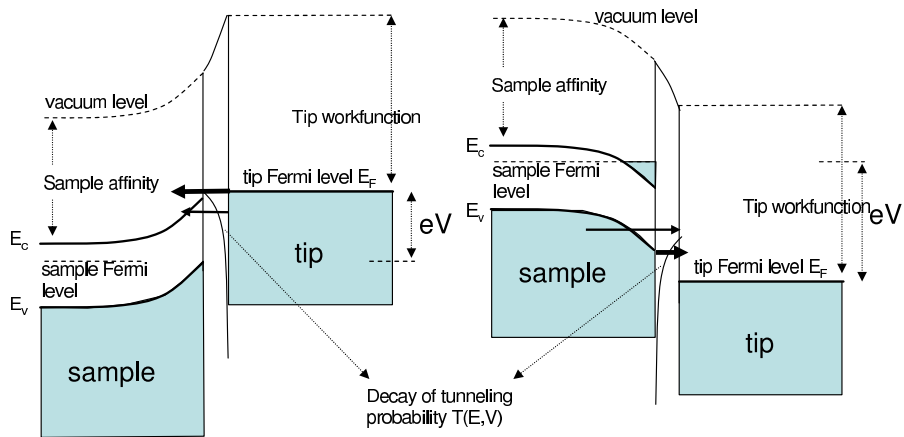


Figure 2.8: Schematic view of tunneling into the conduction band of a n-type doped semiconductor at both polarities and high voltage.

Similarly, the voltage dependent sensitivity of the tunneling current on doping level can be overcome by injecting electrons above the depletion region.

In the case of filled states tunneling (electron tunneling from sample to tip), the valence band offset in a heterostructure is smaller with respect to the total barrier height than the conduction band offset, since the effective barrier height for tunneling is increased by the band gap. Therefore, the resulting electronic contrast is smaller than in the case of empty states tunneling (electron tunneling from tip to sample).

In order to verify the previously presented mechanisms causing electronic contrast in STM images, the difference in tip-sample distance, i.e., the appar-

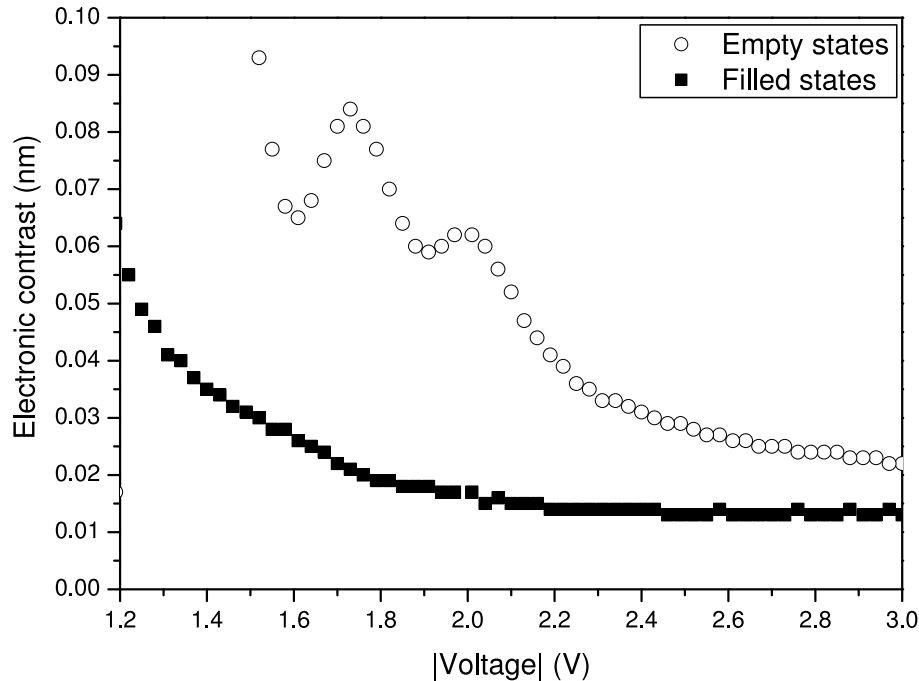


Figure 2.9: Calculated voltage dependence of the apparent height due to electronic contrast between an $\text{In}_{0.14}\text{Ga}_{0.86}\text{As}$ quantum well and a surrounding GaAs matrix. The calculation has been performed for a fixed tunneling current I_{tun} of 100 pA, a donor concentration N_{donor} of $2 \times 10^{15} \text{ cm}^{-3}$ and an acceptor concentration N_{acceptor} of $2 \times 10^{17} \text{ cm}^{-3}$. The oscillation in the calculated electronic contrast for injection into empty conduction band states is due to the difference, between $\text{In}_{0.14}\text{Ga}_{0.86}\text{As}$ and GaAs, in the onset voltage for injection into the L and X valleys. At these onset voltages an extra contribution in the tunneling current is possible which results in an increase in the tip-sample distance.

ent height, from tunneling to an $\text{In}_{0.14}\text{Ga}_{0.86}\text{As}$ layer embedded in a GaAs matrix at a fixed current, has been calculated as a function of voltage using the one-dimensional model described by Feenstra [22]. For a given bias voltage and tip-sample distance, the tip-induced band bending and the shape of the vacuum barrier is determined by solving the Poisson equation, with the boundary condition that the electric field at the semiconductor surface is continuous. The effect of image charge is taken into account. The apparent height $\Delta(V)$ has been calculated using

$$\Delta(V) = Z_1(V) - Z_2(V) \quad (2.10)$$

where $Z_1(V)$ and $Z_2(V)$ are the tip-sample distances as a function of voltage at a fixed tunneling current for $\text{In}_{0.14}\text{Ga}_{0.86}\text{As}$ and GaAs, respectively. Note, the

change in the band offset between $\text{In}_{0.14}\text{Ga}_{0.86}\text{As}$ and GaAs due to pseudomorphic strain, when the $\text{In}_{0.14}\text{Ga}_{0.86}\text{As}$ layer is incorporated in the GaAs matrix, has been taken into account using the model-solid theory of Van de Walle [25].

As shown in the figure, the electronic contrast indeed decreases with increasing tunneling voltage. For the empty state imaging mode the electronic contrast is larger than for the filled state imaging mode, as predicted, showing that for the suppression of electronic contrast the filled state imaging mode is best suited.

Note, that even at high tunneling voltages a small electronic height difference (≈ 10 pm) remains between the filled and empty state imaging mode. This is due to the differences in the bulk density of states ρ_s of the different materials. In the model, the bulk density of states is taken into account by the effective electron mass, which differs for $\text{In}_{0.14}\text{Ga}_{0.86}\text{As}$ and GaAs and thus results in a different tunneling current (and measured apparent height) to the two materials.

Thus, at high (preferably negative) sample voltages, the electronic contribution to the height contrast is minimized, enabling the acquisition of the true (filled states) topography of the structure, such as the outward relaxation of the cleaved surface.

2.6 Conclusion

In this chapter the underlying principles of scanning tunneling microscopy (STM) were explained. It can be concluded that STM is a valuable tool for the determination of size, shape and composition of nanostructures. At a low tip-sample voltage ($|V| < 2$ V) electronic effects dominate the contrast in the image. The electronic contrast enables the visualization of interfaces between layers with different conduction or valence band offsets, as is shown in Chapters 6 and 7. At a high tip-sample voltage ($|V| > 2$ V), electronic contributions to the contrast are minimized which enables the acquisition of the true surface topography. This can be used for the determination of the composition and strain in cleaved nanostructures, as is shown in Chapter 3.

3

X-STM topography

When two materials with a different lattice constant are used in a heterostructure, it is strained. SK-grown (In,Ga)As quantum dots are the ultimate example of such strained heterostructures, but also (In,Ga)As quantum wells have built-in strain. When such a structure is cleaved, it reduces its built-in tensile or compressive strain by deforming the cleaved surface. Regions under compressive strain bulge outward while tensile strain depresses the cleaved surface. The strain can be measured in two ways with cross-sectional scanning tunneling microscopy:

- Strain in the plane of the surface can be deduced from the lattice spacing
- Distortion normal to the surface can be measured (without the need for atomic resolution in the plane) using (filled states) topography

The measured outward displacement and strain (measured by the change in lattice spacing), can be used to determine the indium composition of a strained (In,Ga)As nanostructure, by comparing the experimental data with the calculated relaxation and strain using elasticity theory. In the case of quantum wells with a low concentration of indium ($< 30\%$), or wetting layers (see Chapter 8), the indium distribution can also be obtained directly by counting the indium atoms. However, in the case of InAs quantum dots the indium concentration is too high to distinguish individual indium atoms, and the only way to determine its composition is by fitting to the measured outward relaxation or change in lattice constant. This has been done in Chapters 9 and 11. The strain field of a low-temperature-capped quantum dot shown in Chapter 10 is illustrated in Section 3.4.

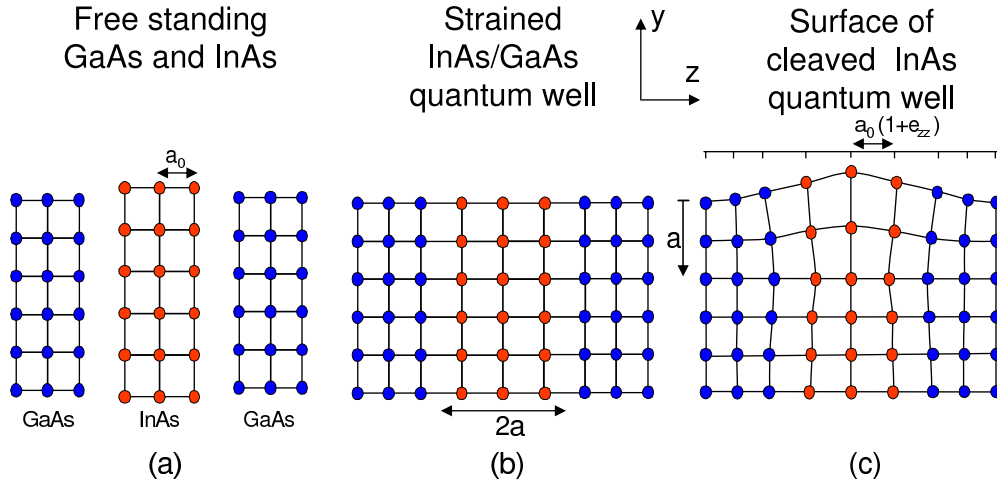


Figure 3.1: Strain relaxation at the cleaved surface of a strained quantum well. (a) Natural lattices of freestanding GaAs and InAs. (b) Due to lattice mismatch the InAs well is strained in GaAs. (c) The strain is released at the cleaved surface by outward relaxation.

3.1 Relaxation of a cleaved quantum well

Fig. 3.1 shows the strain relaxation of a cleaved InAs quantum well embedded in GaAs. The composition of the quantum well can be deduced from the bulk lattice spacing of the material (Fig. 3.1(b)). However, after cleavage, the region near the surface relaxes inhomogeneously to relieve its elastic energy, which results in a different spacing between the atoms near the surface compared to that in the bulk (Fig. 3.1(c)). A calculation of the relaxation is therefore required. Numerical methods must be used for a full solution but the elastic field in a cleaved sample that contains a single, uniform, strained layer or a superlattice, can be found analytically assuming a linear and isotropic elastic response.

For a quantum well (slab) with a width of $2a$ and its unstrained lattice constant exceeding that of the surrounding layers (cladding) by a fraction ϵ_0 , the following results can be obtained analytically [26]:

1. The lattice constant of the surface of the cladding is unaffected despite its distortion when the slab relaxes,
2. The lattice constant of the surface of the slab increases uniformly along the direction of growth z by a fraction $\epsilon_{zz} = (1 + 2\nu)\epsilon_0$ where ν is Poisson's ratio,
3. There is an outward relaxation of the surface given by:

$$u_y(z) = C - \frac{2(1 + \nu)\epsilon_0}{\pi} \left[(z + a) \log \left| \frac{z + a}{a} \right| - (z - a) \log \left| \frac{z - a}{a} \right| \right]. \quad (3.1)$$

An arbitrary constant C is present because the displacement does not decay at infinity. It can be shown [26] that while the slab relaxes to a greater thickness at the surface, it becomes thinner below it, and reaches a minimum width at a depth of $y \approx -a$, forming a neck as shown schematically in Fig. 3.1(c).

Previous X-STM measurements on a cleaved double $\text{In}_{0.05}\text{Ga}_{0.95}\text{As}/\text{GaAs}$ $\text{In}_{0.17}\text{Ga}_{0.83}\text{As}/\text{GaAs}$ quantum well, see Ref. [26], have shown a qualitative agreement with the theory. The prediction that the lattice constant of the cladding layers should be unaffected at the surface, while that of the quantum well is changed by a constant factor, was confirmed. Also, the shape of the outward relaxation of the cleaved surface was described well. The magnitude of the relaxation predicted by the calculations, however, was only 80% of that measured in the experiments. Several reasons for this discrepancy were considered [26]:

1. there are possible difficulties with the measurement of $u_y(z)$ (such as remaining electronic contrast, the size of the atoms, change in buckling behavior with composition),
2. deficiencies in the theory include the assumptions of isotropy, homogeneity, and linearity,
3. there may also be forces associated with the interfaces and surface, and piezoelectricity was neglected.

3.2 The effect of cubic symmetry on the relaxation of a cleaved quantum well

In order to explore the effect of cubic symmetry we have performed a calculation of the outward relaxation of the double $(\text{In,Ga})\text{As}/\text{GaAs}$ quantum well using the finite-element package ABAQUS. The direction of growth z lies along the cubic axis $[001]$ but the direction of the outward relaxation $u_y(z)$ points along $[110]$ or $[\bar{1}10]$, not $[010]$, i.e., the axes used to calculate the stress and strain are not the same as the cubic axes of the crystal. The stress-strain relaxations for this rotated situation differ from the usual cubic ones which only depend on the three independent coefficients $c_{1111}^{(cub)}$, $c_{1122}^{(cub)}$ and $c_{1212}^{(cub)}$. Instead they will look like those for an orthotropic material but with the following relations between the coefficients:

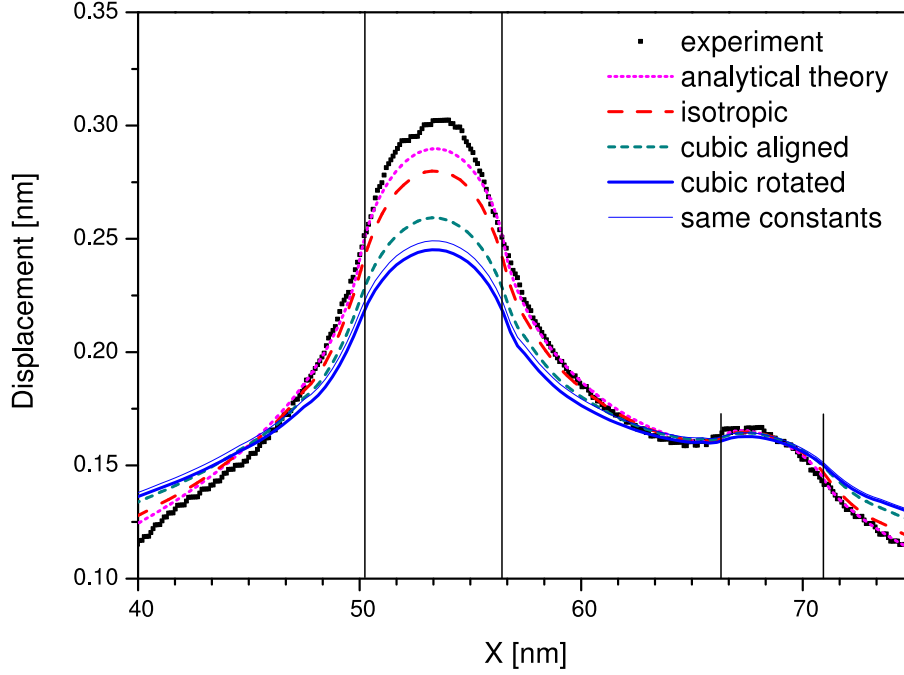


Figure 3.2: Numerical calculations of the outward relaxation of the surface of a cleaved double (In,Ga)As/GaAs quantum well, showing the effect of cubic symmetry and orientation. Also the influence of assuming the same elastic constants in both the quantum well and the cladding, and the experimental result are shown. The position of the wells is indicated by the vertical lines. The indium composition of the large well was taken to be 17.1% while for the small well 5% was used in the calculation.

$$\begin{aligned}
 c_{1111} &= c_{2222} = \frac{1}{2}(c_{1111}^{(cub)} + c_{1122}^{(cub)} + 2c_{1212}^{(cub)}) \\
 c_{3333} &= c_{1111}^{(cub)} \\
 c_{1122} &= \frac{1}{2}(c_{1111}^{(cub)} + c_{1122}^{(cub)} - 2c_{1212}^{(cub)}) \\
 c_{1133} &= c_{2233} = c_{1122}^{(cub)} \\
 c_{2323} &= c_{1313} = c_{1212}^{(cub)} \\
 c_{1212} &= \frac{1}{2}(c_{1111}^{(cub)} - c_{1122}^{(cub)})
 \end{aligned}$$

The effect on the calculated relaxation of cubic symmetry and orientation is shown in Figure 3.2 using the following elastic constants for GaAs: $c_{1111} = 119$ GPa, $c_{1122} = 53.4$ GPa, $c_{1212} = 59.6$ GPa and for InAs: $c_{1111} = 83.4$ GPa, $c_{1122} = 45.4$ GPa, $c_{1212} = 39.5$ GPa. The values for the (In,Ga)As quantum wells

are obtained by interpolation. We find that the outward relaxation is reduced by about 20% by cubic symmetry for a $\{001\}$ plane while rotation to a $\{011\}$ plane reduces the relaxation by a further 10%. The cause of these reductions in the outward relaxation is to be found in the effect of the different elastic constants which change with symmetry [27]. Thus, the results of the numerical calculations for cubic symmetry are further from the measurements than those calculated for isotropic material. Although inclusion of cubic symmetry, in principle, should lead to a better description, we find that this is not the case. Possibly, the inclusion of other effects such as nonlinear elasticity is needed, in order to obtain a better description. Because we obtain the best fit with the isotropic model, we will use this approximation in the remainder of this thesis.

3.3 Relaxation of a cleaved quantum dot

The outward relaxation of the surface of a cleaved quantum dot differs from that of a cleaved quantum well:

1. the position of the cleaved plane matters: the quantum dot has a finite size in all three dimensions and therefore the exact position of the cleavage plane with respect to the dot center determines which part of the dot contributes to the outward relaxation of the surface,
2. the lattice constant of the exposed cleaved dot surface is not uniform, but decreases in the surrounding matrix just above and below the dot; this will be the topic of the next section.

To illustrate the first point, the outward relaxation of the surface of the cleaved quantum dot as shown in Ref. [28] was calculated using the finite-element package ABAQUS for different cleavage planes with respect to the dot center. The dot was modeled as a truncated pyramid with a diagonal base length of 25.4 nm which decreases to 15.4 nm at the top of the dot, and a height of 5 nm. The indium composition was taken to increase linearly from 60% at the bottom to 100% at the top of the dot. Such a concentration gradient is consistent with X-STM measurements [28] and with the dipole moment as observed by photocurrent measurements [29, 30].

Fig. 3.4 shows the change in the outward relaxation when the position of the cleavage plane with respect to the dot center was changed from 0 nm to 14 nm above the dot center. Despite the fact that the exposed cleaved surface is smaller, the outward relaxation initially increases, since a larger part of the dot contributes to the relaxation. Even when the dot is completely buried, the effect of its strain field on the cleaved surface is still apparent. When the smaller part of the dot remains after cleavage, the outward relaxation and the size of the cross-section simply decrease as shown in Fig. 3.5.

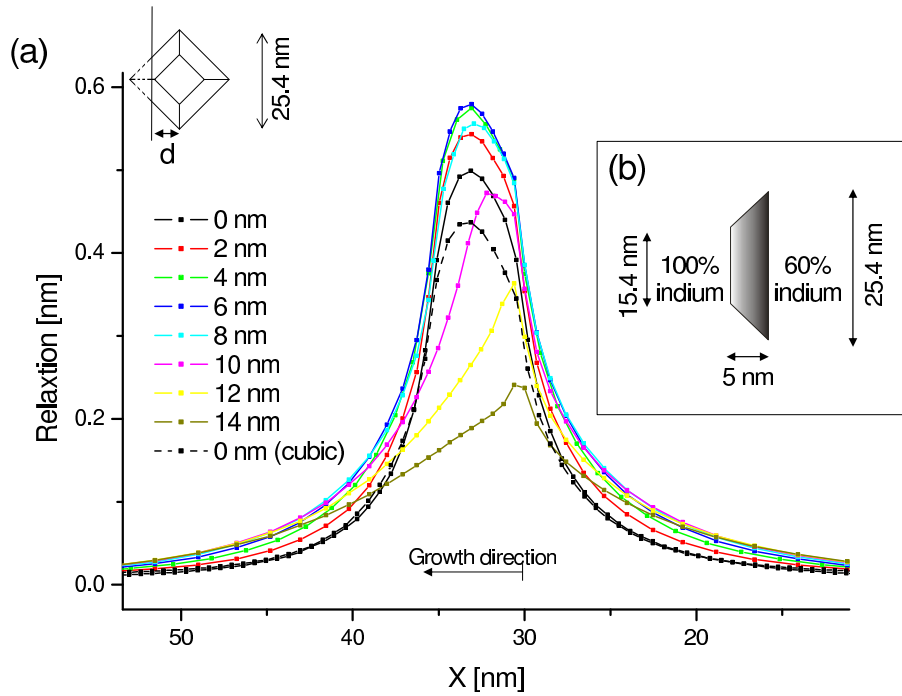


Figure 3.3: (a) Calculated outward relaxation profiles through the center of a cleaved (In,Ga)As dot in the growth direction. The different profiles are for different distances d of the cleavage plane to the center of the dot. The outward relaxation initially increases when a larger part of the dot becomes buried. (b) Schematic showing the size of the cross-section of the dot for $d = 0$ nm and its composition.

Fig. 3.3 shows the line profiles taken in the growth direction through the center of the dots, corresponding to Fig. 3.4. It can be seen that when the dot is cleaved near the center, the relaxation profile is asymmetric, with its maximum shifted in the growth direction, due to the increasing indium composition towards the top of the dot. When the dot is cleaved at a corner, the maximum in the relaxation profile shifts towards the base of the dot. It is clear that knowledge of the position of the cleavage plane is essential for the determination of the composition from the outward relaxation of the cleaved dot surface. However, in X-STM the quantum dots are cleaved at a random position with respect to the dot center. Only after scanning a large number of cleaved dots, the maximum base length of the cross-section of the dot can be determined, which is indicative for a cleavage near the dot center.

The calculated outward relaxation of the cleaved quantum dot is reduced by about 14% in the case that the effect of cubic symmetry is included, see the dashed curve in Fig. 3.3. The decrease in the outward relaxation would imply an increase in the average indium concentration of about 10% in order to achieve

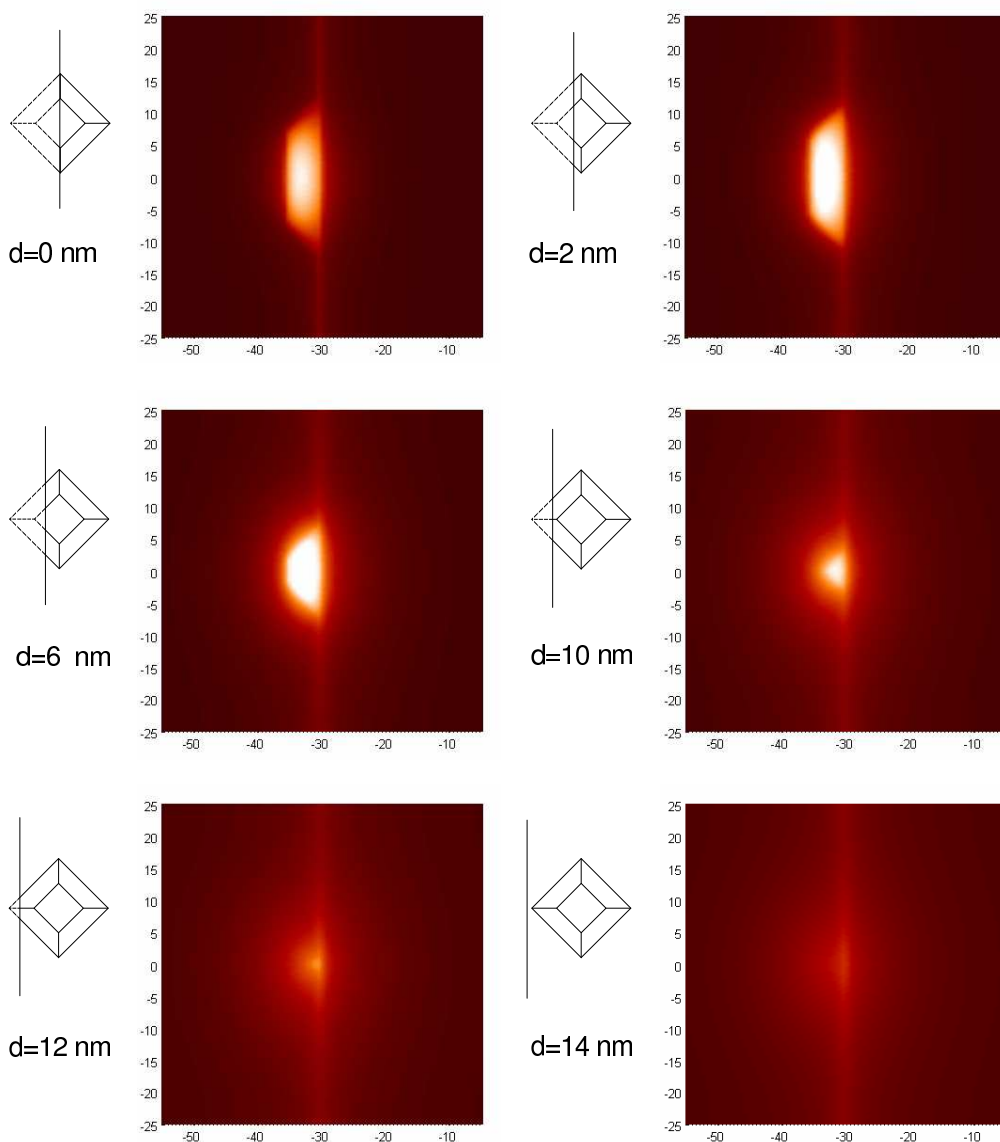


Figure 3.4: Calculation of the outward relaxation of the surface of a cleaved (In,Ga)As quantum dot and its wetting layer. The distance d of the cleavage plane to the dot center was changed from 0 nm to 14 nm. Despite the fact that the exposed cleaved surface is smaller, the outward relaxation initially increases, since a larger part of the dot's body contributes to the relaxation. Even when the dot is completely buried, the effect of its strain field on the cleaved surface is still apparent. The wetting layer was modeled as a 0.6 nm InAs layer.

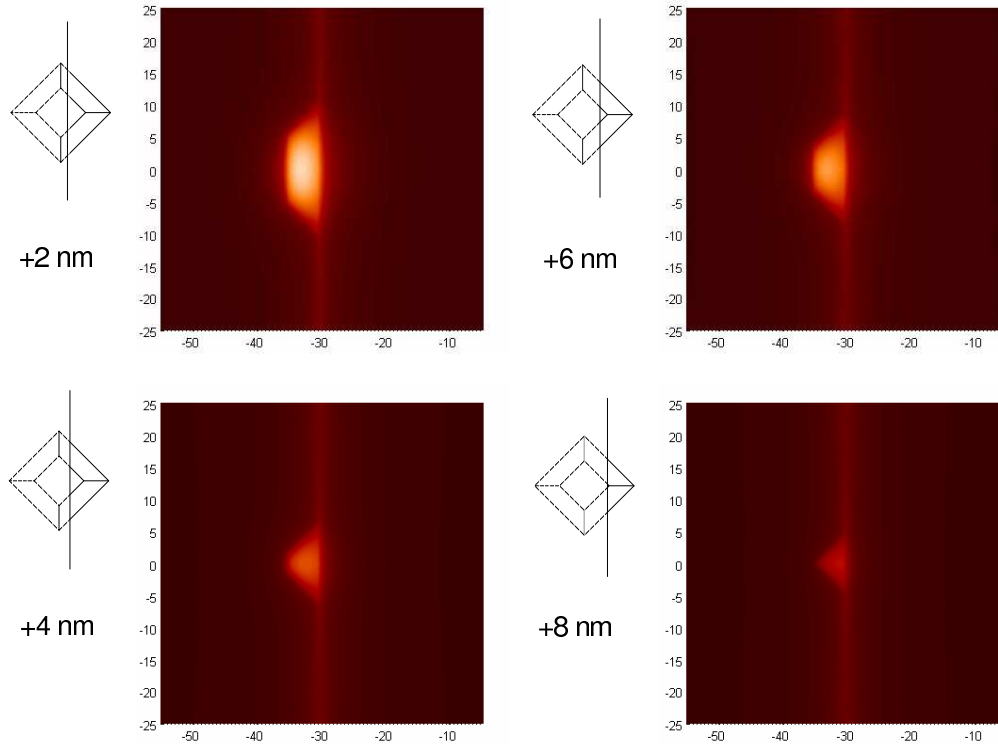


Figure 3.5: Calculation of the outward relaxation of the surface of a cleaved (In,Ga)As quantum dot and its wetting layer. The position of the cleavage plane was changed in such a way that only a corner of the QD is buried. The wetting layer was modeled as a 0.6 nm InAs layer.

agreement with the measured relaxation. Such an increase would imply that the indium profile is changed from 60%–100% to 80%–100%. This reduction of the indium concentration gradient disagrees with our results and those reported in Ref. [28]. As discussed in the previous section, we again find that the isotropic model results in a more realistic fit to the experimental data.

3.4 Calculation of the strain field of a cleaved quantum dot

To illustrate the second point made in the previous section, the strain field of the low-temperature-capped quantum dot shown in Chapter 10 was calculated using the isotropic model. The strain data was used to determine the shift of the atomic rows in and around the QD due to compressive strain. An X-STM topography image of the LT-capped QD is shown in Fig. 3.6(a). The shift of

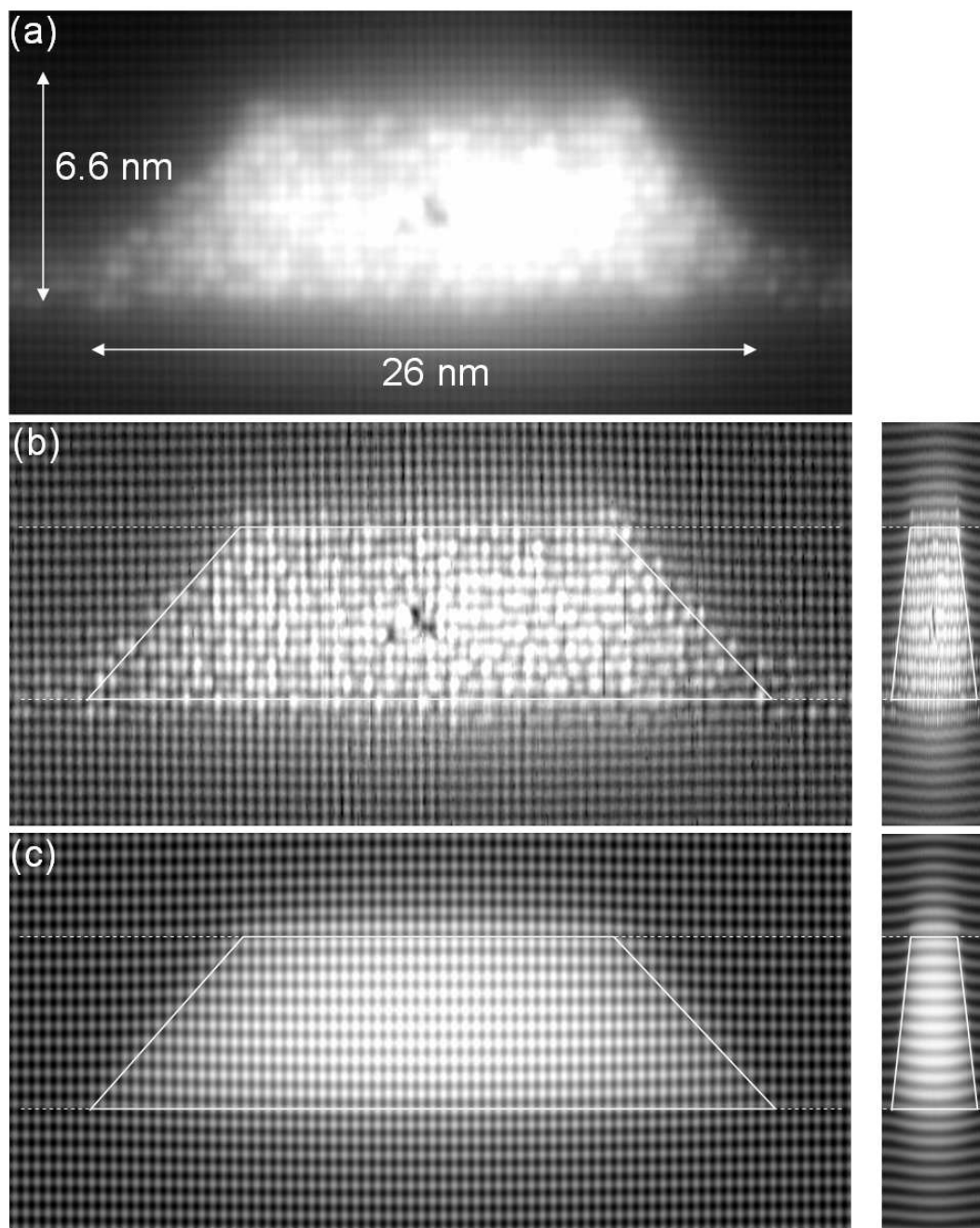


Figure 3.6: (a) X-STM topography image ($V_{\text{sample}} = -3\text{V}$) of a cleaved low-temperature capped QD, (b) same image treated with a local mean equalization filter with unsharp masking, showing the bending of the atomic rows of the cleaved (110) surface, due to compressive strain (c) simulated image based on the calculated strain and outward relaxation of the cleaved surface, using a homogeneous indium concentration of 70%.

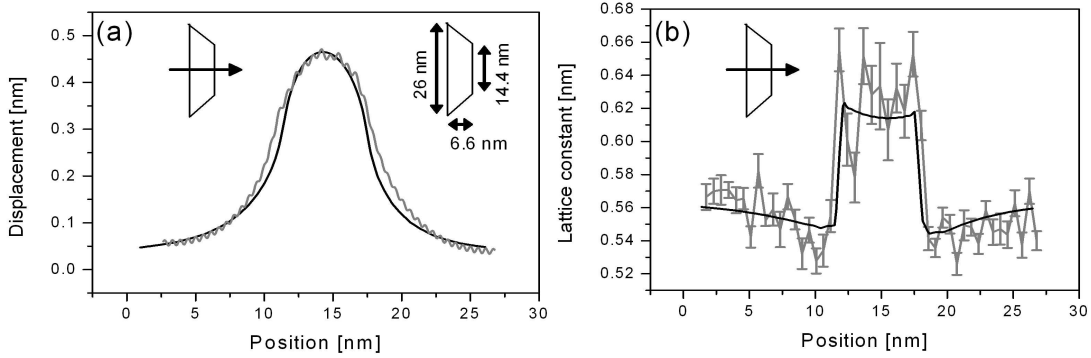


Figure 3.7: (a) Outward relaxation of a LT-capped QD measured along the growth direction, through the center of the cleaved QD surface, (b) Lattice spacing measured along the growth direction, through the center of the cleaved QD surface. The QD was modeled as a truncated pyramid with dimensions as shown and an indium concentration of 70%.

the atomic rows in and around the QD is most clearly seen after treating the topography image with a digital filter, which effectively enhances atomic details, as shown in Fig. 3.6(b).

The QD was modeled as a truncated pyramid with a height of 6.6 nm and a diameter of 26 nm that decreases to 14.4 nm at the top of the dot. A homogeneous indium distribution of $75 \pm 5\%$ was derived from the outward relaxation measured along the growth direction, through the center of the cleaved QD surface, as shown in Fig. 3.7(a). This result was verified by a comparison to the experiment of the lattice spacing measured along the growth direction, through the center of the cleaved QD surface, as shown in Fig. 3.7(b).

The effect of the strain field on the shift of the atomic rows in and around the QD, is visualized by a simulation of the atomic rows shown in Fig. 3.6(b), taking into account the deformation of the lattice by the compressive strain and the contrast change by the outward relaxation of the cleaved QD surface. The result is shown Fig. 3.6(c). From the good agreement between the calculated and the measured in-plane displacement of the atomic rows, it can be concluded that this displacement is a real topographic effect due to the strain field of the cleaved QD, which can be measured by X-STM topography.

3.5 Conclusion

X-STM topography enables the determination of the composition of nanostructures by the calculation of the outward relaxation and strain field of the cleaved

surface. For this calculation, a model based on isotropic, linear elasticity yields better results than a cubic model. A better agreement could probably be obtained by taking into account nonlinear elasticity. The outward relaxation of a cleaved quantum dot depends strongly on the position of the cleavage plane. This complicates the interpretation of X-STM images. For a homogeneous quantum dot distribution, it can be assumed that the quantum dot with the largest measured diameter is cleaved through or near its center. It was shown that the in-plane deformation of the atomic rows in and around a LT-capped QD as measured by X-STM can be attributed to its strain field.

4

Growth techniques, experimental setup and preparation procedures

This chapter starts with the description of the techniques used for the epitaxial growth of different semiconductor compounds for the formation of the nanostructures. It is then shown how pieces of the wafer containing the semiconductor nanostructures are prepared for the X-STM measurement and how an atomically flat cross-sectional surface is achieved. The atomic-scale analysis of the nanostructures is only possible by the use of an ultra-high-vacuum environment that keeps the cleaved surface free of contamination, and the reliable fabrication and scanning with STM tips.

4.1 Growth techniques and control

Molecular-beam epitaxy (MBE), chemical-beam epitaxy (CBE) and metal-organic vapor-phase epitaxy (MOVPE) are techniques that allow the epitaxial growth of different semiconductor compounds on a heated crystalline substrate.

In MBE the constituent elements of a semiconductor compound such as gallium arsenide (GaAs) are deposited using thermally evaporated elemental sources, the so-called Knudsen cells, while in CBE metal-organic compounds from a gas delivery system arrive at (or near) the growth surface where they react. An ultra-high vacuum system enables the collision-free transport of the beams, allowing for fast switching times by means of shutters, which allows the growth of heterostructures with atomically abrupt transitions from one material to another. When molecules arrive at the substrate, they can adsorb, migrate on the surface,

interact with other atoms, incorporate into the crystal, or desorb. The primary controllable factors that affect this process are the surface itself, the temperature of the substrate, and the incident fluxes. One of the most useful tools for in-situ monitoring of the growth is reflection high-energy electron diffraction (RHEED), which can be used for example to calibrate growth rates (which are in the order of one atomic layer per second) and to give feedback on surface morphology.

MOVPE (also known as metal-organic chemical vapor deposition or MOCVD) is another growth method capable of producing heterostructures of high quality. In contrast to MBE and CBE it does not require the use of an ultra-high vacuum system since it usually operates near atmospheric pressure. Different gases are passed through the reaction chamber using a hydrogen carrier gas. The composition of the gases can be varied rapidly to control the composition of the material grown. Because MOVPE has a faster growth speed compared to MBE or CBE, and can be scaled up to grow a large number of structures simultaneously, it is used for commercial production. MBE or CBE are usually used for scientific research.

4.2 Sample preparation, mounting and cleavage

Small rectangular pieces (about $3.5 \times 10 \text{ mm}^2$) are cleaved from a wafer containing the semiconductor heterostructure of interest. These wafers are normally 350–450 μm thick and are polished down with aluminum oxide powder to a thickness of about 100 μm , for easy cleavage. For an STM measurement it is essential to have good electric contact with the sample. Although the samples themselves are (semi-)conducting, a simple mechanical contact between sample and holder is not sufficient because of an insulating oxide layer on the sample surface. Therefore, Ge/Ni/Au contacts are evaporated at the top surface of the sample after treating it with a N_2/H_2 plasma.

A small scratch of about 0.5–1.5 mm, which extends to a small notch at the side of the sample, is made at the top surface of the sample using a diamond pen. This scratch facilitates the cleavage of the sample and provides a fixed starting point for the propagation of the cleavage plane.

The sample is clamped on a sample holder between two metal bars that can be screwed together, as shown in Fig. 4.1. Only one corner of the sample is clamped for the unconstrained propagation of the cleavage plane. Between the metal bars and the two surfaces of the sample, at the position where the sample is to be clamped, thin slices of indium are placed. The sample holder is heated in order to melt the indium before tightening the screws. The indium provides for an even pressure distribution on the sample, preventing it from cleaving during tightening of the screws and slipping out of the holder when the sample is degassed subsequently in the UHV system.

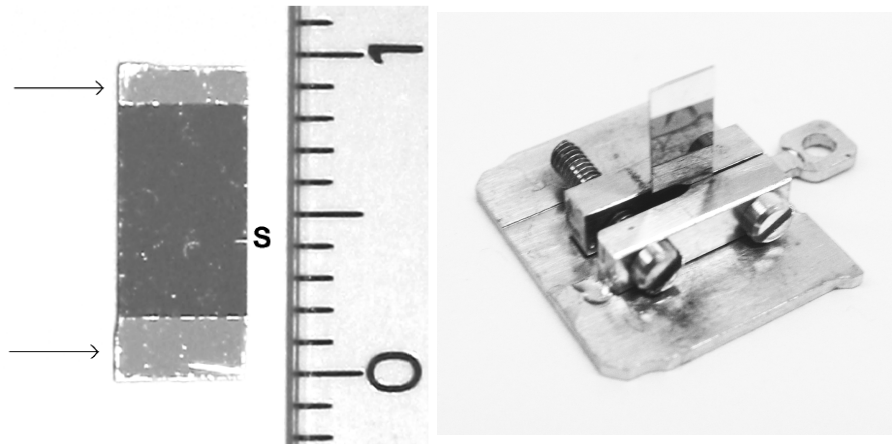


Figure 4.1: Top view of the sample with scratch S and Ge/Ni/Au contacts indicated by arrows. The size of the sample is about 1 cm as indicated by the ruler. On the right it can be seen how the sample is clamped in a sample holder.

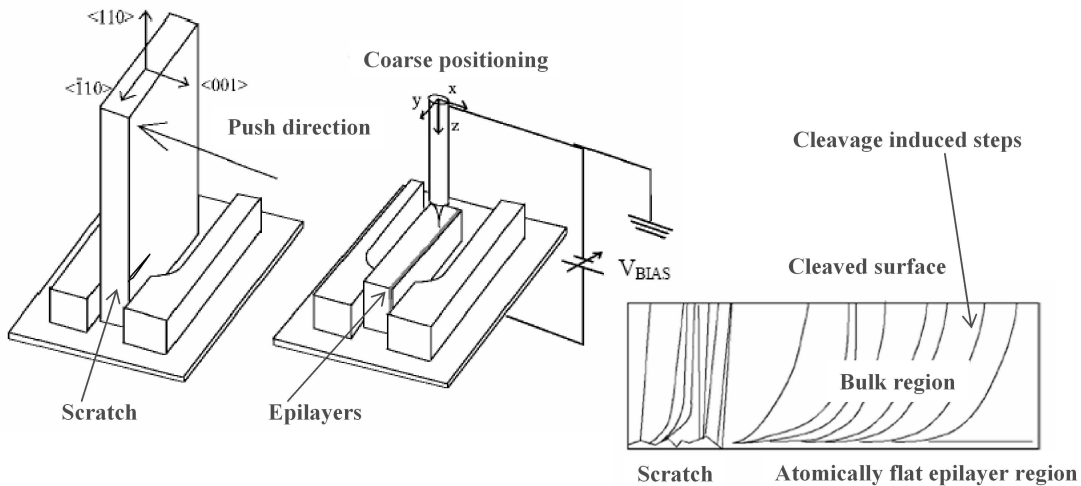


Figure 4.2: Schematic view of the sample cleavage process.

The sample is cleaved in the STM chamber using a gentle touch by a manipulator (the so-called “wobble stick”) just before the measurement as shown in Fig. 4.2(a). A characteristic crack pattern as shown in Fig. 4.2(b) may be observed [31]. For the samples analysed in this thesis, the region near the surface of the sample (epilayer region) is atomically flat. This is not always the case for very strained structures or hard materials. After cleavage, the sample is placed into the sample stage and moved towards a mounted tip, with the help of a CCD camera equipped with a tele-lens. When the sample is brought close to the tip,

the reflection of the tip in the cleaved surface becomes visible. After the tip and sample are properly aligned, further approach until tunneling contact can be done automatically by the system. Since the exact position of the tip with respect to the deposited structures cannot be determined optically, after the first tunneling contact, the tip is retracted and moved several 100 nm towards the edge of the cleavage surface where the grown layers (epilayers) are located. The process of making tunneling contact and moving towards the epilayers is repeated until the tip moves over the edge of the sample. At this point tunneling contact is not achieved, which indicates that the location of the epilayers is within several 100 nm.

4.3 Tip preparation

The tips are made of 99.97% pure polycrystalline tungsten wire with a diameter of 0.25 mm. A short piece of this wire (~ 5 mm) is spot welded onto an Omicron tip holder and cleaned for use in UHV. The tips are then electro-chemically etched with a 2.0 molar potassium hydroxide solution.

The top 1–1.5 mm of the tip is put into the solution and a positive voltage (4–5 Volt) is applied to the tip-wire. A platina-iridium (90%/10%) spiral serves as a counter electrode. The beaker glass in which the etching is performed has a vertical glass plate along its diameter that ensures that the flow around the tungsten wire is not disturbed by the hydrogen bubbles that are produced at the platina-iridium anode, as shown in Fig. 4.4. As the reaction products dissolve in the etchant, they sink down along the wire, which is visible from the local change of the diffractive index of the solution. The tail of reaction products drooping from the wire being etched, should hang straight down from the wire. Because of the geometry, the reaction velocity is the highest at the point where the tungsten wire penetrates the surface of the solution. This causes necking of the wire at the surface of the etching solution, as the reaction products flowing down the tip shield the rest of the wire. Eventually, the wire will break at the neck leaving a very sharp tip, as shown in Fig. 4.3. A current limiter is used to interrupt the etching process immediately ($< 1 \mu\text{s}$) after the breaking of the wire. It was found that for the reliable production of sharp tips, the height of the etching solution in the beaker glass is of critical importance, possibly for the unconstricted flow of reaction products. The tips are degassed after loading into the UHV system and treated with an 700 eV argon ion bombardment in order to mechanically stabilize the tip.

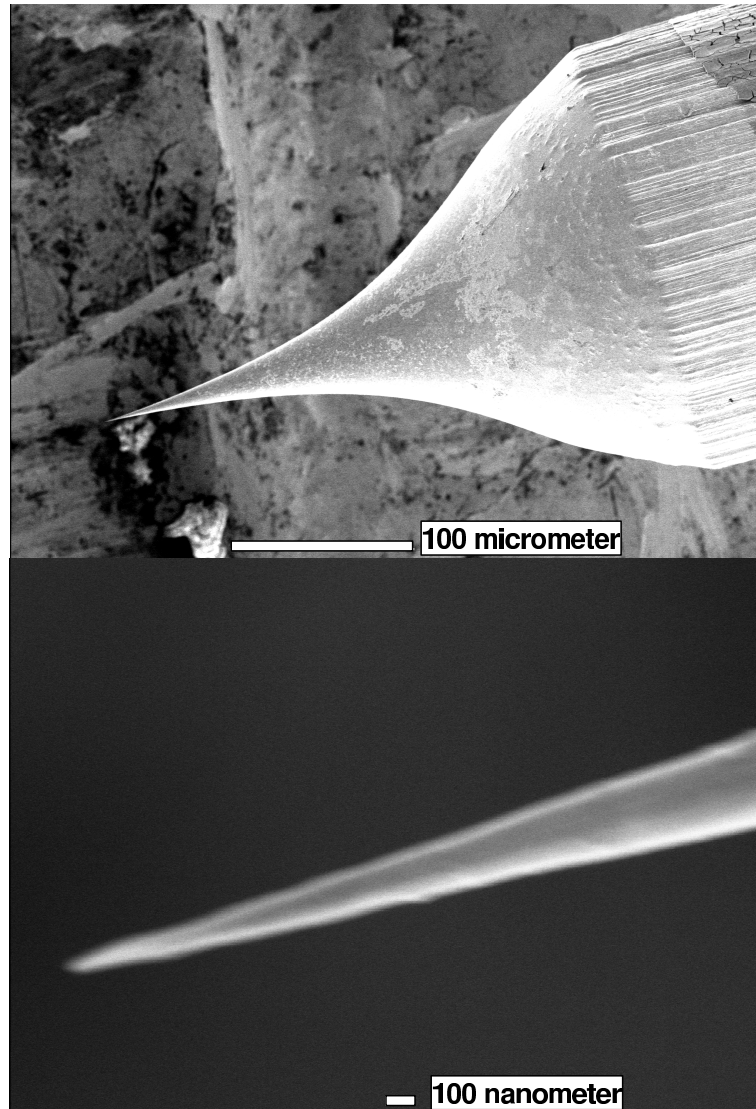


Figure 4.3: Scanning electron microscopy image of an etched STM tip at different magnifications.

4.4 The STM unit

A commercially available room-temperature STM unit (Omicron STM-1 TS2) is used. The heart of the STM unit, shown in Fig. 4.5, consists of a piezo scanner (A) on which the tip can be mounted, and a movable sample stage (B). The

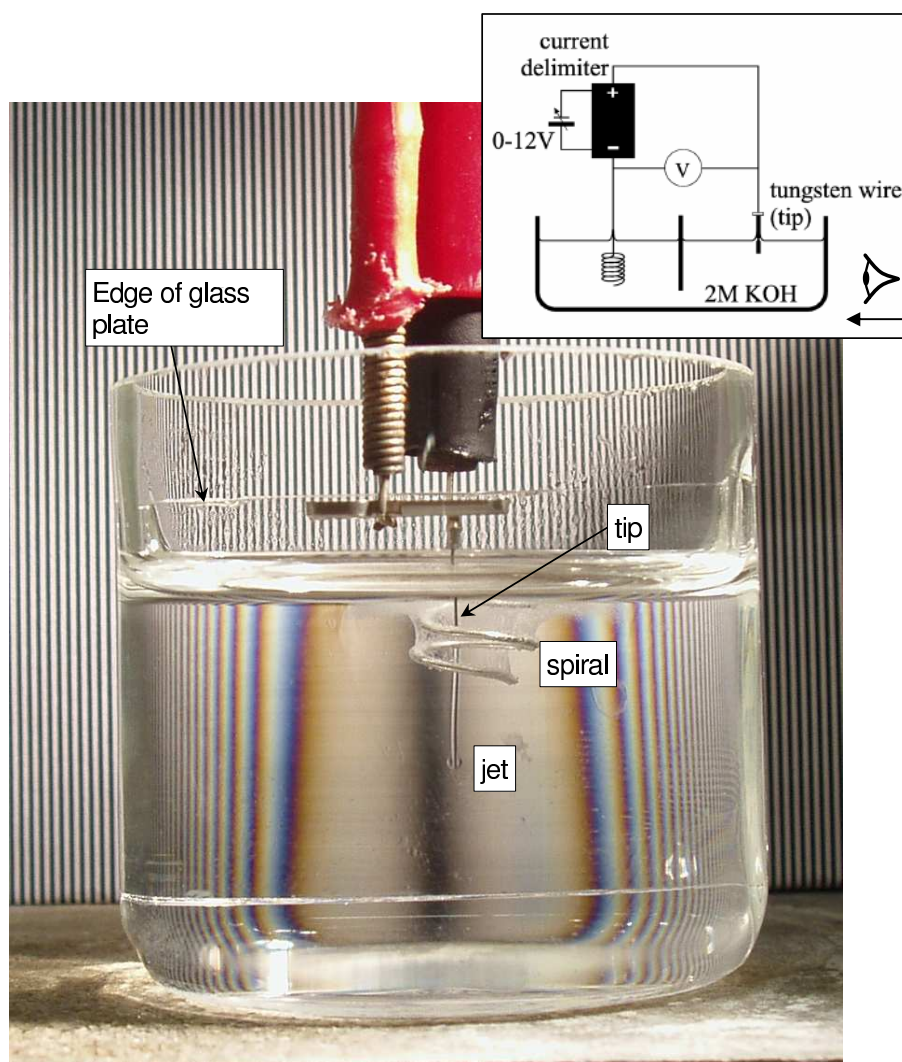


Figure 4.4: Photograph of a jet flowing down from the tip at the start of the tip etching process. The spiral is located behind the diagonal glass plate in the beaker glass, while the tip and jet are in the front. A vortex at the head of the jet can be seen. The jet is visualized by its different diffractive index from the etching solution, by using a patterned background. At the position of the spiral, the jet is not visible because the light coming from the patterned background is blocked by the spiral. This makes the spiral to appear in front of the jet.

movable sample stage is used to bring the sample in tunneling contact with the tip. The sample and tip are part of an electronic circuit that includes a feedback loop. The electronic circuit regulates the tunneling current by moving the tip up and down with respect to the sample surface by using the z piezo tube of the

scanner (A). Perpendicular to this direction, two other piezo tubes are used for scanning the tip over the sample surface. The tunneling current is amplified in the electronic circuit by a current-voltage converter (D).

The STM setup is very sensitive to external vibrations, as the tip-sample distance during tunneling is only a few Ångstrom. Moreover, the apparent height of the atomic corrugation visible in the STM images is only 20 pm. Therefore, the setup is vibration isolated with different damping systems. The scanner unit is suspended on a set of springs and stabilized by an eddy current damping system. The eddy current damping system consists of copper fins (C) that surround the scanner and that are placed between permanent magnets when the scanner unit is in its suspended position.

The STM unit, together with the rest of the setup, is mounted on a heavy metal tabletop. Rubber dampers between this tabletop and the supporting frame filter out high frequency vibrations. Low frequency vibrations are suppressed by four active damping elements that are mounted between the floor and the frame. In this active damping system several motion detectors are present and several actuator-coils that counteract the detected motion of the system. Finally, the entire setup is standing on a heavy concrete platform that is decoupled from the building.

4.5 The UHV system

Apart from the ability to scan the tunneling tip reliably and reproducibly over the surface of the sample, another factor of critical importance in cross-sectional scanning tunneling microscopy on III/V semiconductors, is the production of an atomically flat cross-sectional surface that is free of contamination/oxidation, in order to obtain an electronically unpinned surface. Therefore, cleavage of the samples and the subsequent measurement are performed in a home-built ultra-high vacuum setup.

The central vacuum chamber (STM), in which the STM unit is positioned, is pumped down by an ion-getter pump (IGP) with a titanium sublimation element (TSE) to a pressure lower than 5×10^{-11} Torr (Varian VacIon Plus, 300 liter/sec). During X-STM measurements the inner panel of the IGP/TSE can be cooled down with liquid nitrogen, which enhances the pump speed by a factor of two.

In the preparation chamber (PREP), which is separated by a valve from the STM chamber, the tips and samples can be degassed with a baking unit and tips can be treated with an argon ion bombardment. Two oil-free turbo-molecular pumps (Varian V-250 and V-70), installed in series, keep the preparation chamber at a pressure of approximately 6×10^{-10} Torr. The preparation chamber is connected to a load lock, for loading and unloading of the tips and samples without seriously affecting the pressure in the preparation and STM chamber. The load lock is pumped with one of the turbo-molecular pumps (V-70) to a

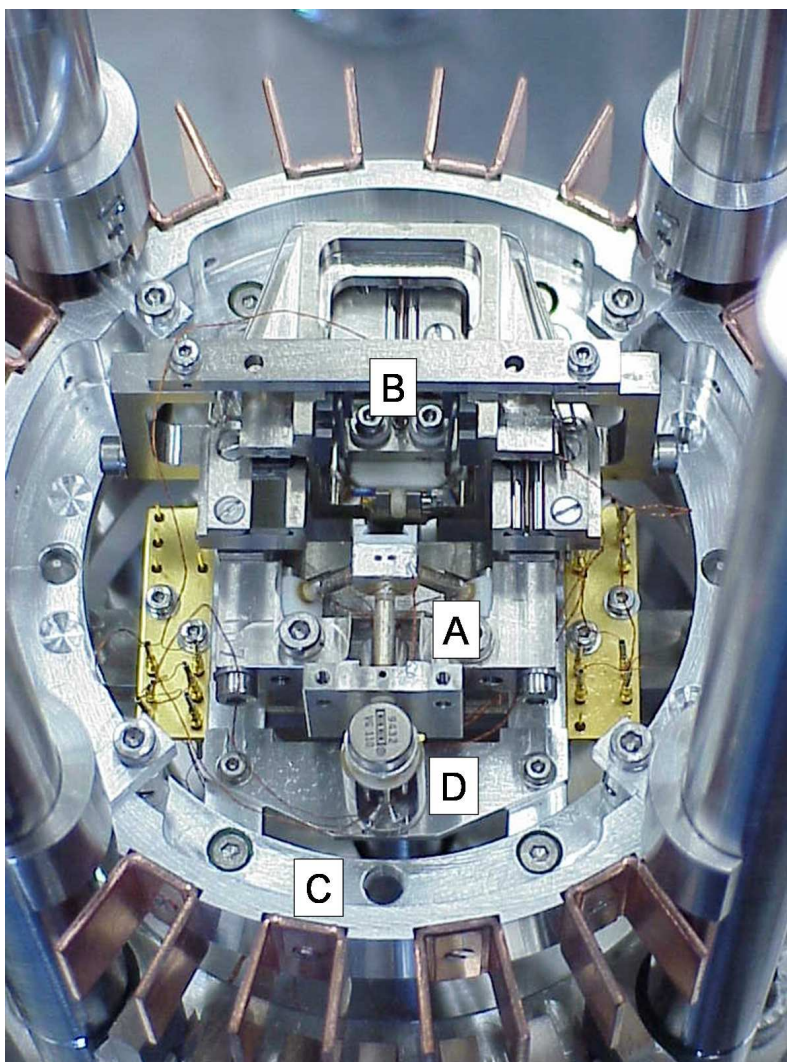


Figure 4.5: Omicron STM-1, TS2 scanner in the upper locked position. A: Tripod scanner, showing the 3 piezos, which are attached to the tip holder. B: Coarse-approach stage. The sample is placed in here, making it possible to move the sample in two dimensions towards the tip and towards the epilayers. C: Eddy current damping stage. The copper fins are located outside the ring. In the lowered position these fins are positioned between the magnets. D: Current amplifier. For noise reasons this amplifier is placed as close as possible to the tip, inside the UHV.

pressure of about 10^{-6} Torr. An XDS5 dry scroll pump provides the necessary pre-vacuum of about 10^{-1} Torr. During the X-STM measurements all pumps are switched off to prevent vibrations, except the IGP/TSE as this pump contains

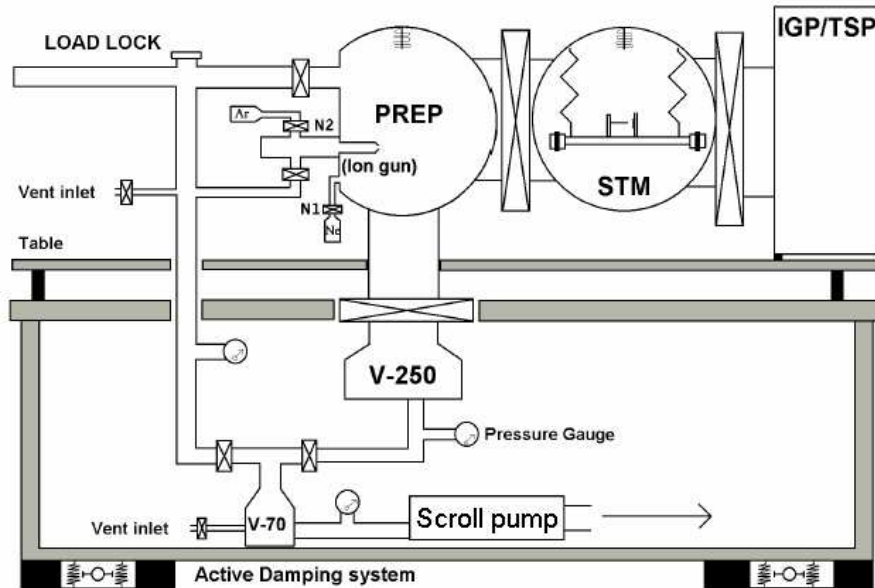


Figure 4.6: Schematic drawing of the UHV system containing the STM and damping system

no moving parts. Two wobble sticks in the STM and preparation chamber are used for manipulation and transportation of the tips and samples.

4.6 Summary

MBE, CBE and MOVPE are techniques that enable the growth of complex semiconductor nanostructures with a high degree of control. During the growth, processes such as surface migration, segregation and intermixing influence the size, shape and composition of the nanostructures. X-STM is a technique that enables the atomic-scale structural analysis of the effects of these processes after the completed growth of these nanostructures. In X-STM an atomically sharp metallic probe (tip) is brought in tunneling contact with the cleaved surface (cross-section) of the nanostructures, and scanned across it using a feedback loop that maintains a constant tunneling current. Reliable scanning and positioning of the tip is only possible by the use of an ultra-high-vacuum environment that keeps the cleaved surface free of contamination and a damping system that keeps fluctuations in tip-sample distance within a few picometers.

5

Indium incorporation in III/V semiconductor structures: an overview

Throughout this thesis, indium incorporation is the main issue that connects the different chapters, as it determines the sharpness of interfaces and the size, shape and composition of self-assembled nanostructures. The purpose of this chapter is to provide the reader with a short overview of different functional structures where indium migration plays a key role in the growth and hence the performance of the device. The work described in this chapter is part of a collaborative effort to disentangle the electronic and optical properties of self-assembled nanostructures [32, 33, 34, 35, 36, 37].

5.1 Structural quality of MOVPE grown InP based Quantum Cascade Lasers

The feasibility of metal-organic vapor-phase epitaxy (MOVPE) to produce the complex sequence of quantum wells and barriers making up a quantum cascade laser (QCL), was recently demonstrated [38]. MOVPE growth has several potential advantages over MBE for the commercialization of quantum cascade technology. These include the higher overall growth rates that are achievable, which can be varied during a growth run. This allows the active and bridging regions of a QCL to be grown at a reduced rate, providing excellent control of layer thicknesses, while the thick waveguide cladding layers can be rapidly deposited, significantly reducing the total growth time. Because MOVPE growth takes place close to atmospheric pressure, the maintenance of reactors is considerably

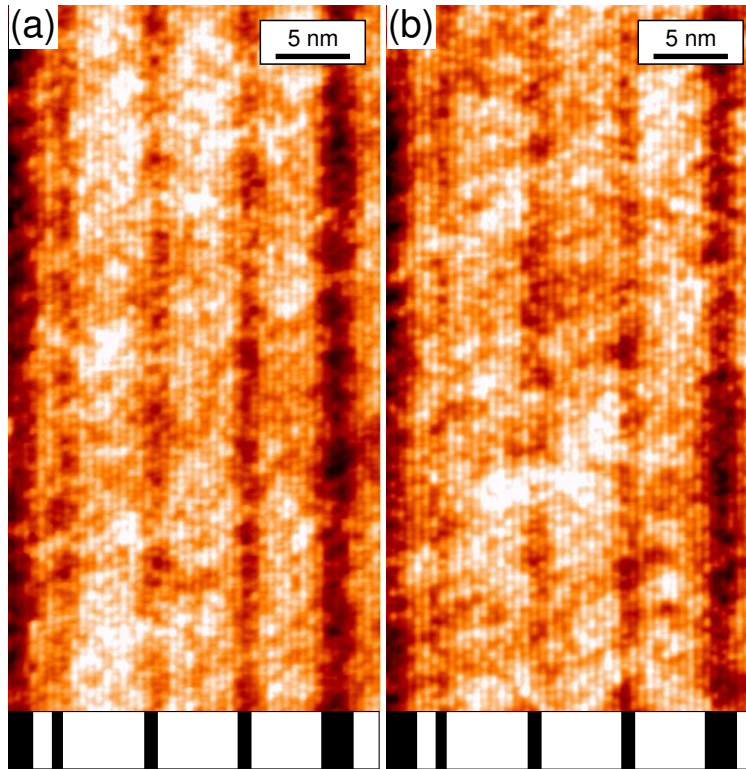


Figure 5.1: X-STM image of the active region of a MOVPE-grown [35, 36] (a) and a MBE-grown [32] (b) QCL. The active regions of both structures have the same layer sequence of 14/7/58/9/57/9/50/22 Å, where the InGaAs wells (bright) are indicated in roman, and the InAlAs barriers (dark) in bold. The layer sequence is indicated below the images.

simplified, and extended bake-out cycles are not needed in order to recover from atmospheric contamination. Furthermore, MOVPE provides an established route to high quality, multi-wafer growth of phosphide materials in planetary reactors.

Figure 5.1(a) shows an X-STM image of the active region of a MOVPE grown QCL structure [35, 36]. All layers can be clearly resolved and there is no evidence of interfacial undulation. This structure is to be compared with a state-of-the-art MBE-grown QCL with an identical layer sequence [32], shown in Fig. 5.1(b). It can be seen that the structural quality of the active regions of the two samples, as observed in these measurements, is almost indistinguishable. It is notable that the InGaAs/InAlAs interfaces obtained with the two growth techniques are of equivalent quality. These results show that the growth techniques of MOVPE and MBE are capable of providing material of the epitaxial quality needed for the production of high performance QCLs. This capability could have a significant impact on the prospects for future commercialization of QCL technology [35]. An

extensive structural analysis of the MBE-grown QCL with digitally graded and abrupt interfaces is presented in Chapter 7.

This work was done in collaboration with L. R. Wilson and R. P. Green, University of Sheffield, UK, and M. Beck, J. Faist and T. Aellen, University of Neuchâtel, Switzerland.

5.2 InGaAs/AlAsSb Quantum Cascade Lasers

The ultimate limit on short wavelength QCL operation is set by the depth of the quantum wells in the laser active region, i.e., the conduction band offset ΔE_c of the heterostructure material system used. Consequently, there is a strong motivation to extend the QCL concept to materials system with the highest possible E_c , such as InAs/AlSb [39] ($E_c \approx 2.1$ eV) and $\text{In}_{0.53}\text{Ga}_{0.47}\text{As}/\text{AlAs}_{0.56}\text{Sb}_{0.44}$ [40] ($E_c \approx 1.6$ eV). However, due to the very high complexity of QCL design, and the stringent demands placed on layer thickness control and uniformity, extension to these materials systems presents considerable challenges.

High resolution cross-sectional scanning tunneling microscopy (X-STM) measurements were made on an $\text{In}_{0.53}\text{Ga}_{0.47}\text{As}/\text{AlAs}_{0.56}\text{Sb}_{0.44}$ QCL structure MBE-grown on InP and emitting at $4.4 \mu\text{m}$ [37]. For this structure, laser emission was observed in pulsed regime, up to a maximum temperature of ~ 240 K, and found to be strongly dependent upon the thickness of the $\text{AlAs}_{0.56}\text{Sb}_{0.44}$ injection and exit barriers of the active region.

Figure 5.2 shows a high-pass filtered X-STM image of the QCL structure, with the optically active region visible in the center. The layer sequence is shown below the image. In the image, Sb atoms are represented by the brightest spots. It can be seen that Sb atoms are incorporated mainly in the barriers. This shows that the interface quality of InGaAs/InAlSb structures is comparable with typical MBE-grown InGaAs/InAlAs QCLs.

This work was done in collaboration with L. R. Wilson, D. G. Revin and R. P. Green, University of Sheffield, UK.

5.3 (In,Ga)As sidewall quantum wires on shallow-patterned InP (311)A

Nanometer-scale structures on patterned substrates such as V-grooves or sharp ridges have been widely studied to fabricate uniform quantum wires (QWires) and quantum dots with precisely controlled position and emission energy for opto-electronic devices. A technique that allows the formation of QWires in the InGaAs/InP material system, which is technologically important for opto-electronic devices, is the growth of highly uniform quasi-planar (In,Ga)As sidewall

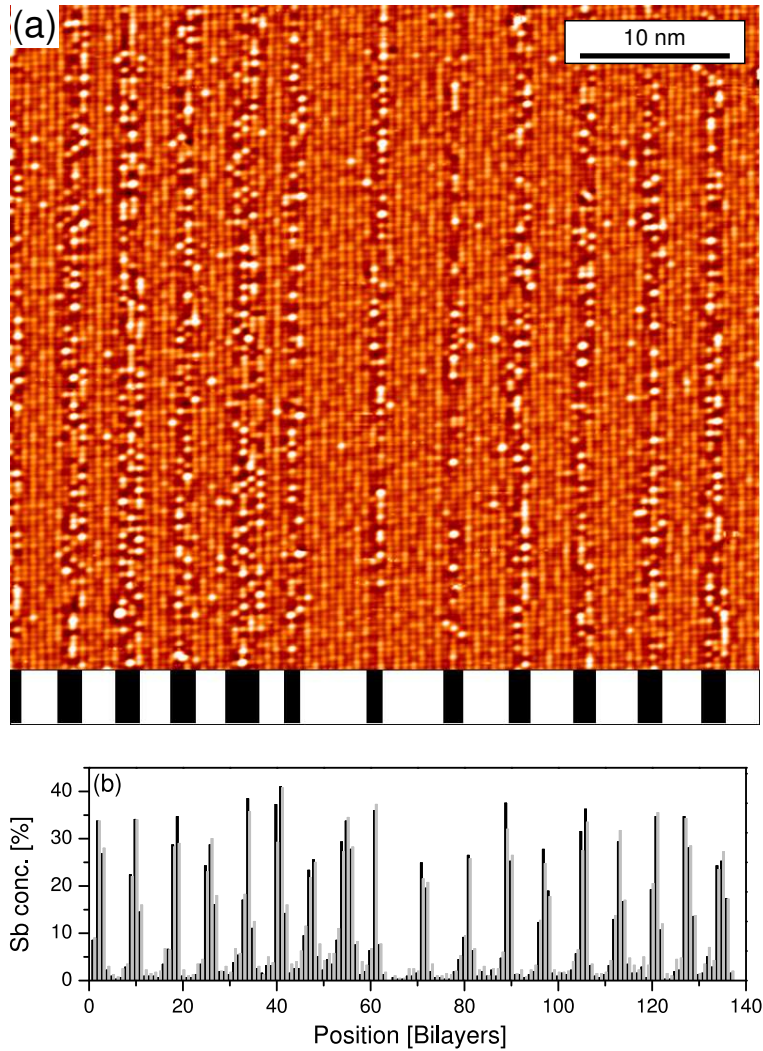


Figure 5.2: (a) High-pass filtered X-STM image of an $\text{In}_{0.53}\text{Ga}_{0.47}\text{As}/\text{AlAs}_{0.56}\text{Sb}_{0.44}$ QCL structure). The sequence of the $\text{AlAs}_{0.56}\text{Sb}_{0.44}$ barriers (black) and $\text{In}_{0.53}\text{Ga}_{0.47}\text{As}$ wells (white) is shown below the image. Bright spots in the barriers correspond to Sb atoms. (b) Sb count histogram. The two data sets shown (black and grey bars) are from a 80×165 nm image using slightly different threshold values for counting.

QWires by chemical beam epitaxy (CBE), on shallow $[01\bar{1}]$ stripe-patterned InP (311)A substrates [33].

Figure 5.3(a) shows an X-STM filled states topography image of a stack of three sidewall QWires formed by 10 nm thick (In,Ga)As layers at a 35 nm high mesa stripe marked by the first (In,Ga)As layer. The structure was grown by D. Zhou. After 100 nm InP buffer layer growth, the sidewall develops a smooth curved profile, which provides the template for (In,Ga)As QWire formation. A

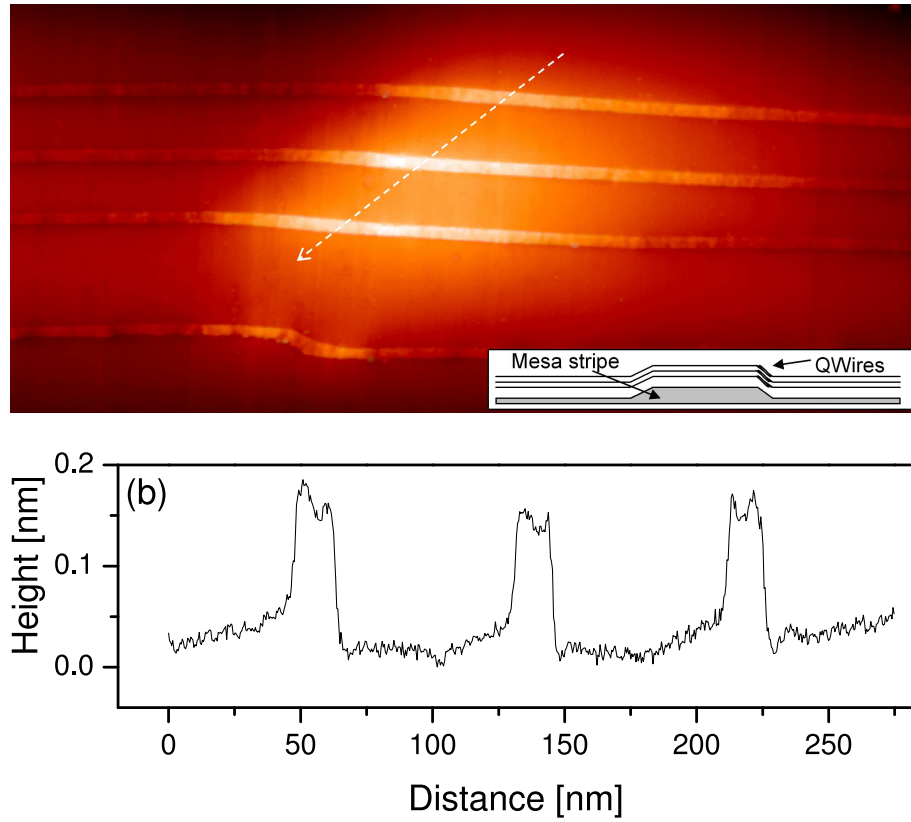


Figure 5.3: (a) X-STM image of three sidewall QWires formed by 10 nm (In,Ga)As layers embedded in InP on a patterned InP (311)A substrate, viewed along $[01\bar{1}]$. The dotted line indicates the direction and position of the line profile shown in (b). A second order polynomial background correction was applied to the line profile for a comparison of the height of the QWires at the indicated position. The inset in (a) shows a schematic view of the structure.

schematic of the structure is shown in the inset of Fig. 5.3(a). The QWires exhibit a distinct thickness enhancement close to the sidewall to a maximum of 12–13 nm with an extension at the mesa bottom. This enhancement of the thickness is accompanied by In enrichment, as indicated by the height (brightness) change along the QWire width. The compressive strain due to the In enrichment leads to a proportional outward bending of the In containing structure at the cleavage plane [Fig. 5.3(b)], which results in the observed brightness contrast. An effective width of the tapered QWire of 200 nm is measured from the full-width at half-maximum of the thickness or In composition change along the cross-section of the QWire. The QWire thickness increase by a factor of 1.2–1.3 confirms the strong preferential migration of In and Ga adatoms from the planar areas towards the

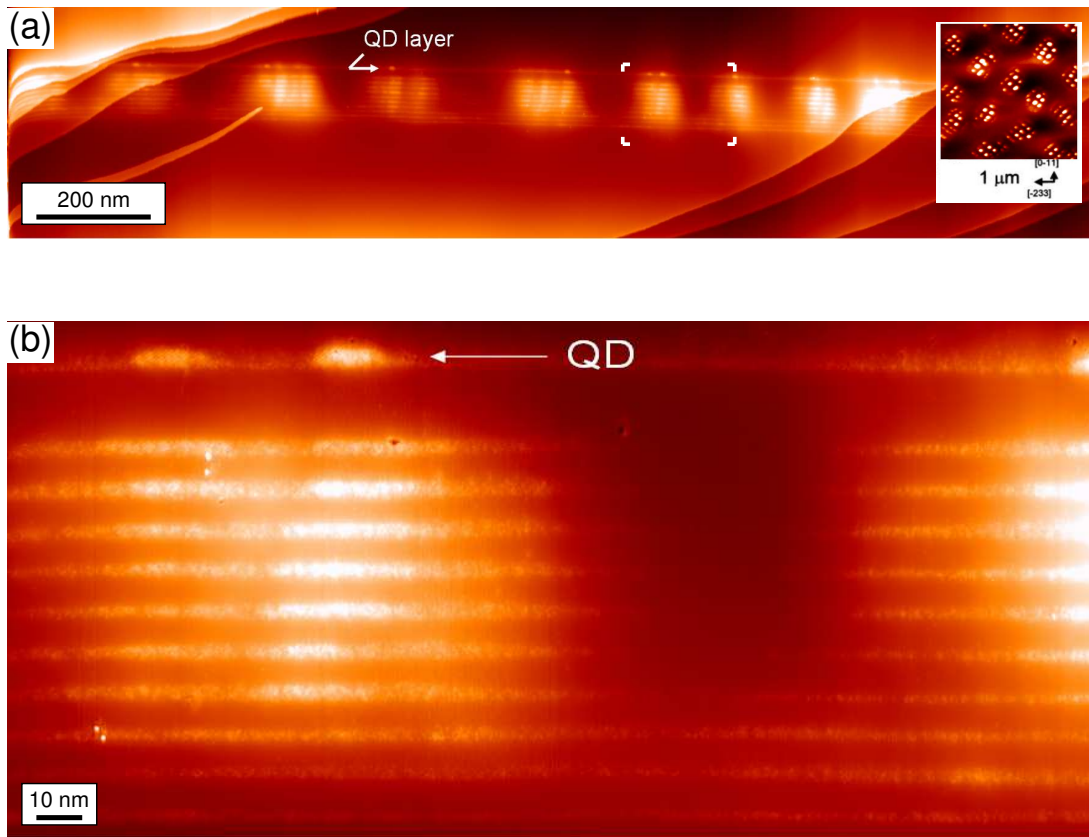


Figure 5.4: (a) X-STM image of InAs quantum dot molecules grown by self-organized anisotropic strain engineering of an (In,Ga)As/GaAs superlattice (SL) template on GaAs (311)B by molecular-beam epitaxy. The inset shows an AFM image [41] of the uncapped quantum dot molecules. (b) Enlarged view of the indicated part of the image showing small and large scale variations in the indium composition. The top InAs layer of the structure shows the formation of QDs. The positions of these QDs correspond to the indium-rich regions below the top InAs layer.

mesa sidewall, which is accompanied by In enrichment due to the larger In adatom migration length.

5.4 Ordered quantum dot molecules formed by self-organized anisotropic strain engineering

An ordered lattice of lateral InAs quantum dot molecules can be created by self-organized anisotropic strain engineering of an (In,Ga)As/GaAs superlattice (SL) template on GaAs (311)B by molecular-beam epitaxy [41]. It was shown that

during stacking, the SL template self-organizes into a two-dimensionally ordered strain modulated network on a mesoscopic length scale. InAs QDs preferentially grow on top of the nodes of the network due to local strain recognition. The QDs form a lattice of separated groups of closely spaced ordered QDs whose number can be controlled by the GaAs separation layer thickness on top of the SL template. Fig. 5.4(a) shows an X-STM image of the InAs quantum dot molecules. The structure was grown by T. v. Lippen. A large scale periodic (~ 200 nm) ordering can be clearly seen in the image by the enhanced contrast from indium-rich regions, due to lateral strain-driven mass transport during growth. Fig. 5.4(b) shows an enlarged view of an indium-rich region. Within the indium-rich region, a variation in indium composition at a length scale of less than 50 nm can be distinguished, which probably determines the ordering of individual quantum dots.

5.5 Formation of columnar (In,Ga)As quantum dots on GaAs(100)

Columnar (In,Ga)As quantum dots (QDs) with homogeneous composition and shape in the growth direction are realized by molecular-beam epitaxy on GaAs (100) substrates [34]. The columnar (In,Ga)As QDs are formed on InAs seed QDs by alternating deposition of thin GaAs intermediate layers and monolayers of InAs with extended growth interruptions after each layer. The height of the columnar (In,Ga)As QDs is controlled by varying the number of stacked GaAs/InAs layers. With increase of the aspect ratio of the columnar QDs, the emission wavelength is redshifted and the linewidth is reduced [34].

Figure 5.5 shows a X-STM image of a columnar (In,Ga)As QDs with eight stacked GaAs/InAs layers overgrown by a 5 nm $\text{In}_{0.2}\text{Ga}_{0.8}\text{As}$ strain reducing layer. The structure was grown by J. He. From the height contrast in the image, it can be seen that also in and above the strain reducing layer indium accumulation occurs, at the top of the columnar dot. The height contrast, in addition to the contrast from the bilayer atomic corrugation, originates from the outward bending of the compressively strained (In,Ga)As structure at the cleavage plane which is directly related to the In composition. The columnar QDs are vertical, confirming the strain correlated QD leveling and rebuilding [42] during GaAs/InAs multilayer growth. Most important, the In composition in growth direction is uniform within the detection limit of at most 5% variation within each period.

5.6 Conclusion

In this chapter, several examples of nanostructures were presented. In the QCL structures indium migration plays an important role in the roughness of interfaces

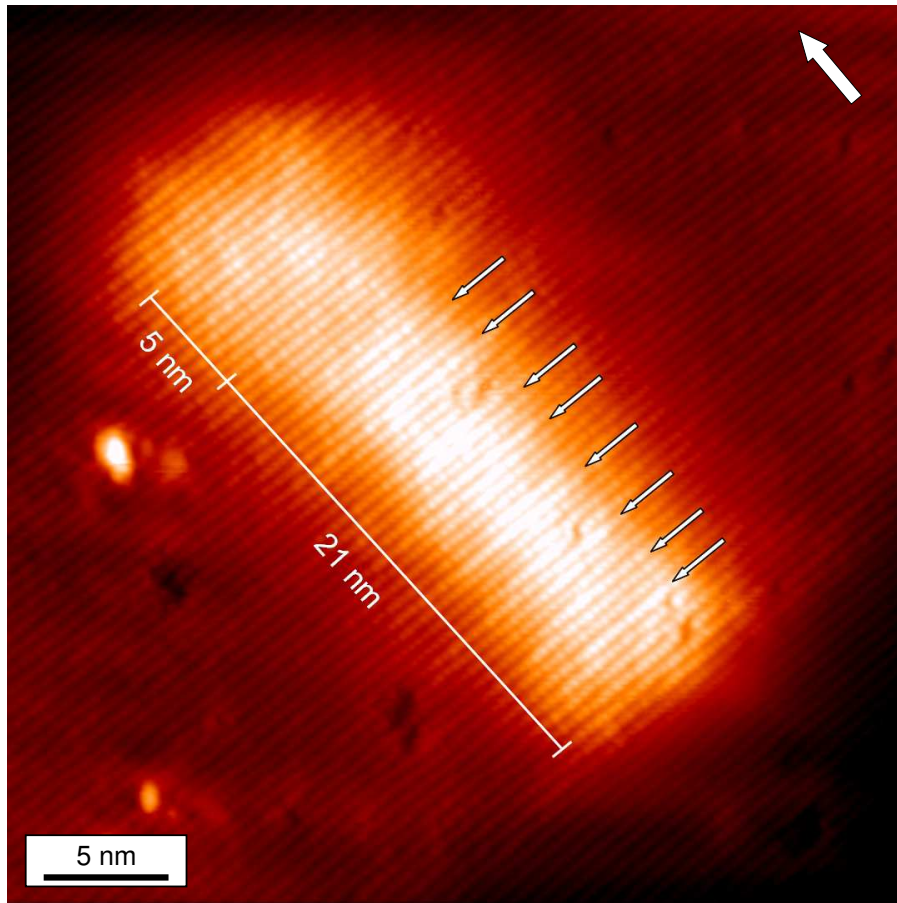


Figure 5.5: X-STM image of the columnar (In,Ga)As QD formed by eight stacked 2 nm GaAs/1 ML InAs layers on the 2 ML InAs seed QD and overgrown by 5 nm $\text{In}_{0.2}\text{Ga}_{0.8}\text{As}$ on GaAs(100) substrate. The small arrows indicate the GaAs/InAs periods. The large arrow indicates the growth direction.

and the homogeneity of the barriers and wells. It is shown that the use of Sb in the barrier material of a QCL does not lead to interfacial degradation or layer inhomogeneity. The formation of QWires on a patterned InP (311)A substrate by preferential migration of In (and Ga) at the mesa sidewalls, accompanied by In enrichment, was confirmed using STM topography, which is sensitive for the outward relaxation of the cleaved surface due to compressive strain. Strain-driven In migration is the primary mechanism in the formation of the QD molecules and columnar QDs.

6

Annealing of (In,Ga,Al)As digital alloy

We have investigated the structural properties of as-grown and annealed (750°C and 800°C) digital alloy (In,Ga,Al)As ($\lambda = 1.3 \mu\text{m}$) laser structures by cross-sectional scanning tunneling microscopy (X-STM). We show that it is possible to resolve the digital alloy period in the as-grown sample and the 750°C annealed sample. The 800°C annealed sample did not show the digital alloy period because of intermixing of the digital alloy. In the 750°C annealed sample only slight intermixing occurred. The barrier/well interface roughness of the as-grown sample was similar that of the 750°C annealed sample. Annealing at 800°C showed large barrier/well interface roughness and lateral composition modulation due to the phase separation of InGaAs/InAlAs alloys.

6.1 Introduction

Digital (In,Ga,Al)As alloys, lattice matched to an InP substrate, have been used successfully to construct laser structures without the need for additional source cells or laborious changes of cell temperature during growth with molecular-beam epitaxy. With this technique, (In,Ga,Al)As alloy layers are formed by sequentially depositing (fractions of) monolayers of separate alloys which can be either ternary (InGaAs/InAlAs) or binary (InAs/GaAs/AlAs). The resulting deposited layers have on average, a quaternary composition [43].

A possible drawback of digital alloys, however, is the introduction of many heterojunction interfaces of the short period superlattice (SPS). Probably more important is the fact that the optimum growth temperature (T_g) in view of the congruent sublimation temperature (T_{cs}) of the ternary InGaAs alloy, is lower

than the T_{cs} of the InAlAs alloy. The congruent sublimation temperature T_{cs} of a binary compound, e.g., GaAs, is the temperature at which equal numbers of Ga and As atoms sublime from the substrate surface. Most III–V binary layers grown significantly below their respective T_{cs} are severely degraded. To prevent degradation of the InGaAs alloy by In evaporation, the growth temperature is limited to about 510°C. This leads, however, to the incorporation of nonradiative recombination centers in the unintentionally low-temperature-grown InAlAs alloy. It has been suggested that rapid thermal annealing (RTA) removes most of the nonradiative recombination centers [44].

We report cross-sectional scanning tunneling microscopy measurements of as-grown and annealed digital alloy (In,Ga,Al)As 1.3 μm laser structures. Room temperature (RT) photoluminescence (PL) measurements have previously shown that after annealing at a temperature of $T_{\text{RTA}} = 620^\circ\text{C}$ to 750°C there is a huge increase of the PL intensity and a small (10 meV) blueshift of PL peak energy. At $T_{\text{RTA}} = 800^\circ\text{C}$ PL measurements have shown degraded PL intensity. The blueshift has been attributed to slight intermixing of gallium and aluminum in the InGaAs/InAlAs short period superlattice interfaces. The degraded PL intensity of the $T_{\text{RTA}} = 800^\circ\text{C}$ annealed structure has been attributed to roughening of the barrier/well interfaces [45]. With X-STM we have found direct evidence for the smoothing of the short period superlattice at and above $T_{\text{RTA}} = 750^\circ\text{C}$ and strong roughening of the MQW interfaces at $T_{\text{RTA}} = 800^\circ\text{C}$. With X-STM we did not find any evidence for non-radiative recombination centers (vacancies), because of the low density of these features and the difficulty of distinguishing them in the alloyed material.

6.2 Sample description

The digital alloyed (In,Ga,Al)As layers were grown by MBE on an epi-ready n-InP substrate, see Fig. 6.1. The layers were grown at a growth temperature of 510°C. Details of the grown structure and growth conditions are described elsewhere [44]. The wafer was covered with a 1500 Å SiO_2 layer to prevent re-evaporation of arsenic during RTA. Annealing was done in a nitrogen atmosphere for 30 seconds at 750°C and 800°C. The samples were grown at the Kwangju Institute of Science and Technology, Korea.

6.3 Results

In Fig. 6.2(a) we show a STM image of a digitally grown $(\text{InGaAs})_x(\text{InAlAs})_{1-x}$ MQW structure. Figure 6.2(a) was taken at a negative sample bias of -1.5 V, showing the filled states associated with the As sites. The bright regions are the 93.8 Å $(\text{InGaAs})_{0.8}(\text{InAlAs})_{0.2}$ well layers and the dark regions are the 65.6 Å

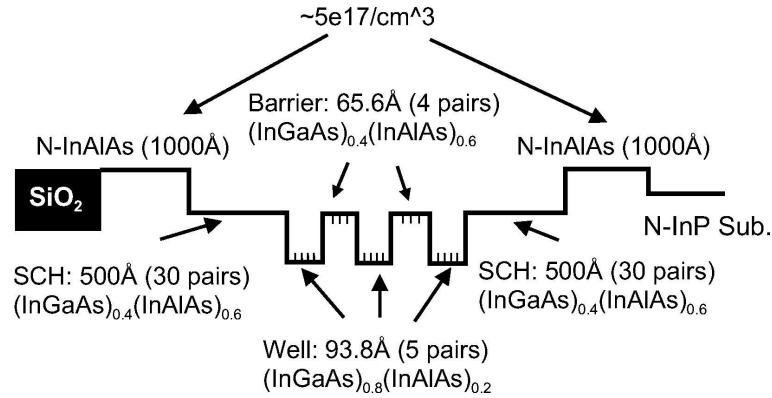


Figure 6.1: Schematic of the sample structure. The separate confinement and barrier $(\text{InGaAs})_{0.4}(\text{InAlAs})_{0.6}$ layers were formed by alternate deposition of 6.6 \AA thick InGaAs and 9.8 \AA thick InAlAs layers. The $(\text{InGaAs})_{0.8}(\text{InAlAs})_{0.2}$ wells were formed alternate deposition of 15 \AA thick InGaAs and 3.75 \AA thick InAlAs layers. All these layers are lattice matched to InP.

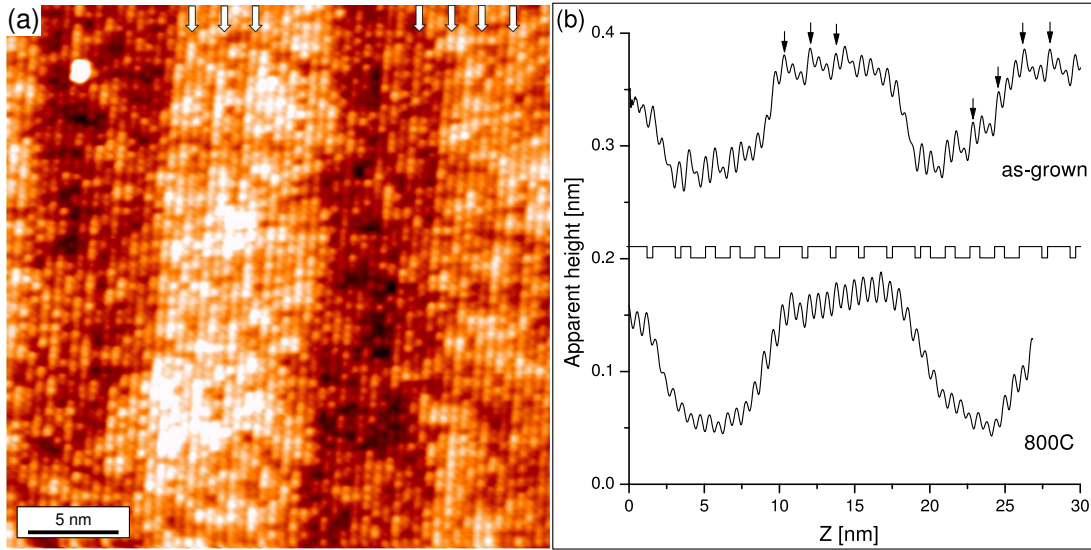


Figure 6.2: (a) $30 \times 30 \text{ nm}^2$ filled states topography image of as grown-sample showing two barriers and two wells, $V_{\text{sample}} = -1.5 \text{ V}$. (b) Averaged line profiles of the MQW region of the as-grown and the $T_{\text{RTA}} = 800^\circ\text{C}$ annealed sample at $V_{\text{sample}} = -1.5 \text{ V}$. The as-grown line profile shows the digital alloy period, indicated by arrows that correspond to those in the image. No digital alloy period is present in the line profile of the 800°C annealed sample which indicates intermixing of the short-period-superlattice after annealing. The curves are vertically shifted.

(InGaAs)_{0.4}(InAlAs)_{0.6} barrier layers. The observed contrast between the barrier and the well layers is due to the band offset between the well and the barrier layers which causes an electronic contribution to the tunneling current at low sample bias ($V_{\text{sample}} > -2 \text{ V}$). Clearly visible is the period of the digital alloy, which is approximately 3 atomic bilayers.

Figure 6.2(b) shows a line profile averaged perpendicular to the growth direction. In the well and barrier layers, 5 and 4 pairs of digital alloy can be distinguished, respectively. This is in agreement with the structure design as indicated in Fig. 6.1. Also shown in Fig. 6.2(b) is the averaged line profile of the MQW region of the 800°C annealed sample. No digital alloy period can be seen in the line profile which indicates that intermixing of the SPS's occurs after annealing. The intermixing is assumed to cause a blueshift of the PL spectrum after annealing of these structures [45].

Generally, contrast in STM images is mostly determined by electronic contributions to the tunneling current. It has been suggested that for the material system InP/GaAs/InAs it is possible to minimize electronic effects by applying either a high ($V_{\text{sample}} > +2 \text{ V}$) positive sample bias or a high negative sample bias ($V_{\text{sample}} < -2 \text{ V}$) [23, 24].

Figure 6.3(a) and 6.3(b) show high voltage (-3 V) filled states images of the as-grown and the 800°C annealed structure. The images have the same height scale with a maximum of 180 pm. The image of the as-grown sample shows almost no electronic effects as the barrier and well regions show almost no contrast. The topography is as expected for a homogeneous alloy. The image of the 800°C annealed structure, however, shows strong lateral corrugation modulation and roughening of the barrier/well interfaces. The roughening of the interfaces is attributed to barrier/well intermixing due to the interdiffusion of Al and Ga atoms during annealing. The lateral corrugation modulation is caused by a lateral composition modulation due to diffusion and clustering of indium atoms. It is known that in various material systems it is possible to have a phase separation into indium rich and indium poor phases [46, 47, 48]. The bright areas are attributed to indium rich areas. Note that the filled states image actually shows the As sites. The indium rich areas appear bright because the In atoms in the first subsurface layer cause the surface As atoms to protrude out of the surface plane [49]. With the model described in [26], we find that a deviation of -7.5% and $+7.5\%$ from the nominal indium concentration in the indium poor and rich areas, respectively, accounts for the observed corrugation modulation. We propose that the strong lateral corrugation modulation together with roughening of the barrier/well interfaces as an alternative mechanism for the strong degradation in PL intensity observed in these samples by Song *et al.* [45].

Figure 6.3(c) is a large scale overview image of the 800°C annealed sample, showing the lateral corrugation modulation on the InAlAs cladding layers (dark) and the (InGaAs)_{0.4}(InAlAs)_{0.6} separate confinement heterostructure (SCH) layers with the three quantum well layers. Note that we do not observe the lateral

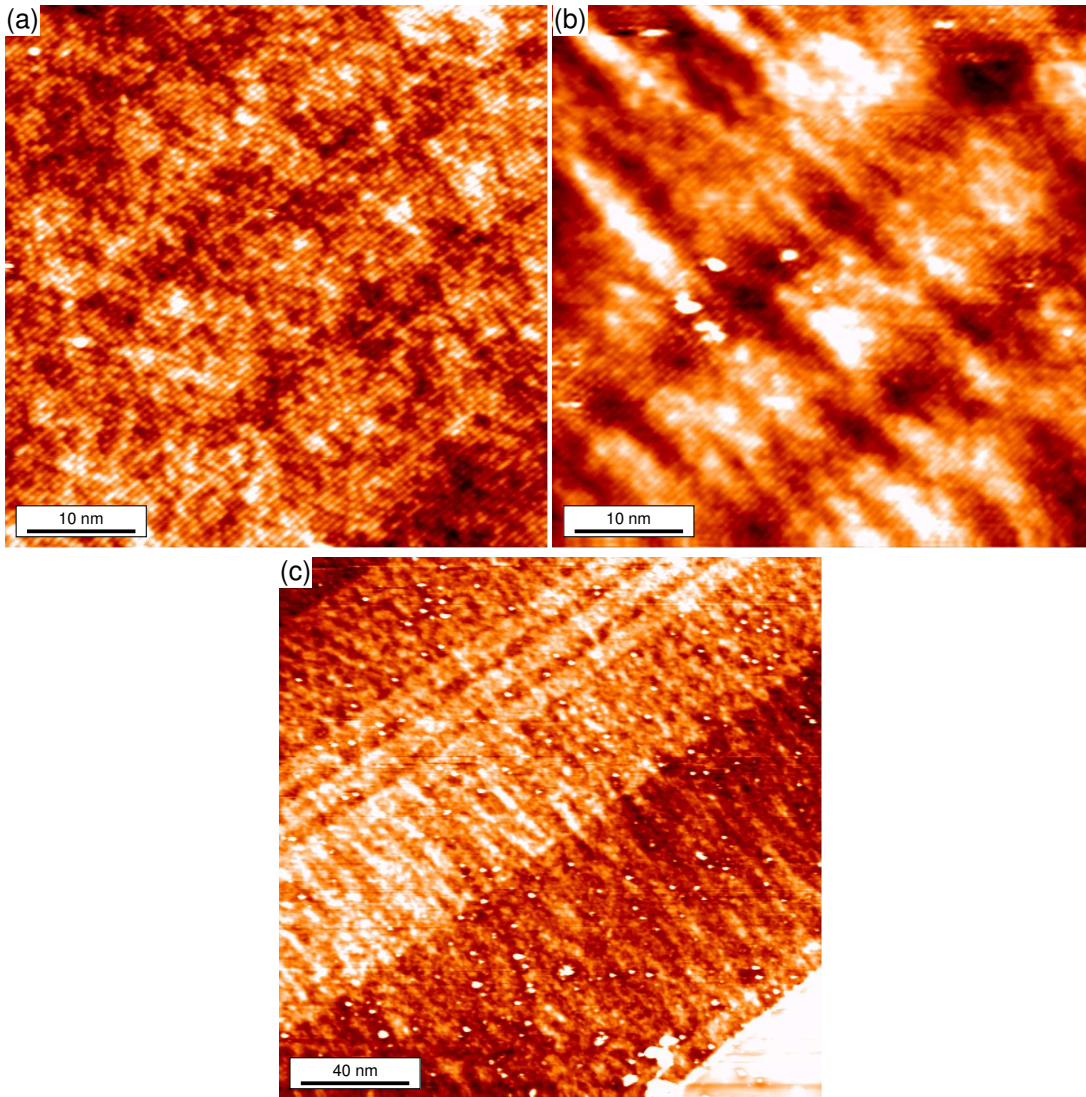


Figure 6.3: (a) and (b) $50 \times 50 \text{ nm}^2$ filled states topography image of the as-grown sample (a) and annealed ($T_{\text{RTA}} = 800^\circ\text{C}$) sample (b) showing three wells and two barriers. Contrast between wells and barriers is very low because of high sample voltage which minimizes electronic contrast. The height scales are 0 pm (black) to 180 pm (white), $V_{\text{sample}} = -3.0 \text{ V}$. (c) $200 \times 200 \text{ nm}^2$ filled states topography image of the $T_{\text{RTA}} = 800^\circ\text{C}$ annealed sample showing large scale lateral corrugation modulation. The dark regions are the 50 nm cladding InAlAs layers. Also part of the InP substrate is visible in the lower right corner, $V_{\text{sample}} = -3.0 \text{ V}$.

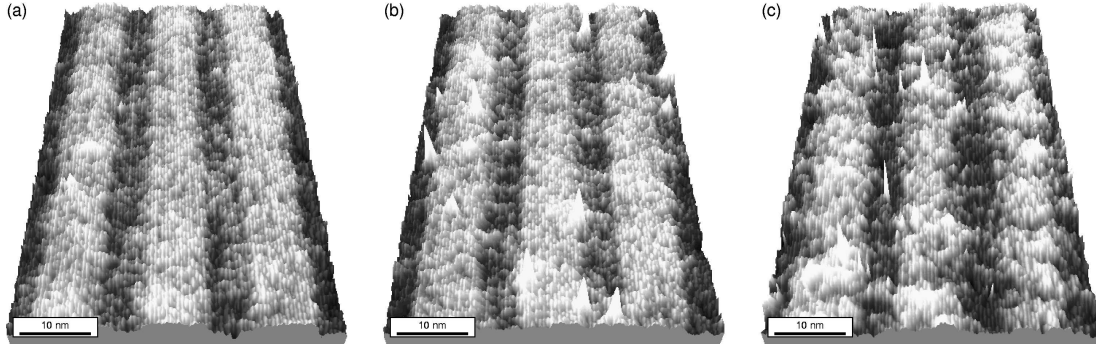


Figure 6.4: $72 \times 48 \text{ nm}^2$ filled states topography images of (a) as-grown sample, $V_{\text{sample}} = -1.4 \text{ V}$. (b) 750°C annealed, $V_{\text{sample}} = -1.4 \text{ V}$ and (c) 800°C annealed sample, $V_{\text{sample}} = -2.2 \text{ V}$.

corrugation modulation across the entire image; parts of the MQW region are relatively undisturbed. We have no explanation for this.

To compare the effects of annealing more directly, we show filled state images of the as-grown, the 750°C and the 800°C sample in Fig. 6.4. The 750°C and as-grown images look roughly the same, the 800°C image, however, clearly shows large barrier/well intermixing and phase separation. The short period superlattice shows only slight intermixing after annealing at 750°C which agrees with the observed small PL blueshift. The huge increase of PL intensity after annealing at 750°C is usually attributed to the curing of non-radiative recombination centers that are introduced unintentionally by the low temperature growth of the InAlAs layers. As mentioned earlier we could not find any evidence for this. Annealing at 750°C did not affect the barrier/well interfaces which agrees with the improved PL characteristics, whereas the strong degradation of the PL intensity after annealing at 800°C is due to barrier/well intermixing and phase separation.

6.4 Conclusion

In conclusion we have shown that it is possible to resolve the digital alloy period for an as-grown digital alloy (In,Ga,Al)As MQW structure by X-STM. Our results show that in the presence of a 1500 \AA SiO_2 capping layer, annealing at 750°C results in slight intermixing of the SPS whereas annealing at 800°C results in complete disappearance of the digital alloy period. Annealing at 750°C does not affect barrier/well interface roughness. Annealing at 800°C results in large barrier/well interface roughness and lateral composition modulation due to indium phase separation. These conclusions support the assertions in Ref. [45].

This work was done in collaboration with J.D. Song, J.M. Kim, S.J. Bae and Y.T. Lee, Kwangju Institute of Science and Technology, Korea.

7

Digital alloy interface grading of an InGaAs/InAlAs quantum cascade laser structure

We have studied an InGaAs/InAlAs quantum cascade laser structure with cross-sectional scanning tunneling microscopy. In the quantum cascade laser structure digital alloy grading was used to soften the barriers of the active region. We show that due to alloy fluctuations, softening of the barriers occurs even without the digital grading.

7.1 Introduction

Unlike quantum well semiconductor lasers, where the light originates from recombination of electrons and holes across the energy gap that exists between the conduction band and valence band of the crystal, in quantum cascade laser (QCL) structures, the emission wavelength is given by the subband energy spacing. In the case of lattice-matched growth on InP using InAlAs/InGaAs layers, this can be effectively controlled by the thicknesses of the layers of the active region. The injection and extraction efficiency to and from the active regions has been significantly improved by means of wave function engineering, which involves control over the barrier/well thickness and interface quality. Interface roughness scattering is one of the important non-radiative scattering mechanisms of QCL structures. To reduce interface roughness scattering, digital alloy grading was used to soften the barriers of the active region of a four-quantum-well (4QW)

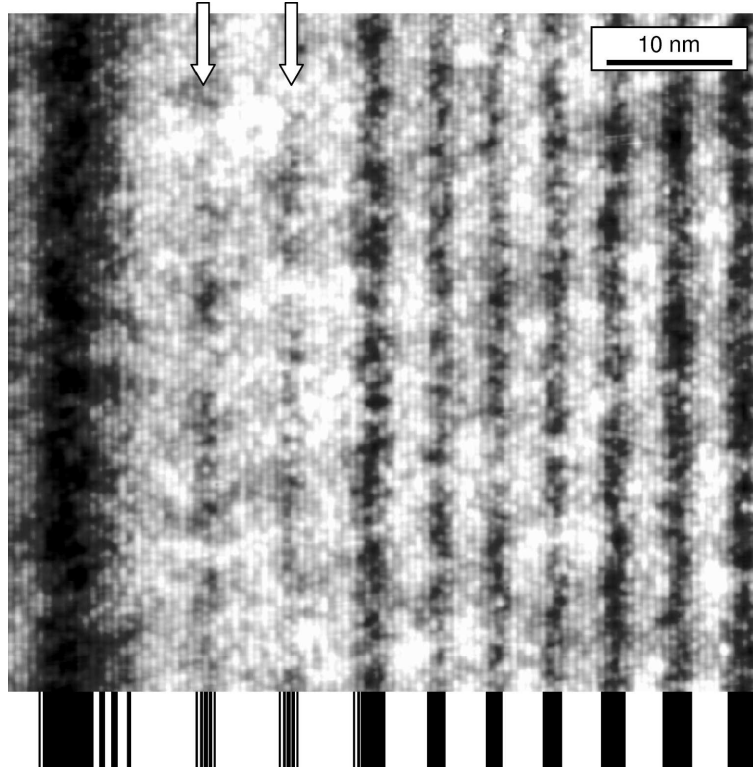


Figure 7.1: $60 \times 60 \text{ nm}^2$ filled states STM image of the graded structure with layer sequence indicated at the bottom of the image, $V_{\text{sample}} = -1.6 \text{ V}$. The dark layers are the InAlAs barriers and the bright layers are the InGaAs wells. The arrows indicate the graded barriers that separate the wells of the active region.

mid-infrared quantum cascade laser structure. This structure showed a reduced threshold current density and a narrower luminescence linewidth in pulsed mode than a device with abrupt interfaces [50]. However, this result could not be reproduced in a second growth run, and might therefore also be attributed to the device processing, rather than to the active structure itself. We report cross-sectional scanning-tunneling microscopy (X-STM) measurements of 4QW QCL structures with and without graded interfaces. The aim of this chapter is to show that interface roughness and grading occur due to fluctuations in the alloy concentration that are caused by indium clustering during growth.

7.2 Sample description

The QCL structures were grown by molecular-beam epitaxy on InP substrates using lattice-matched InAlAs/InGaAs active layers and an InP top cladding. Ex-

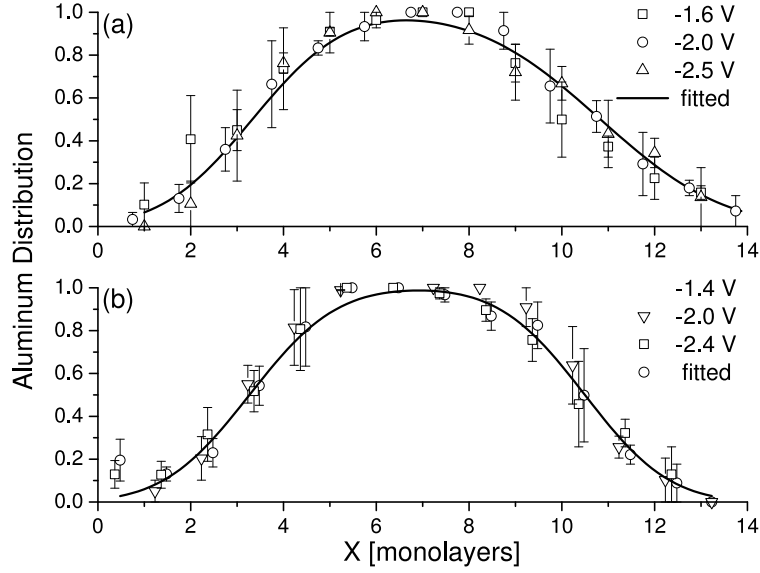


Figure 7.2: Aluminum concentration of an abrupt 2.5 nm barrier of both the structure with graded interfaces (a) and abrupt interfaces (b) in the active region. The aluminum concentration was derived from averaged line profiles taken at three sample voltages.

cept for the interfaces, both types of devices are identical and based on a 4QW active region designed for a vertical lasing transition at 9.3 μm with a double phonon resonance [51]. The layer sequence of the graded structure is as follows, with InGaAs wells in roman, InAlAs barriers in bold, and doped layers ($\text{Si}, 3 \times 10^{17} \text{ cm}^{-3}$) underlined:

31/19/30/23/29/25/26/1/2/40/5/4/6/4/8/(3/52/1/2)/(2/1/3/1/2)/(2/1/51/1/2)/(2/1/3/1/2)/(2/1/44/1/2)/(2/1/19)/34/14/33/13/32/15 Å. The structure with the abrupt interfaces has the following layer sequence:

31/19/30/23/29/25/29/40/19/7/58/9/57/9/50/22/34/14/33/13/32/15 Å.

The main differences between both structures are the design of injection barrier and the barrier/well interfaces of the active region which are graded by a digital InGaAs/InAlAs alloy of 1 Å and 2 Å thick layers as indicated by parentheses. The samples were grown by M. Beck, University of Neuchâtel, Switzerland.

7.3 Results

In Fig. 7.1 we show a STM image of the QCL structure with graded interfaces. Figure 7.1 was taken at a negative sample bias of -1.6 V , showing the filled states associated with the As sublattice. The bright regions are the InGaAs well layers and the dark regions are the InAlAs barrier layers. The observed contrast

between the barrier and the well layers is due to the band offset between the well and the barrier layers which causes an electronic contribution to the tunneling current at low sample bias ($V_{\text{sample}} > -2 \text{ V}$). The graded interfaces are indicated by arrows. The brighter and darker regions within and across the layers indicate the strong presence of alloy fluctuations. We will show that these are caused by indium clustering. It is clear that the alloy fluctuations are producing strong interface roughness, which influences the actual effect of the intentional grading of the interfaces.

In order to quantify the sharpness of the ungraded interfaces of both structures, we derive the distribution of the gallium and aluminum atoms across both interfaces of a 2.5 nm wide barrier by using averaged line profiles of the filled states image. Since we are imaging the filled states of the sample surface, we are not directly probing the aluminum and gallium atoms themselves, but rather the electronic effects these two atomic species have on the surface arsenic atoms. The apparent height of an arsenic site is dependent on the number of aluminium atoms in the nearest neighbor positions at the cleaved (110) surface [52]. There are three nearest neighbor positions where an Al atom can reside. Two neighbor positions are in the surface layer and one neighbor position is in the subsurface layer. In our analysis of the apparent height profile, the average number of aluminum atoms of a single bilayer can be assigned to both the surface and subsurface layers, which will give a spread in the possible number of aluminum atoms in each monolayer. The final aluminum distribution is determined by fitting with a concentration profile in the form of: $c(x) = 1/2(\text{erf}((L/2+x)/2\sigma_x) + \text{erf}((L/2-x)/2\sigma_y))$, where L is the width of the barrier and σ_x and σ_y are related to the sharpness of the interfaces of the barrier. Figures 7.2(a) and 7.2(b) show for both QCL structures the aluminum distribution of the 2.5 nm wide abrupt InAlAs barrier. The analysis was done for profiles taken at sample voltages of -1.6 V , -2.0 V and -2.4 V . Although the observed contrast in the STM image depends on the applied voltage, the counted aluminum distribution does not. We find that for both structures the FWHM is in agreement with the growth menu, however, in both cases the interfaces have a width of 4 ML. We propose that this grading is caused by large scale alloy fluctuations due to indium clustering during growth. This means that any additional digital grading of the interfaces of the active region will not have a strong effect.

In Fig. 7.3(a) and 7.3(b) we show detailed images of the active region of the graded structure and the structure with abrupt interfaces. The barriers of the active region are indicated by arrows. The injection barriers of both structures are clearly different; however, the thin barriers in the active region look the same. This can also be seen in Fig. 7.3(c), which shows the averaged line profiles of the active region of both structures.

Fig. 7.4 shows the InGaAs region which was grown on top of the active layers. In the lower right corner part of the active layers can be seen. The image was taken at high positive voltage ($+2.5 \text{ V}$) where electronic contrast is minimized

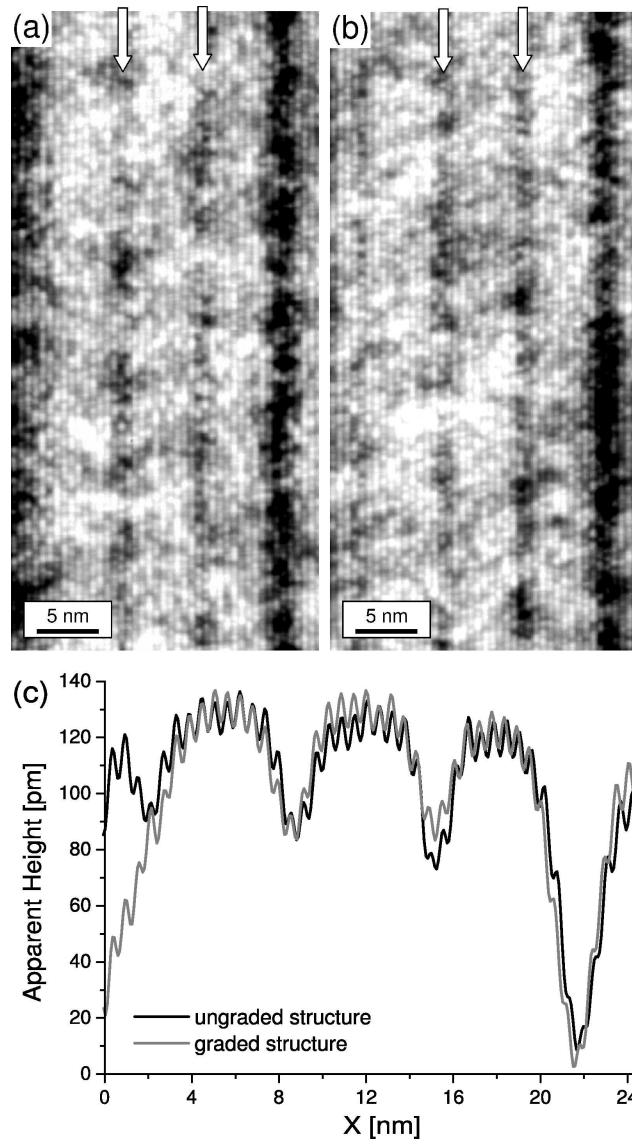


Figure 7.3: $25 \times 55 \text{ nm}^2$ filled states STM image of the active region of (a) the structure with digitally graded interfaces and (b) the structure with abrupt interfaces. (c) shows the averaged line profiles of the active region.

[23, 24]. The topographical contrast is due to the outward relaxation of indium rich regions. The lateral scale variation of alloy fluctuations is about 10 nm, which is large enough to influence the device characteristics [53].

Fig. 7.5(a) and 7.5(b) show images of the same active region at low negative voltage (filled states) and high positive voltage (empty states) respectively. The filled states image clearly shows the electronic contrast between the barriers and wells. The empty states image shows the topographical contrast due to outward

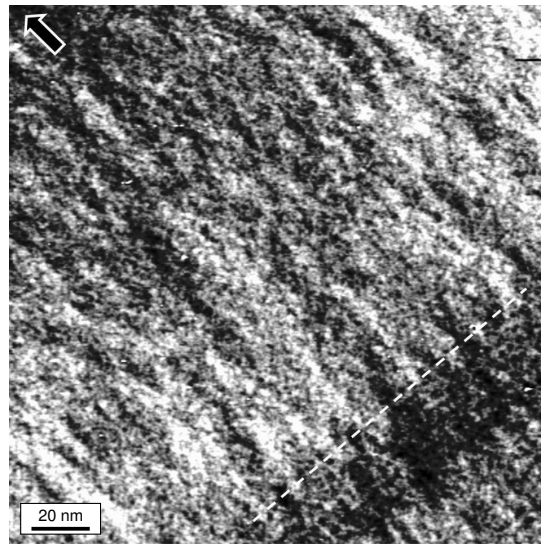


Figure 7.4: $185 \times 185 \text{ nm}^2$ empty states image of the InGaAs capping layer of the structure with digitally graded interfaces showing the outward relaxation of indium rich regions, $V_{\text{sample}} = 2.5 \text{ V}$. In the bottom right corner, indicated by the dashed line, part of the active layers can be seen. The growth direction is indicated by the arrow.

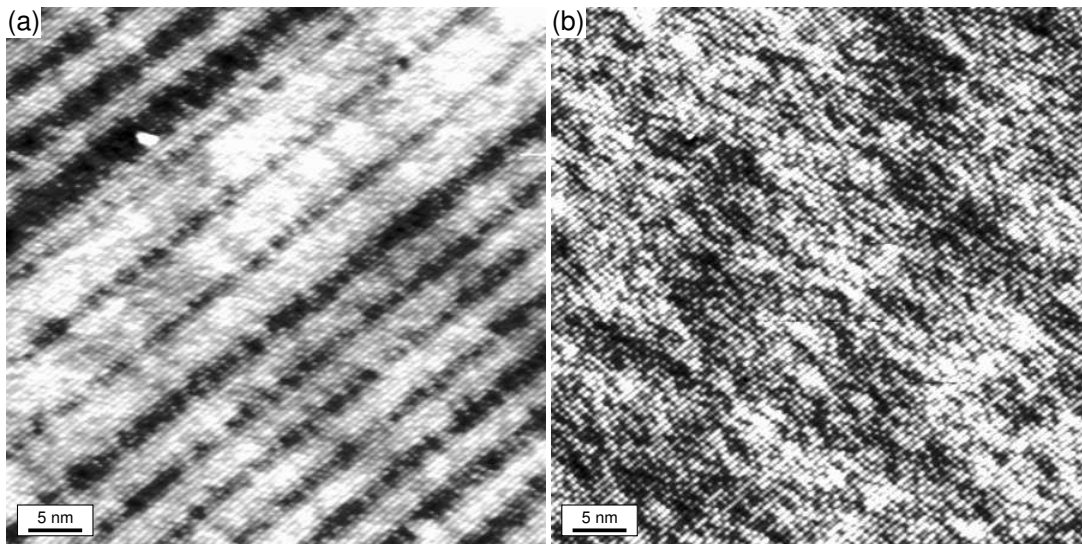


Figure 7.5: $50 \times 50 \text{ nm}^2$ filled states, $V_{\text{sample}} = -1.6 \text{ V}$ (a) and empty states, $V_{\text{sample}} = 2.4 \text{ V}$ (b) image of the injector region of the structure with abrupt interfaces. In both images brighter and darker regions correspond to indium rich and indium poor regions.

relaxation of indium rich regions. In this image the wells and barriers cannot be distinguished due to the lack of electronic contrast. In both the barriers and the wells of the filled states image brighter and darker regions can be seen, which correspond to the indium rich and indium poor regions of the empty states image. This shows to our surprise that the indium clusters extend across the barrier and wells, resulting, on average, in graded interfaces.

7.4 Conclusion

We have compared QCL structures with and without digitally alloyed interfaces on the atomic level with X-STM. We showed that fluctuations in the width of the layers occur due to indium clustering across the barrier and well layers, which on average lead to graded interfaces of about 4 ML. We find that, because of the unintentional grading, the digital alloy graded interfaces are not significantly smoother than the ungraded interfaces. We propose that in order to reduce interface roughness scattering, fluctuations in the layer thicknesses due to indium clustering should be taken into account in the design and growth of QCL structures.

This work was done in collaboration with M. Beck, T. Aellen and J. Faist, University of Neuchâtel, Switzerland.

8

Formation of InAs wetting layers

We show that the composition of (segregated) InAs wetting layers (WLs) can be determined by either direct counting of the indium atoms or by analysis of the outward displacement of the cleaved surface as measured by cross-sectional scanning tunneling microscopy. We use this approach to study the effects of the deposited amount of indium, the InAs growth rate, and the host material on the formation of the WLs. We conclude that the formation of (segregated) WLs is a delicate interplay between surface migration, strain-driven segregation and the dissolution of quantum dots during overgrowth.

8.1 Introduction

The formation of InAs wetting layers (WLs) has attracted relatively little attention compared to quantum dot (QD) formation [54, 55, 56]. In the simple picture of Stranski-Krastanov growth, after the build-up of a critical amount of strain, 2D layer growth is followed by QD formation. It has become increasingly clear, however, that such a simple picture is far from reality. Recently, In incorporation during pseudomorphic InAs/GaAs growth and QD formation were observed by in-situ stress measurements [57].

In this paper we study the segregation of InAs WLs by either directly counting the indium atoms or by analysis of the outward displacement of the cleaved surface as measured by cross-sectional scanning tunneling microscopy (X-STM).

By cleaving the sample containing the WLs, the cross-sectional surface of the segregated InAs WLs is exposed, and releases its strain due to the lattice mismatch between the InAs and the surrounding GaAs (or AlAs) matrix, which

results in an outward displacement of the cleaved surface [26]. This can be measured with X-STM at high negative sample voltages (< -2 V), where the electronic contribution to the contrast in the image is minimized [23]. By modeling the indium segregation, the outward displacement of the segregated WL can be calculated by integration of the analytical expression derived by Davies for the outward displacement of a cleaved quantum well [26]. Several models for indium segregation have been proposed [58, 59, 60, 61]. We use the phenomenological model of Muraki *et al.* [59], which has been shown to describe the indium composition $x(n)$ of InAs WLs well [56]:

$$x(n) = \begin{cases} 0, & n < 1 \\ (1 - R^n), & 1 \leq n \leq N \\ (1 - R^N)R^{n-N}, & n > N \end{cases}, \quad (8.1)$$

where n is the monolayer (ML) index, N is the total amount of deposited indium and R is the indium segregation coefficient. N and R are determined by fitting the calculated relaxation profile to the measured relaxation profile.

8.2 Sample description

The WLs were grown by molecular-beam epitaxy (MBE) on doped GaAs (100) wafers. In sample A, three different sets of WLs were grown at 495°C by deposition of 1.5 ML, 2.0 ML and 2.5 ML of InAs, respectively, at a growth rate of 0.1 ML/s. Each layer was repeated two times, separated by a 50 nm GaAs buffer layer, also grown at 495°C. A growth interruption of 10 seconds has been applied after the growth of each layer. No dot formation was observed for the layers with 1.5 ML indium deposition. In sample B, two sets of WLs were grown at 480°C by deposition of 2.0 ML of InAs at a high and a low growth rate of 0.1 ML/s and 0.01 ML/s, respectively. Each layer was repeated two times and capped by a 20 nm GaAs layer grown at 480°C, followed by a 30 nm GaAs layer grown at 580°C. A growth interruption of 10 seconds has been applied after the growth of each layer. In sample C, one set of InAs layers was grown in GaAs while a second set was grown in AlAs barriers. The InAs layers were grown at 500°C by deposition of 1.9 ML of InAs in a cycled way, i.e., with a 3 seconds pause after each deposition of 0.25 ML, at a growth rate of 0.043 ML/s. The following layer sequence was used: 20 nm GaAs/1.9 ML InAs/40 nm GaAs/1.9 ML InAs/40 nm GaAs/50 nm GaAs (doped $1 \times 10^{18} \text{ cm}^{-2}$)/20 nm GaAs/4×(20 nm AlAs/1.9 ML InAs/20 nm AlAs/40 nm GaAs). To reduce interface roughness, the bottom AlAs barriers were grown at 600°C followed by a growth interruption prior to InAs deposition. Samples A and B were grown by G. J. Hamhuis. Sample C was grown by K. Pierz, Physikalisch-Technische Bundesanstalt Braunschweig, Germany.

8.3 Results

Sample A was used to study the effect of the amount of indium deposition on the WL formation. We measured the relaxation profiles of the WLs and fitted these with calculated relaxation profiles, by adjusting the fit parameters N and R . The resulting segregation profiles were verified by counting directly the number of indium atoms in the WL as a function of distance in growth direction. For the counting procedure, we selected four high quality images of each layer, such as the one shown in Fig. 8.1. The relaxation and segregation profiles are shown in Fig. 8.2. In all three cases, we find an excellent agreement between the indium profile determined from the outward relaxation of the surface, and the direct counting procedure. For the 1.5 ML WL, the measured amount of indium N corresponds to the deposited amount, indicating that no indium has gone into dot formation. For the 2.0 ML and 2.5 ML WLs, however, we find a clear indium enrichment of the WL, despite dot formation.

In Stranski-Krastanov growth mode, strain builds up until the critical amount of indium for dot formation is deposited [62]. It has been shown that only part of the deposited amount of indium contributes to the strain, by incorporation into the lattice, while the remaining indium forms a floating layer on the surface [57]. During dot formation, part of the floating indium is transferred by lateral mass

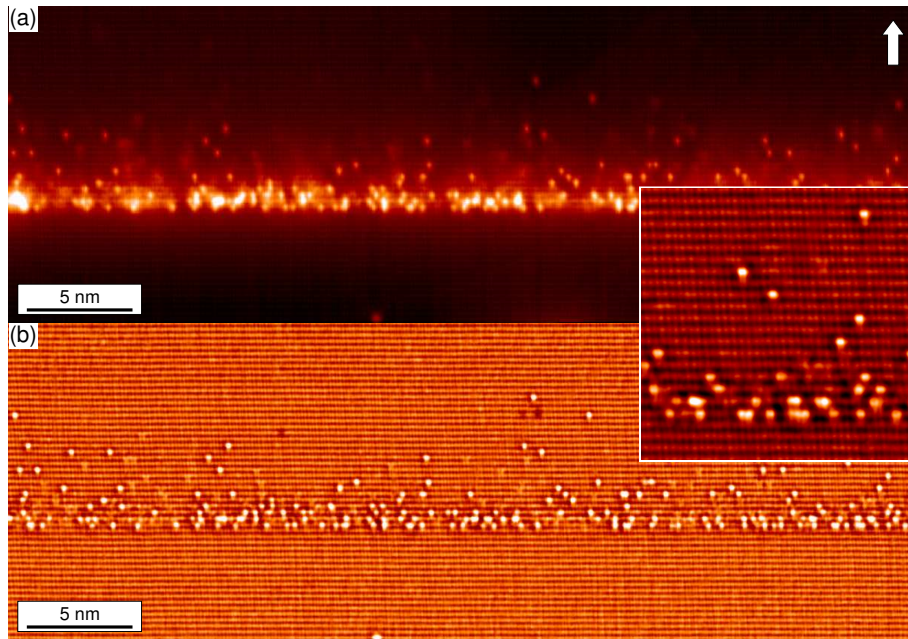


Figure 8.1: (a) Empty states X-STM image of a segregated 2.0 ML InAs WL. (b) The same image treated with a high-pass Fourier filter. The inset shows an enlarged view of part of the image.

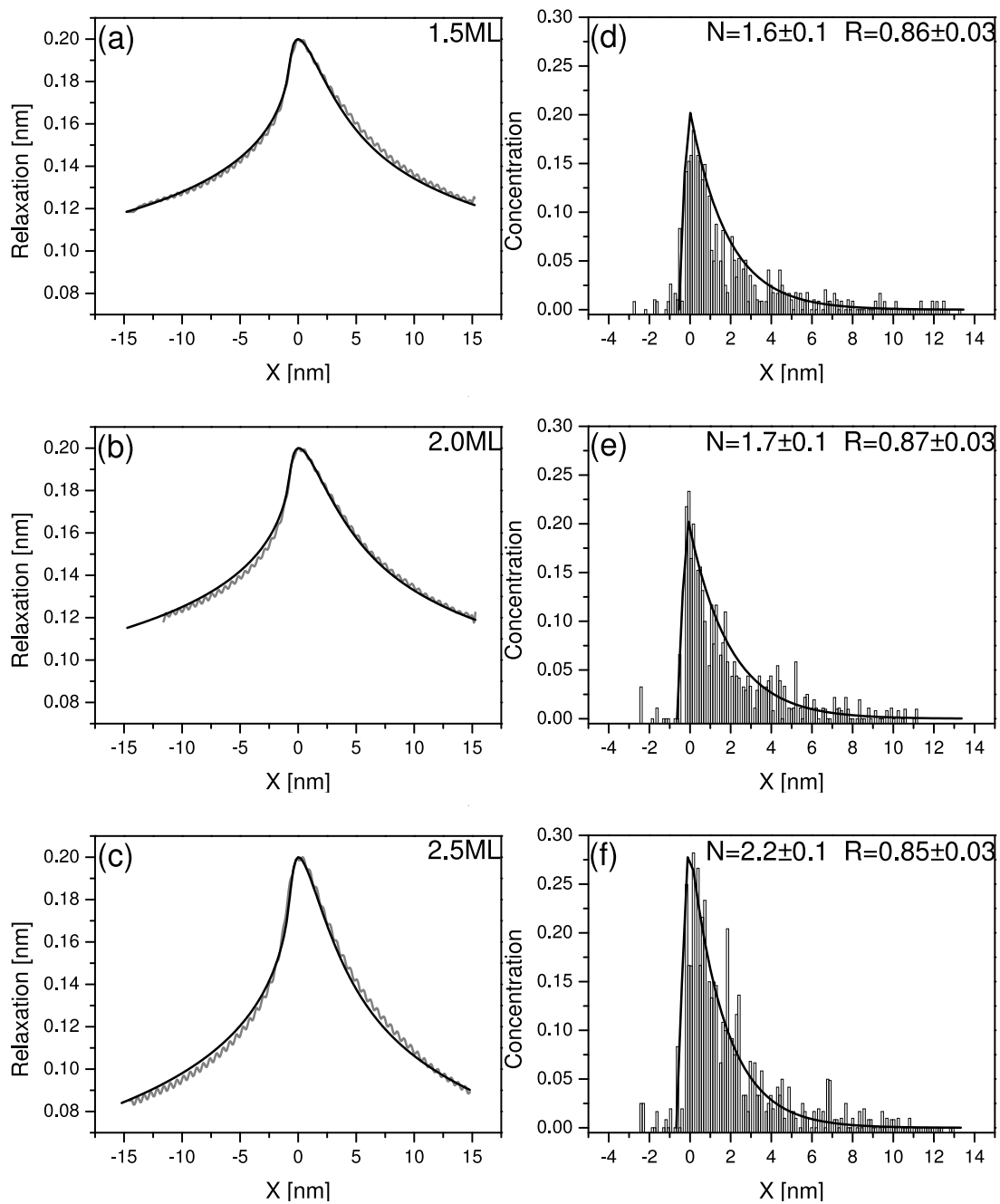


Figure 8.2: Measured and fitted relaxation profiles of the 1.5 ML (a), 2.0 ML (b) and 2.5 ML (c) InAs WLS of sample A. The black curves in (d), (e) and (f) show the segregation profiles corresponding to the fitted relaxation profiles in (a), (b) and (c). The columns indicate the counted indium concentration in the WL as a function of distance X in growth direction.

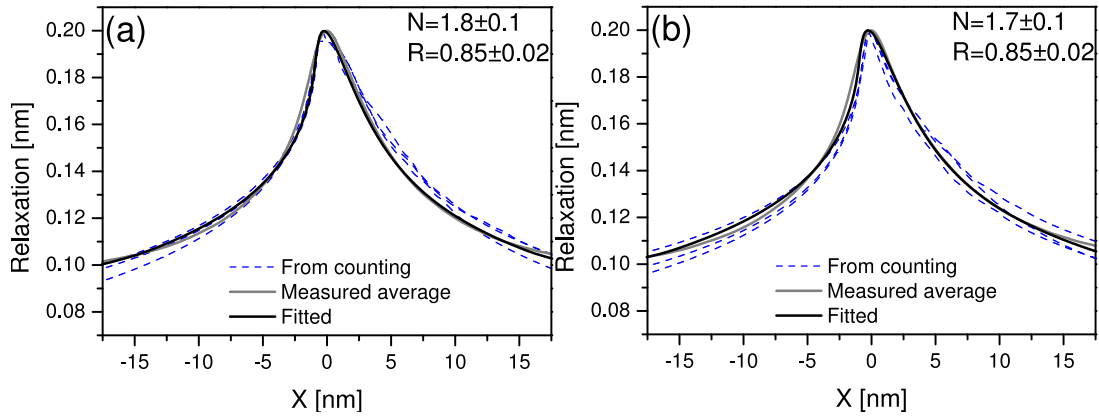


Figure 8.3: Measured and fitted relaxation profiles of the high (a) and low (b) growth rate InAs WLs of sample B. The dashed lines indicate the relaxation profiles calculated directly from counted segregation profiles.

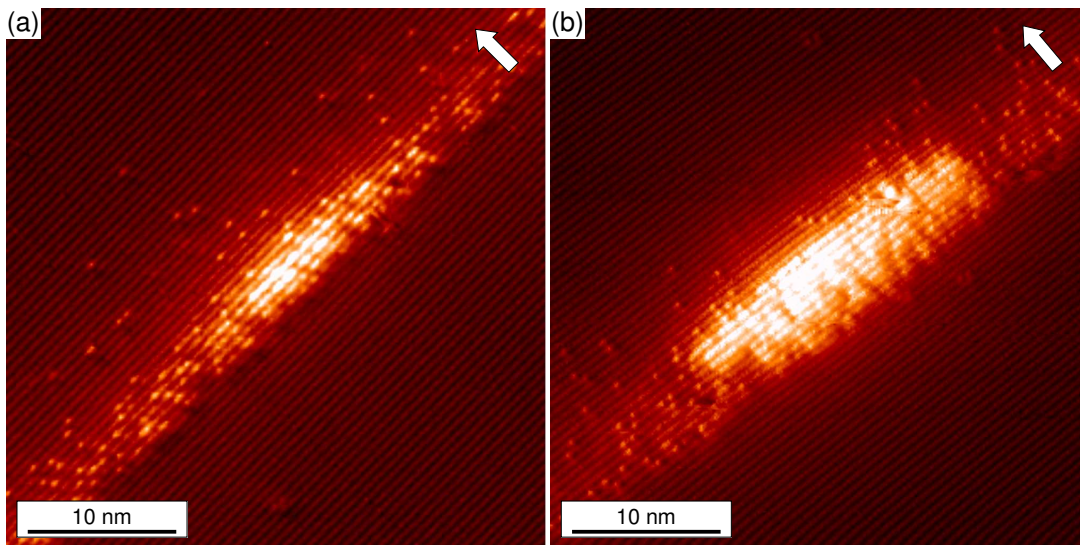


Figure 8.4: X-STM images of typical quantum dots found in the high (a) and low growth rate WLs (b). The arrow indicates the growth direction.

transport to the dots. The amount of indium that remains in the dots, however, is strongly reduced by the capping process, which dissolves the top of the dots back into the WL [63]. The dissolved indium adds to the remaining floating indium, and is eventually incorporated into the lattice, during continued capping.

We used sample B to study the effect of a reduced growth rate on the WL formation. It is known that a reduced growth rate leads to an increased QD size and a reduced QD density. However, it is not a priori clear how this affects the formation of the segregated WL in the buried structure. In Fig. 8.3 we show the

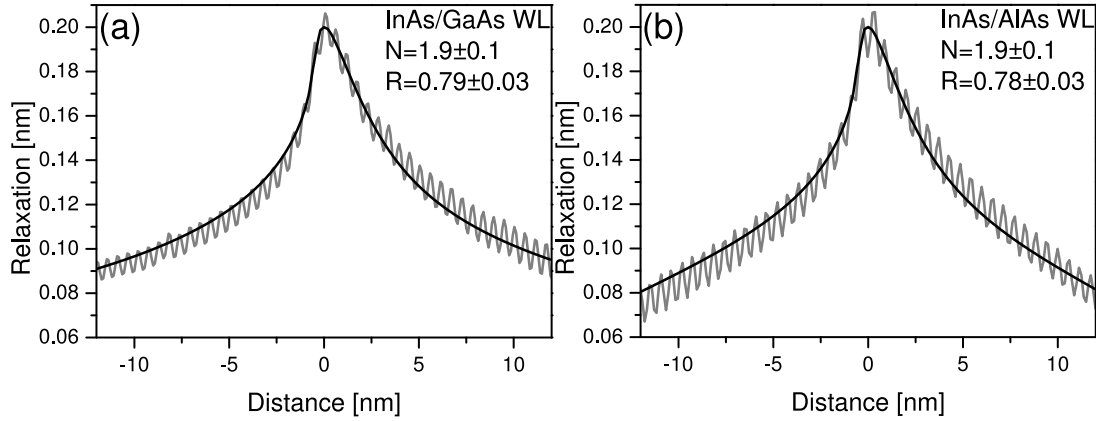


Figure 8.5: Measured and fitted relaxation profiles of the segregated InAs WLS in GaAs (a) and AlAs (b).

average measured and calculated relaxation profiles of the InAs WLS of sample B. The dashed lines indicate the relaxation profiles calculated directly from indium atom counting for different images. We find that the high (0.1 ML/s) and low (0.01 ML/s) growth rate InAs WLS can be described by the same parameters within errors. However, as expected, there is a marked difference in the size of the QDs, shown in Fig. 8.4(a) and 8.4(b). Whereas the QD grown at the high growth rate appears as a rather flat, disc-like shape with a height of 3 nm, the QDs grown at low rate, show an indium distribution with a reversed truncated cone shape [64] with a height of 5.4 nm.

We studied the effect of the host material, by analyzing the segregation of InAs WLS grown in the AlAs barriers of sample C, and comparing this to the segregation of InAs WLS grown, under the same growth conditions, in a GaAs matrix. It has been shown that QD formation in the InAs/AlAs system is kinetically limited due to a reduced lateral In migration on the AlAs surface, because of the larger Al-In bond strength [65]. Recently, we have reported on the marked differences in the structural properties of the dots grown in GaAs and AlAs [66]. Fig. 8.5. shows the averaged measured and fitted relaxation profiles. We find that the vertical indium segregation in AlAs and GaAs can be described by almost the same parameters, in agreement with [55]. This indicates that, in contrast to the lateral In migration, the vertical indium segregation is strain-driven rather than determined by the chemical bond strength.

It is known that vertical indium segregation is reduced at lower growth temperatures [67]. We have reported that reducing the growth temperature to 300°C after capping of the WLS with 3 monolayers of GaAs leads to a dramatic reduction of the indium segregation [63]. However, such a capping procedure also leads to the almost complete dissolution of the QDs into the capping layer due to their partial coverage.

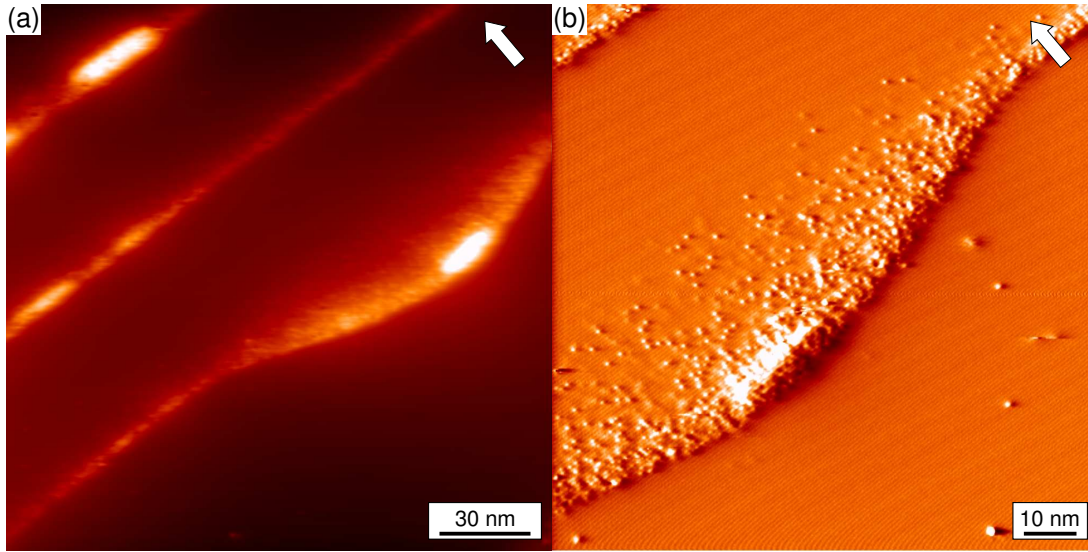


Figure 8.6: (a) X-STM overview image showing a shallow V-groove in one of the layers of sample B. (b) X-STM current-image showing an enlarged view of the V-groove. The arrow indicates the growth direction.

Another drastic example of the effects of partial capping is the formation of quantum rings (QRs). QRs can be grown by the partial capping of QDs with 2 nm of GaAs and subsequent annealing [68]. Recently, we observed that during this process, a second layer of indium accumulates on the surface of the capping layer, which is due to vertical segregation of indium from the WL and to lateral migration on the surface of indium atoms that have been expelled from the QDs during QR formation [69, 70, 71, 72]. After continued capping, the second layer of indium, forms a segregated indium distribution.

Finally, we show in Fig. 8.6 an overview image of the WLs of sample B. Surprisingly, one of the layers, showed a shallow V-groove in which a QD was formed. The V-groove was unintentionally created on the GaAs substrate. It can clearly be seen that a large amount of indium atoms have accumulated in the V-groove. By comparing the extent of the indium segregation inside and outside the V-groove, it can be seen that during GaAs overgrowth, the indium segregation and migration facilitates a rapid planarization of the growth front, in the presence of indium atom accumulation in the V-groove.

8.4 Conclusion

We have shown that the composition of (segregated) InAs WLs can be determined by either directly counting the indium atoms or by analysis of the outward displacement of the cleaved surface as measured by X-STM. We used this approach

to study the effects of the deposited amount of indium, the InAs growth rate, and the host material on the formation of the WLs. A clear indium enrichment of the WL is found after the deposition of the critical amount of indium, despite dot formation. We attribute this to the dissolution of the top of the dots back into the WL during the capping process. Although we find a marked difference in the size of the QDs at high (0.1 ML/s) and low (0.01 ML/s) growth rate, in these cases the segregated InAs WLs can be described by the same parameters within errors. By comparison of the vertical indium segregation in AlAs and GaAs we find that, in contrast to the lateral In migration, the vertical indium segregation is strain-driven rather than determined by the chemical bond strength. We conclude that the formation of (segregated) WLs is a delicate interplay between surface migration, strain-driven segregation and the dissolution of quantum dots during overgrowth.

9

Atomic-scale structure and photoluminescence of InAs quantum dots in GaAs and AlAs

We have determined the size, shape and composition of InAs/GaAs QDs and InAs QDs embedded in an AlAs barrier, by cross-sectional scanning tunneling microscopy. The outward relaxation and lattice constant of the cleaved surface of the QDs and their wetting layers were calculated using continuum elasticity theory and compared with experimental data in order to determine the indium concentration of the dots. Based on the structural results we have calculated the electronic ground states of the dots using a single band, effective mass approach. We find that the calculated ground state photoluminescence energy of the InAs/GaAs dots is in excellent agreement with the measured energy. The observed large width of the PL spectrum of InAs/AlAs dots can be attributed to Γ - Γ electron-hole recombination within an ensemble of dots with sizes varying between 2.4–4.2 nm in height and 10–20 nm along the base diagonal. We find that the electron-hole wave function overlap of small InAs/AlAs QDs is 7.6 times larger than that of InAs/GaAs QDs grown under the same conditions. This supports the explanation that the long decay times in InAs/AlAs dots are caused by an enhanced exciton exchange splitting.

9.1 Introduction

Self-assembled InAs quantum dots (QDs) embedded in AlAs barriers are of interest because of their large confinement potential [73, 74] compared to InAs/GaAs QDs and their consequent suitability for resonant tunneling devices [75, 76]. Despite the almost identical lattice mismatch, the formation of InAs QDs in AlAs differs considerably from that in GaAs. This is due to the larger Al-In bond strength, which reduces In migration on the AlAs surface, leading to a larger density and smaller size of InAs/AlAs QDs [65]. It is these differences in size distribution, together with the larger confinement potential, that are thought to cause the large differences in the observed photoluminescence (PL) spectra between the two types of QD [77, 75, 65]. However, the relationship between the differences in the spectra, and the properties of the two dot types is not quantitatively understood because of a lack of detailed structural information on buried InAs/AlAs QDs [78]. Experimental and theoretical investigation of this topic is the subject of the present work.

We determine the shape, size and composition of the QDs by cross-sectional scanning tunneling microscopy (X-STM). We show new results for the composition variation in an InAs/AlAs dot and confirm the inverted trumpet-like indium distribution that has been assumed in InAs/GaAs QDs [79, 54, 80, 64]. Based on the X-STM results we then use a single band effective mass approach to calculate the electron and hole states and estimate the ground state PL energy. Our results are consistent with the measured PL spectra and indicate that the large difference in the PL spectra of InAs/GaAs and InAs/AlAs QDs can be explained by the structural properties of the dots. Finally, we discuss the mechanisms that have been suggested for the recently observed extremely long (microsecond) PL decay times of the InAs/AlAs dots [81, 82, 83].

9.2 Sample description and experimental setup

The QDs were grown by molecular-beam epitaxy on doped GaAs (100) wafers. During growth of the QDs the substrate temperature was maintained at 500°C. Each 1.9 ± 0.1 monolayer (ML) of InAs was grown in a cycled way, i.e., with a 3 second pause after each deposition of 0.25 ML, at a low growth rate of 0.043 ML/s. After a 500 nm n-doped ($1 \times 10^{18} \text{ cm}^{-2}$) GaAs buffer layer the following sequence was grown: 20 nm GaAs/1.9 ML InAs/40 nm GaAs/1.9 ML InAs/40 nm GaAs/50 nm n-doped GaAs/20 nm GaAs/4×(20 nm AlAs/1.9 ML InAs/20 nm AlAs/40 nm GaAs). The bottom AlAs barriers were grown at 600°C followed by a growth interruption prior to InAs deposition. This growth temperature avoids excessive surface roughness. The sample was grown by K. Pierz, Physikalisch-Technische Bundesanstalt Braunschweig, Germany.

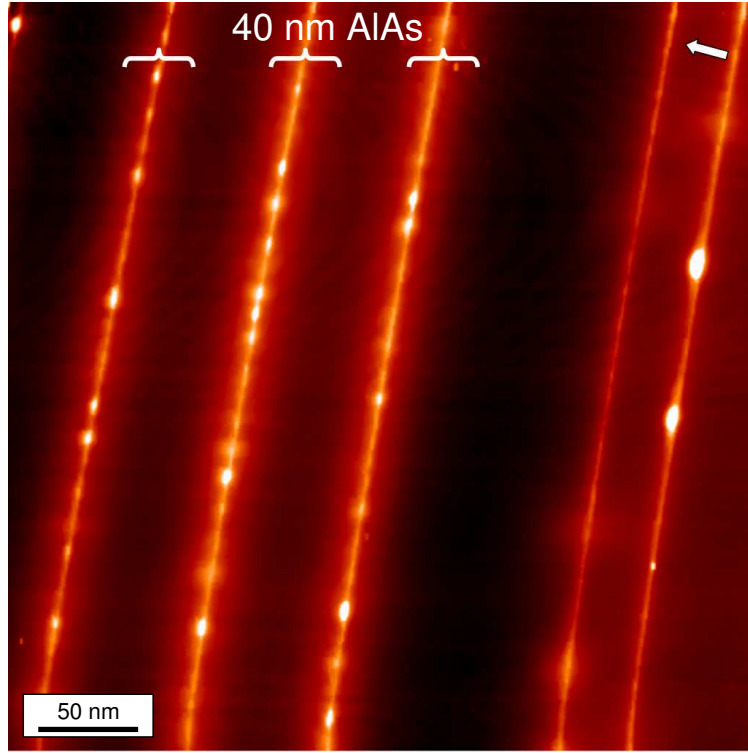


Figure 9.1: Filled states topography X-STM image of three QD layers embedded in 40 nm thick AlAs barriers and two QD layers grown in GaAs, $V_{\text{sample}} = -3$ V. The arrow indicates the growth direction.

The X-STM measurements have been performed in an ultra-high-vacuum (UHV) chamber with base pressure $< 2 \times 10^{-11}$ Torr on the UHV-cleaved (110) cross-sectional surface. The photoluminescence measurements were performed in an He cryostat at 7 K under cw-excitation ($\lambda = 514$ nm) from an Ar^+ laser.

9.3 Results and Discussion

9.3.1 Structure

In Fig. 9.1 we show a large scale filled-states topography X-STM image of the structure. Three layers of QDs embedded in AlAs barriers and two layers of QDs grown on GaAs are visible in the image. Compared to the dots grown on GaAs, the QDs embedded in AlAs barriers show a smaller size and have a significantly larger density of about $3 \times 10^{11} \text{ cm}^{-2}$. This has been attributed to reduced diffusion of In adatoms on the AlAs surface due to a higher surface roughness and the larger Al-In bond strength [65].

By imaging at a high voltage ($V_{\text{sample}} = -3 \text{ V}$), electronic contributions to the contrast in the image are minimized and only the true outward surface relaxation due to the lattice mismatch (7%) between the InAs and surrounding GaAs or AlAs is imaged [23]. This is the reason why the AlAs barriers do not appear as dark layers. In X-STM the QDs are cleaved at a random position with respect to the center of the QD. Therefore, more than 20 QDs were imaged and the largest ones were selected for analysis. It can be then assumed that these QDs are cleaved near their middle.

In Fig. 9.2(a) and Fig. 9.2(b) we compare high-voltage filled-states topography images of individual InAs/GaAs and InAs/AlAs QDs, respectively. The images show the surface relaxation, which varies with the local indium distribution in the QDs. The surface relaxation of the InAs/GaAs dot indicates a lower indium concentration in the corners of the trapezium shaped cross-section compared to the center, while the indium distribution in the InAs/AlAs dot is more homogeneous.

We calculated the outward relaxation and the strain distribution of the QDs with the finite element package ABAQUS, which is based on continuum elasticity theory. The QD shape was taken to be a truncated pyramid which is consistent with the observed cross-section and earlier work [84, 28]. The sizes were determined from the X-STM measurements while the indium distribution was varied in order to get the optimal fit to the measured outward relaxation. The best results were obtained by allowing the modeled QDs to be cleaved at a plane 1 nm above their diagonal. The diagonal base length and the height of the InAs/GaAs QD is 28.4 nm and 6 nm respectively. For the InAs/AlAs QD the diagonal base length is 19 nm and the height is 4.2 nm. The calculated relaxation of the cleaved surface of the QDs is shown in Fig. 9.2(c) and Fig. 9.2(d) using the same height scale as in the corresponding X-STM images, Fig. 9.2(a) and Fig. 9.2(b).

Figure 9.3 shows the measured and calculated outward relaxation profiles (a,b) and lattice constant profiles (c,d) taken in the growth direction through the center of the QDs. From the change in lattice constant, which is determined by the strain distribution in and around the QDs, it can be seen that there is compressive strain above and below the QDs. For the InAs/GaAs QD, there is a clear increase in lattice constant towards the top of the QD, which indicates an increasing indium concentration. This can also be seen by the slight asymmetry in the relaxation profile of the InAs/GaAs QD. From X-STM and photocurrent experiments, it has been shown that low growth-rate InAs/GaAs QDs have an increasing indium concentration in the growth direction [29, 28]. However, other groups have reported (In,Ga)As QDs with laterally non-uniform indium compositions showing an inverted-triangle, trumpet or truncated reversed-cone shape [79, 54, 80, 64]. We find that the indium distribution of our low-growth rate InAs/GaAs QDs mostly resembles the trumpet shape proposed in [54] which we describe with a linear gradient in both the growth direction and lateral direction, as shown by the inset in Fig. 9.3(a). Along the center of the QD, the indium

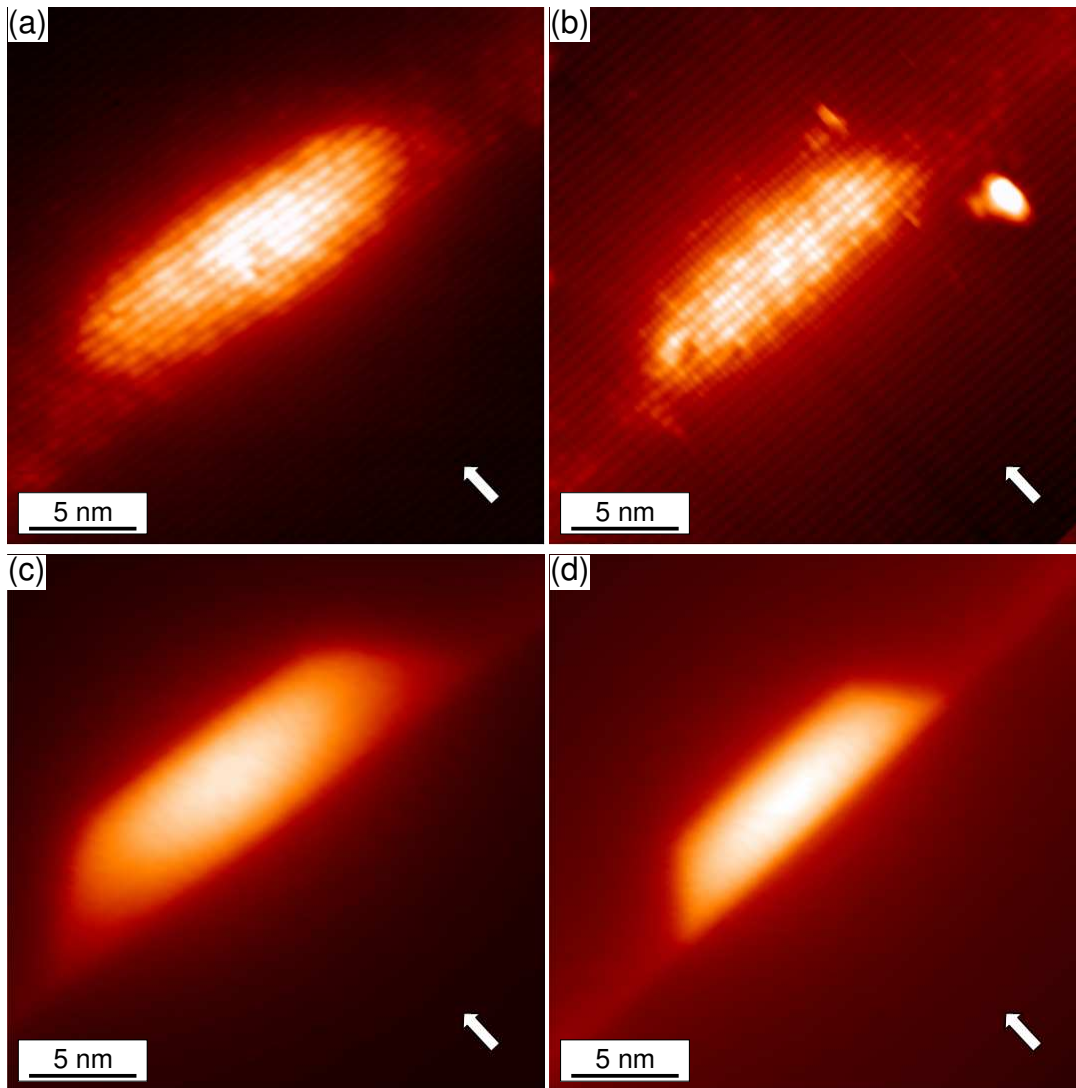


Figure 9.2: Filled states topography X-STM images of (a) InAs/GaAs QD (b) InAs/AlAs QD. (c) and (d) show the calculated outward relaxation corresponding to (a) and (b). The height scale for (a) and (c) is 0 (dark) to 600 pm (bright). The height scale for (b) and (d) is 0 (dark) to 450 pm (bright). $V_{\text{sample}} = -3 \text{ V}$. The arrows indicate the growth direction.

concentration increases from 80% at the base to 100% at the top of the QD. The gradient in the lateral direction is dependent on the position along the growth direction. At the base of the QD, it varies linearly from 80% to 40% from the core to the perimeter, while at the top of the QD it remains constant. For the InAs/AlAs QD best fit results were obtained by an indium gradient of 85 to 70%

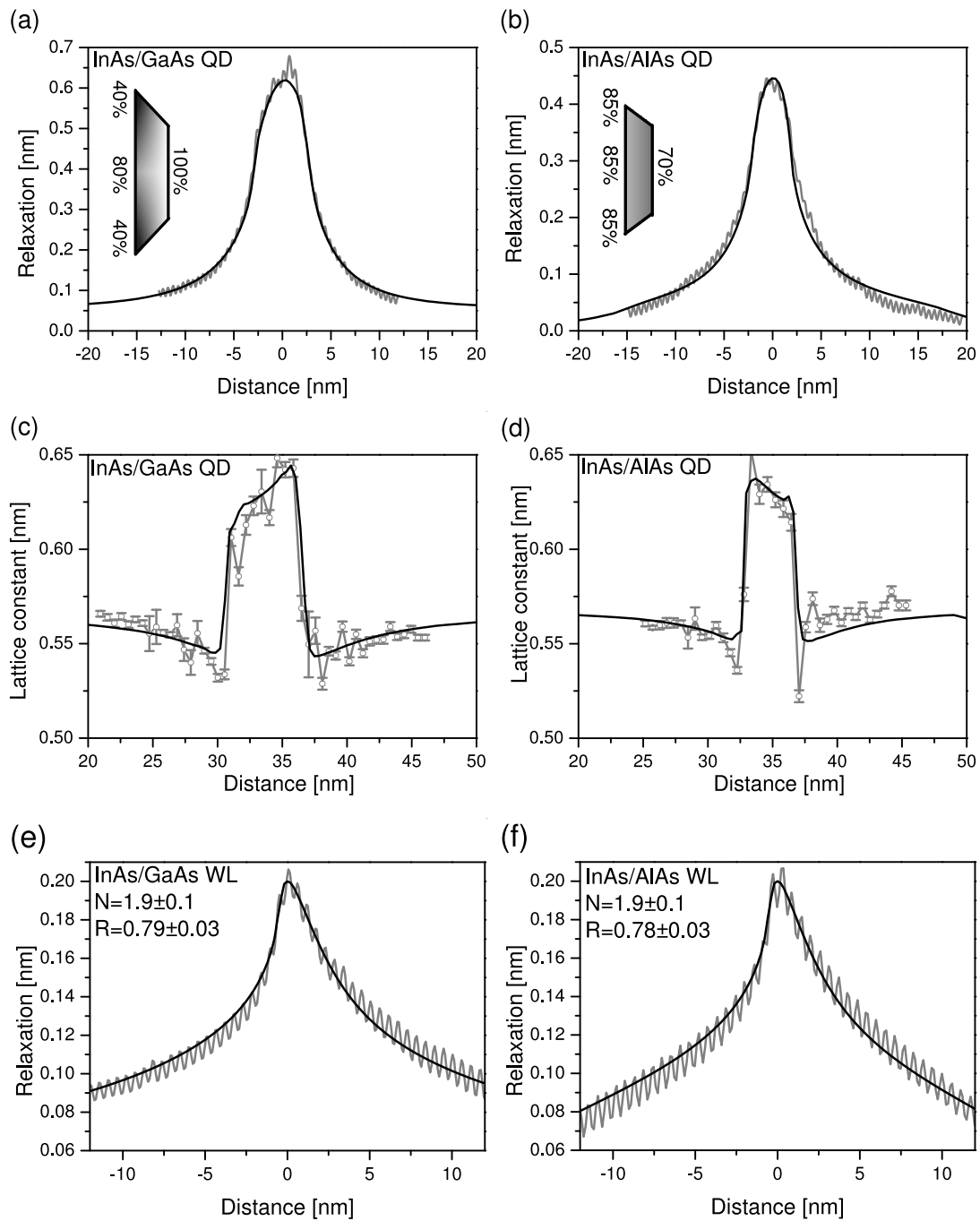


Figure 9.3: Calculated and measured relaxation profiles through the center of the QD in the growth direction, for an InAs/GaAs QD (a) and an InAs/AlAs QD (b). (c) and (d) are the corresponding calculated and measured lattice constant profiles. (e) and (f) are measured and calculated relaxation profiles of the segregated wetting layers in GaAs (e) and AlAs (f). The growth direction is from left to right.

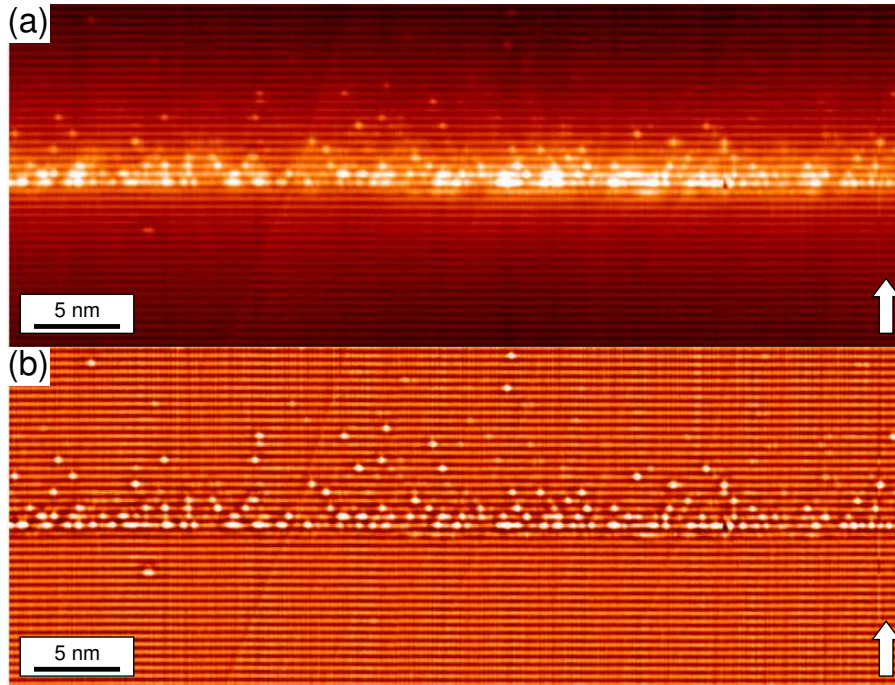


Figure 9.4: Filled states topography X-STM image of the InAs/AlAs segregated wetting layer (a). By using an inverse Fourier filter, the background contrast is removed (b). The arrow indicates the growth direction.

decreasing from base to top of the QD, as shown by the inset in Fig. 9.3(b). In this case there is no evidence for a lateral gradient in the indium composition.

We attribute the observed differences in indium composition and size of the QDs in GaAs and AlAs to the combined effects of (a) the reduced diffusion of In on AlAs compared to GaAs, (b) the reduced intermixing for the InAs WL on AlAs, and (c) the capping process. It is known that the indium accumulation in QDs is determined by strain minimization during growth [85, 86]. However, the preferential indium aggregation at the In-rich region of the dot is limited by the lateral diffusion of indium in the case of growth on the AlAs substrate, resulting in a reduced QD size and increased QD density [65].

Furthermore, it has been shown [87] that there is less intermixing for an InAs WL on AlAs compared to an InAs WL on GaAs. Together with the reduced mobility of In on AlAs, this explains the homogeneous indium distribution in the base of the InAs/AlAs QDs. It has been proposed that the growth of dots on AlAs is initiated by 2D islands which develop into small 3D islands when more InAs is deposited [87]. This is in contrast to the growth of dots on GaAs where dot formation is initiated by small indium-rich nucleation centers which develop into trumpet-shaped indium distributions by the preferential diffusion of In to the

apex of the dot [54]. These growth mechanisms are supported by our observation of the indium distribution inside the dots.

The observed decrease of the indium concentration towards the top of the InAs/AlAs QD might be caused by the residual incorporation of AlAs in the top of the dot during the capping process. In order to reduce the total strain field in the QD some capping material is incorporated in the top of the dot. In the case of GaAs capping, the diluted part of the dot is very mobile and therefore disappears very quickly during capping, causing leveling of the QDs [63]. The InAs diluted by Al, however, is much less mobile due to the stronger Al–In bond strength and therefore more diluted material at the top remains in place.

Finally, the difference in the formation of QDs in AlAs and GaAs cannot be attributed to a different vertical indium segregation process in AlAs and GaAs. An image of the vertical segregation of the wetting layer of the InAs/AlAs dots structure is shown in Fig. 9.4. Figure 9.3 shows the measured and calculated relaxation profiles for the segregated wetting layer in AlAs (e) and GaAs (f). The calculated relaxation profiles have been derived using the phenomenological model of Muraki *et al.* [59] to describe the indium segregation profile. We find a segregation coefficient of $R = 0.79 \pm 0.03$ and $R = 0.78 \pm 0.03$ for GaAs and AlAs, respectively, in agreement with Ref. [55]. This indicates that strain rather than the chemical bond strength determines the vertical indium segregation.

9.3.2 Photoluminescence

We have calculated, on the basis of our structural analysis, the single particle bound electron and hole states in both the InAs/GaAs and InAs/AlAs QDs shown in Fig. 9.2. We use the electron and hole ground state energies to estimate the energy of the ground state exciton and compare this to the photoluminescence results shown in Fig. 9.5. The InAs/GaAs dots show a second PL peak around 1.13 eV, which we attribute to a bimodal size distribution since it does not depend on the excitation density. The bimodal size distribution was confirmed by atomic force microscopy measurements on the top (uncapped) layer. The broad PL spectrum of InAs/AlAs dots has been attributed to a unimodal dot size distribution [83].

The calculation of the bound electron and hole states is performed with the method of Roy and Maksym [88] in which the single band, effective mass Hamiltonian is diagonalized in a basis of harmonic oscillator functions. Within this approximation the strain dependence of the band gap is included exactly in the Hamiltonian, while the strain dependence of the electron and hole mass is included with perturbation theory [89, 30]. In our calculation the dot structures and composition variations are taken directly from our X-STM measurements. We linearly interpolate the band parameters and effective masses to obtain the values relevant to the (In,Ga)As and (In,Al)As alloy material in the QDs.

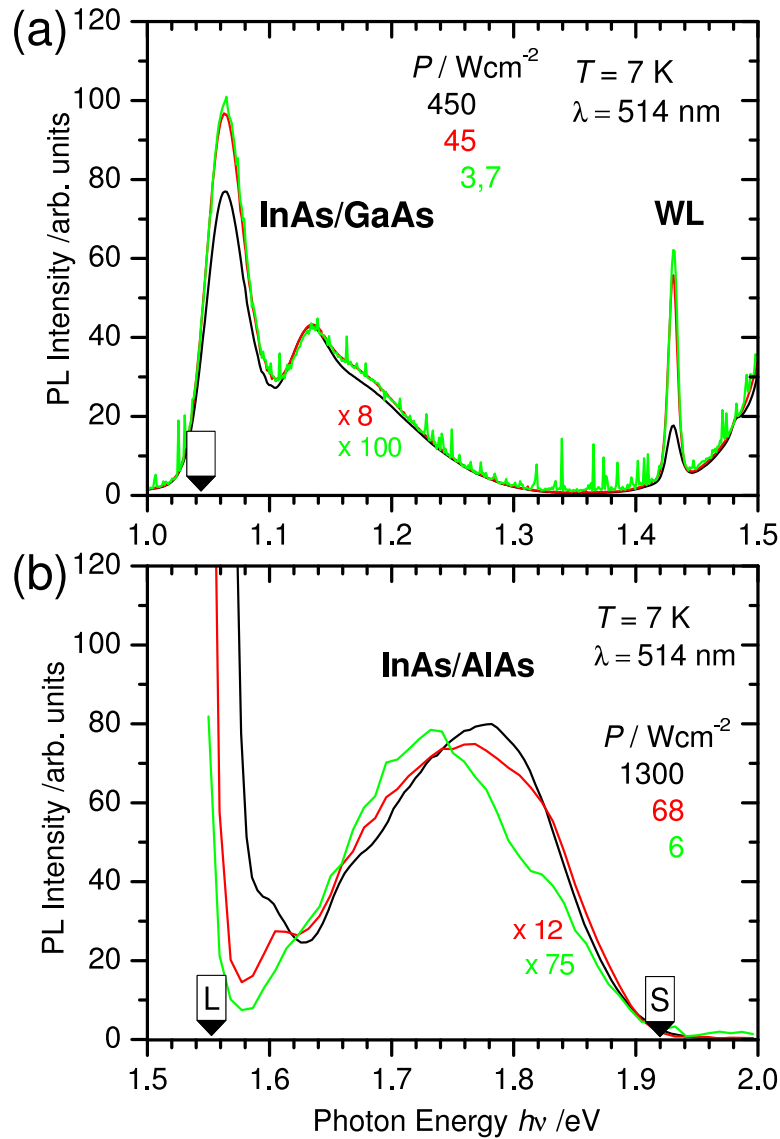


Figure 9.5: Photoluminescence (PL) of InAs/GaAs (a) and InAs/AlAs (b) dots measured at 7 K. The double peak from the InAs/GaAs dots (a) indicates a bimodal size distribution which was confirmed by atomic force microscopy measurements of the uncapped dot layer on the sample surface. The calculated ground state PL energy is indicated by the arrow. The broad PL peak of the AlAs dots (b) can be attributed to a dot size distribution of about 10–20 nm in diameter and 2.4–4.2 in height. The large increase in PL intensity at the low energy end of the spectrum is due to band gap recombination of the GaAs substrate. The arrows labeled L and S indicate the calculated ground state PL energy for large and small dots as discussed in the text. The PL was measured by Klaus Pierz, PTB Braunschweig.

Band parameter	AlAs			InAs		
	Γ	X	L	Γ	X	L
E_c (eV) *	3.13	2.42 ^e	2.46	1.27	2.29	1.99
m_e^{\parallel}	0.124 ^b	0.22	0.26	0.023 ^c	0.16	0.09
m_e^z	0.124 ^b	0.97	0.21	0.023 ^c	1.13	0.07
a_c (eV)	-5.64 ^a	4.30	-1.31	-5.08 ^c	1.50	-2.31
m_h^{\parallel}	0.21 ^d			0.036 ^c		
m_h^z	0.403 ^d			0.34 ^c		
a_v (eV)	2.47 ^a			1.00 ^c		
b (eV)	-1.5 ^a			-1.8 ^c		

Table 9.1: Electron and hole parameters for AlAs and InAs.

*Band gaps taken from Ref. [90] and aligned according to Ref. [25]. The values are relative to the AlAs valence band edge.

^aFrom Ref. [25], ^bfrom Ref. [91], ^cfrom Ref. [30], ^dfrom Ref. [92], ^efrom Ref. [93]. The deformation potentials a_c , at X and L are obtained from data given in Ref. [94]. Electron parallel (m_e^{\parallel}) and perpendicular (m_e^z) masses at X and L are taken from Ref. [90].

It is well known that a single band calculation adequately describes the electron states and the hole ground state [30] in InAs/GaAs QDs. For the calculation of the electron and hole ground state of the InAs/GaAs QD shown in Fig. 9.2(a), we use the band parameters given in Ref. [30], and converge the calculated electron and hole energies to within 0.1 meV. We estimate the ground state photoluminescence energy from the electron E_e and hole E_{hh} ground state energies as $\hbar\omega \approx |E_e| - |E_{hh}| - 10$ meV, where the 10 meV is a rough approximation to the electron-hole interaction energy. With $E_e = 1275.9$ meV and $E_{hh} = 222.3$ meV, we find a PL energy of $\hbar\omega \approx 1044$ meV, which corresponds to the observed PL peak position to within 15 meV (shown by the arrow in Fig. 9.5(a)). Since we look for the largest dots in the X-STM measurements, we expect that the calculated PL energy is at the low energy side of the observed PL peak.

In contrast to InAs/GaAs QDs, the electron states in InAs/AlAs QDs may be bound at the Γ , X or L point. We have calculated the electron and heavy hole single band envelope functions using the band parameters shown in Table 9.1. The calculated electron and hole energies are converged to within 0.5 meV. The slower convergence in this type of QD, compared to the InAs/GaAs QDs, is due to the much larger confinement potential.

From the Γ bound electron ($E_e = 2175$ meV) and hole states ($E_h = 611$ meV) in the InAs/AlAs QD shown in Fig. 9.2(b), we estimate a ground state PL energy

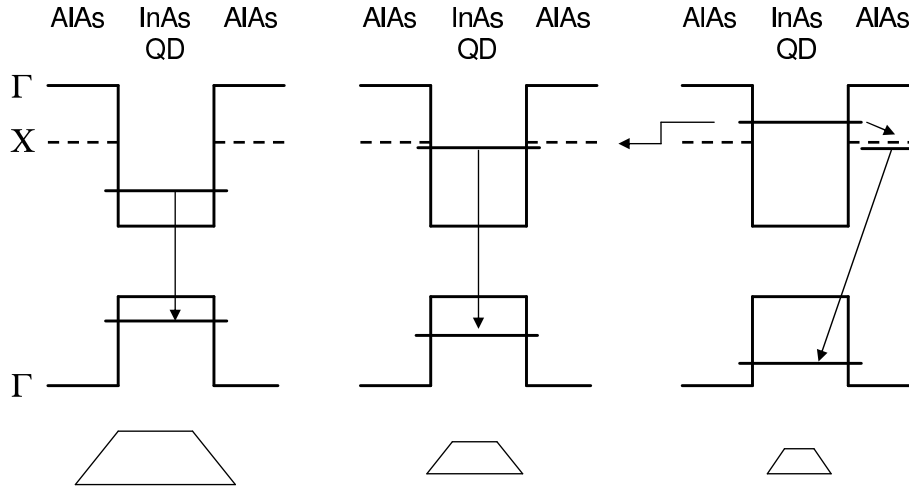


Figure 9.6: Band scheme for differently sized InAs QDs embedded in an AlAs barrier, showing the shift of the lowest Γ -bound electron state above the AlAs X conduction band edge with decreasing dot size. For the smallest dot the Γ -electron is no longer confined to the dot and recombination involves a dispersive electron state [81]. These electrons may also scatter to the surrounding GaAs matrix or to larger QDs [82].

of $\hbar\omega \approx 1554$ meV, which corresponds to the low energy side of the broad PL peak spectrum as shown by the “L” arrow in Fig. 9.5(b). As stated previously, this is to be expected since the analyzed InAs/AlAs dot is one of the largest in the sample, as observed by X-STM.

The broad PL spectrum of InAs/AlAs dots has been attributed to a spread in dot size [83]. To investigate this, we repeated the calculation for smaller InAs/AlAs QDs with the same shape as the large dot and the same vertical variation in indium fraction from 85 to 70%. For a dot with a height of 2.4 nm and diameter of 10.8 nm, we find that the lowest Γ bound state shifts up in energy by 246 meV while the heavy hole ground state moves down by 120 meV. This results in a PL energy of $\hbar\omega \approx 1920$ meV, which corresponds to the high energy side of the PL spectrum in Fig. 9.5(b), as indicated by the “S” arrow. It is difficult to determine the smallest dot size from cross-sectional images since the position of the cleavage plane is unknown. The existence of InAs/AlAs QDs as small as 8 nm in diameter has been reported in the literature [83]. However, if we decrease the QD diameter below 10.8 nm we find that the lowest energy state at Γ moves above the AlAs X band edge, and is no longer confined to the dot. In such small QDs, the recombination becomes both spatially indirect and indirect in k -space, and is therefore expected to give only a weak contribution to the PL.

For the large QD, we find that the L bound ground state is well above (114 meV) the Γ bound ground state. There is a large spread in the reported values

for the position of the AlAs conduction band edge at X [93, 25]. We find that the AlAs X band edge may be either above or below the unstrained InAs X band edge. In either case, the band edge deformation potential is positive at the X point [94], and the large compressive strain in the QD lowers the dot X band edge below that of the AlAs barrier, leading to a weakly bound state in the X valley. Using the parameters shown in Table 9.1, we find that the X bound electron state in the large InAs/AlAs QD, shown in Fig. 9.2(b), is 74 meV above the Γ bound electron state. In the small InAs/AlAs QD discussed earlier, the lowest Γ bound electron state coincides with the AlAs X band edge and is 123 meV above the X bound state. If we assume that the normally forbidden Γ - X transitions *do* contribute to the PL, these transitions would only contribute in the narrow energy window between 1628 and 1796 meV. We therefore conclude that the large width of the PL peak shown in Fig. 9.5(b) is due to Γ - Γ electron-hole recombination, with the low energy side of the PL peak determined by the largest dots, such as the one analysed by X-STM, and the high energy side determined by the smallest dots that contribute to the PL. These could be either the smallest dots in the distribution or the smallest dots that have a direct Γ - Γ transition.

It has been suggested [82] that QDs without a bound electron state, do not contribute to the PL, since electrons can rapidly scatter via the X states in the AlAs barrier, to the surrounding GaAs matrix or to larger QDs, where Γ - Γ transitions are allowed, as shown in Fig. 9.6. Repeated scattering would cause the extremely long decay times (microseconds) observed in InAs/AlAs QDs [82]. However, such long decay times have also been observed for excitation ($\hbar\omega = 1.82$ eV) *below* the AlAs X conduction band edge [83]. This has been explained by enhanced exchange splitting of strongly confined exciton levels in small InAs/AlAs QDs [83], which would lead to a dark ground state [95] in the smallest InAs/AlAs QDs. Due to the high QD density, carriers could transfer from the small dots to larger ones [77] with a smaller splitting, and eventually recombine. We have estimated the exchange splitting of the small InAs/AlAs QD discussed previously by calculation of the electron-hole wave function overlap $P \sim \int \psi_e(\mathbf{r})\psi_h(\mathbf{r})d\mathbf{r}$ [96]. We find that this is 7.6 times larger than that of the InAs/GaAs QD, which will clearly lead to an enhancement in the exciton exchange splitting in InAs/AlAs QDs.

9.4 Conclusion

To summarize, we have determined the size, shape and composition of InAs/GaAs QDs and InAs QDs embedded in an AlAs barrier, by X-STM. The outward relaxation and lattice constant of the cleaved surface of the QDs and their wetting layers were calculated using continuum elasticity theory and compared with experimental data in order to determine the indium concentration of the dots. Based on the structural results we have calculated the electronic ground states of the

dots using a single band, effective mass approach. We find that the calculated ground state photoluminescence energy of the InAs/GaAs dots is in excellent agreement with the measured energy. The observed large width of the PL spectrum of InAs/AlAs dots can be attributed to Γ - Γ electron-hole recombination within an ensemble of dots with sizes varying between 2.4–4.2 nm in height and 10–20 nm along the base diagonal. We find that the electron-hole wave function overlap of small InAs/AlAs QDs is 7.6 times larger than that of InAs/GaAs QDs grown under the same conditions. This supports the explanation that the long decay times in InAs/AlAs dots are caused by an enhanced exciton exchange splitting.

This work was done in collaboration with M. Roy and P. A. Maksym, University of Leicester, UK, and K. Pierz, Physikalisch-Technische Bundesanstalt Braunschweig, Germany.

10

Capping process of InAs/GaAs quantum dots

The capping process of self-assembled InAs quantum dots (QDs) grown on GaAs (100) substrates by molecular-beam epitaxy is studied by cross-sectional scanning tunneling microscopy. GaAs capping at 500°C causes leveling of the QDs which is completely suppressed by decreasing the growth temperature to 300°C. At elevated temperature the QD leveling is driven in the initial stage of the GaAs capping process while it is quenched during continued overgrowth when the QDs become buried. For common GaAs growth rates, both phenomena take place on a similar time scale. Therefore, the size and shape of buried InAs QDs are determined by a delicate interplay between driving and quenching of the QD leveling during capping which is controlled by the GaAs growth rate and growth temperature.

10.1 Introduction

Self-assembled quantum dots (QDs) formed in the Stranski-Krastanov growth mode attract great efforts due to their enormous potential for basic physics studies and device applications. For most cases, the QDs are embedded in a semiconductor matrix, i.e., are capped subsequent to their formation. Both the formation and the capping process are crucial for the structural and electronic properties of the QDs. In particular, the capping process may induce drastic changes in size and shape of the QDs, as has been observed in the Ge/Si(100) [97] and InAs/GaAs(100) [98, 99, 42] material systems. Leveling of InAs/GaAs QDs after

deposition of thin GaAs cap layers has been clearly revealed by top-view scanning tunneling microscopy (STM) [98, 99] and atomic force microscopy (AFM) [42]. The leveling process has been attributed to the additional strain build up between the cap layer and the partially relaxed InAs QDs [98, 42] to destabilize the QDs. These experiments, however, lack information about the shape and, in particular, the residual height of the QDs, which is the most important parameter determining the electronic properties. In this chapter, we study the capping process of InAs QDs on GaAs(100) by cross-sectional STM (X-STM). Detailed and accurate results of the QD leveling are presented, which are essential for understanding the capping process and the control of the structural and electronic properties of InAs QDs.

10.2 Sample description

The samples were grown by solid source molecular-beam epitaxy (MBE) on Si-doped n-type GaAs(100) substrates. After oxide desorption at 580°C, a 150 nm thick GaAs buffer layer was grown. Then the substrate temperature was lowered to 500°C for deposition of 2.1 MLs InAs. Formation of InAs QDs was verified by the sharp transition from streaky to spotty of the reflection high-energy electron diffraction pattern. Thereafter, for samples A–D different capping procedures were applied:

- (A) Deposition of 10 nm GaAs at 500°C followed by 150 nm GaAs growth at 580°C;
- (B) cooling down the sample to 300°C before capping the InAs QDs by 10 nm GaAs at the same temperature and growth of 150 nm GaAs at 580°C;
- (C) capping the InAs QDs by 3 MLs GaAs at 500°C, then cooling down the sample to 300°C for deposition of 150 nm GaAs; and
- (D) capping the InAs QDs by 3 MLs GaAs at 500°C followed by a growth interruption (GI) of time t , deposition of 10 nm GaAs at the same temperature, and growth of 50 or 150 nm GaAs at 580°C.

In sample D five such InAs QD layers were inserted with GI times t of 0, 20, 40, 60, and 90 seconds, separated by 60 nm GaAs and 150 nm GaAs on top. An extra 30 nm GaAs spacer was grown as a marker between the QD layers with GI times t of 40 and 60 seconds. The time for cooling down samples B and C from 500 to 300°C was four minutes. The growth rates were 0.58 and 0.06 ML/s for GaAs and InAs, respectively, and the As_4 beam equivalent pressure was 1×10^{-5} Torr. The samples were grown by Q. Gong.

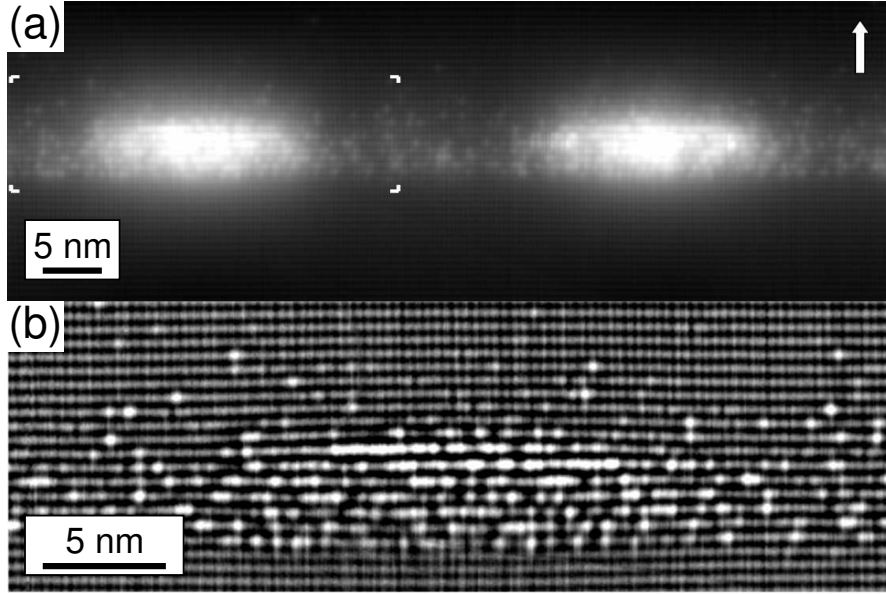


Figure 10.1: (a) Filled states topography X-STM image of the InAs QDs in sample A with conventional capping by 10 nm GaAs at 500°C and 150 nm GaAs at 580°C. $V_{\text{sample}} = -3.0$ V. A part of the image (a) marked by four corners is treated by a local mean equalization filter and shown in (b). In (a) the arrow indicates the growth direction. The black-to-white height contrast in (a) is 0 to 0.5 nm.

10.3 Results

Figure 10.1(a) shows the filled states topography X-STM image of the InAs QDs in sample A which are capped in the conventional way by 10 nm GaAs at 500°C and 150 nm GaAs at 580°C. Part of the image shown in Fig. 10.1(b) is treated with a local mean equalization filter to enhance atomic details by removing the large scale background contrast. The bright horizontal lines are the top zig-zag rows of the (110) surface, which are separated by one bilayer (BL), i.e., two MLs. The topographical contrast in Fig. 10.1(a) is due to the outward relaxation of the cleaved surface of the compressively strained InAs QDs, revealing their cross-sectional shape [28]. The bright spots in Fig. 10.1(b) correspond to In atoms in the top layer of the cleaved surface. The height of the InAs QDs in sample A is measured as 8 BLs by counting the number of atomic rows.

It is well established that InAs QDs buried in the conventional way of sample A exhibit a reduced height compared to unburied ones due to QD leveling [98, 99, 42]. In order to determine the QD height reduction, the shape change during overgrowth of the InAs QDs in sample B is strongly suppressed by capping them at 300°C. The filled states topography X-STM image of an InAs QD in sample B is shown in Fig. 10.2(a) with the filtered image in Fig. 10.2(b). The InAs

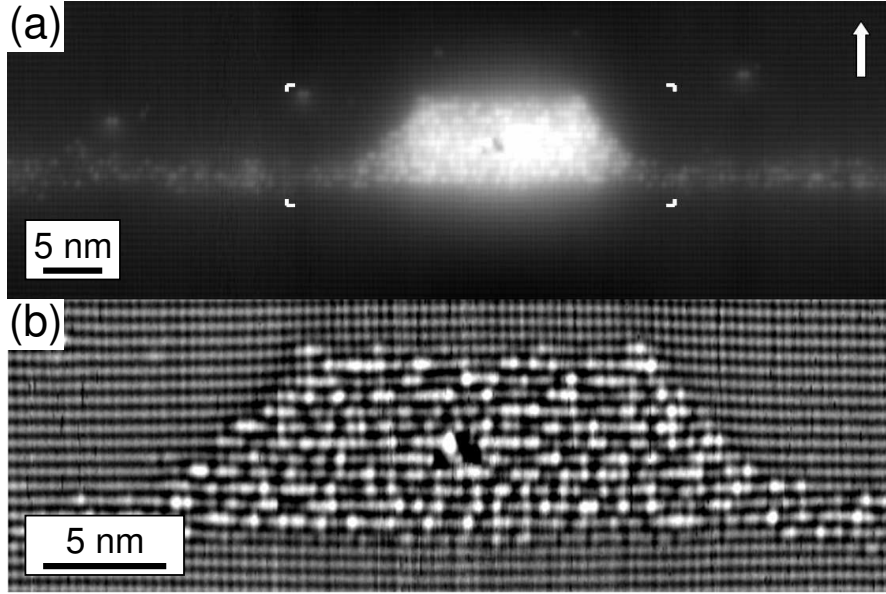


Figure 10.2: (a) Filled states topography X-STM image of the InAs QD in sample B with the GaAs cap grown at 300°C. $V_{\text{sample}} = -3.0$ V. A part of the image (a) marked by four corners is treated by a local mean equalization filter and shown in (b). In (a) the arrow indicates the growth direction. The black-to-white height contrast in (a) is 0 to 0.5 nm.

QD exhibits very sharp and well-defined interfaces confirming the suppressed QD leveling, atom diffusion, and segregation [57] and, thus, the preservation of the QD shape [97, 100]. The height of the InAs QD is 12 BLs which is 4 BLs larger than that of the QDs in sample A. This indicates that during conventional capping at 500°C the QD height is reduced by about one third of the original one.

When InAs QDs are capped by only a very thin GaAs layer, strong QD leveling or QD collapse occurs [98, 42]. Figure 10.3(a,b) shows the filled states topography and filtered images of such InAs QDs in sample C. The QDs are capped at 500°C by 3 MLs GaAs and subsequently overgrown at 300°C to further maintain the shape. During the thin GaAs capping and cooling down, the leveling of the InAs QDs leads to a rather homogeneous (In,Ga)As layer in-between the QDs due to In detachment from the QD tops, Ga/In intermixing, and indium segregation. The thickness of this layer is about 4 BLs. This is much thicker than the original InAs wetting layer. Intermixing with the GaAs substrate [101] expected during the growth of InAs at 500°C additionally contributes approximately 3 MLs of GaAs to the (In,Ga)As layer, which is derived by subtracting the thicknesses of deposited InAs (2.1 MLs) and GaAs (3 MLs) from the total (In,Ga)As thickness of 4 BLs. After leveling of the QDs, unincorporated In floating on the surface

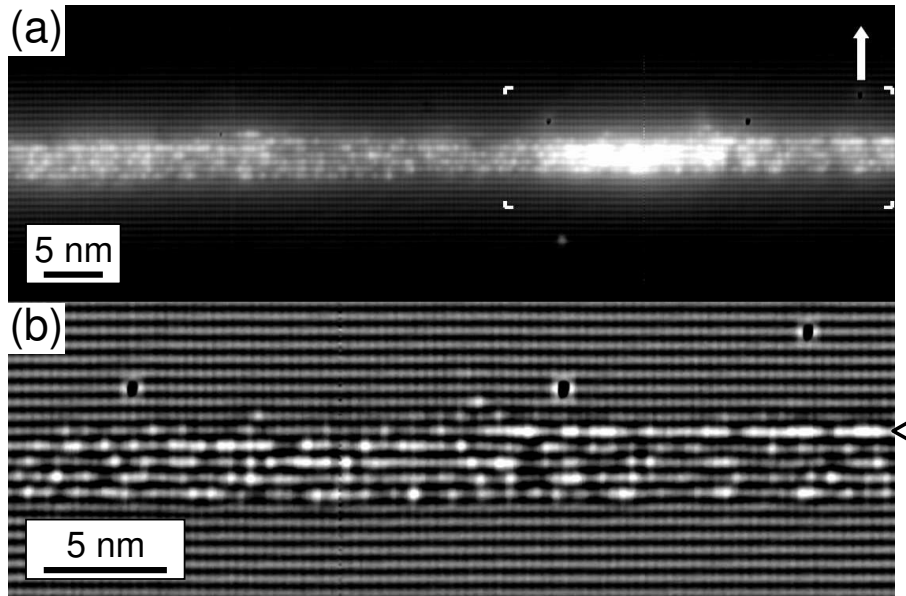


Figure 10.3: (a) Filled states topography X-STM image of the InAs QD in sample C capped by 3 MLs GaAs at 500°C, followed by 150 nm GaAs grown at 300°C. $V_{\text{sample}} = -3.0$ V. A part of the image (a) marked by four corners is treated by a local mean equalization filter and shown in (b). In (a) the arrow indicates the growth direction. The black-to-white height contrast in (a) is 0 to 0.4 nm. The arrow in (b) points to the In-rich layer. The three dark features in (b) are As vacancies due to the low temperature capping.

is pinned there by the low-temperature GaAs capping and forms an In-rich layer marked by the arrow in Fig. 10.3(b). The sharp interface between this layer and the low-temperature GaAs cap confirms that In segregation and diffusion in growth direction are strongly suppressed for GaAs overgrowth at 300°C. Most interestingly, the InAs QDs are completely leveled to the thickness of the (In,Ga)As layer in-between them, which is much smaller than the height of the QDs observed in samples A. This suggests that the conventional, continuous GaAs capping at 500°C in sample A not only drives QD leveling during the initial stage, like the thin GaAs capping in sample C, but also quenches the leveling process when the QDs become buried.

To assess the time scale of QD leveling which is, therefore, crucial for the final size and shape of the buried QDs, varying GI times are inserted in sample D after deposition of 3 MLs GaAs at 500°C on the InAs QDs prior to GaAs overgrowth. Figure 10.4 shows the filled states topography image of the InAs QDs in sample D with GI times of 0, 20, 40, 60, and 90 seconds in subsequent layers. Clearly, the height of the InAs QDs capped without GI (first layer) is significantly larger than

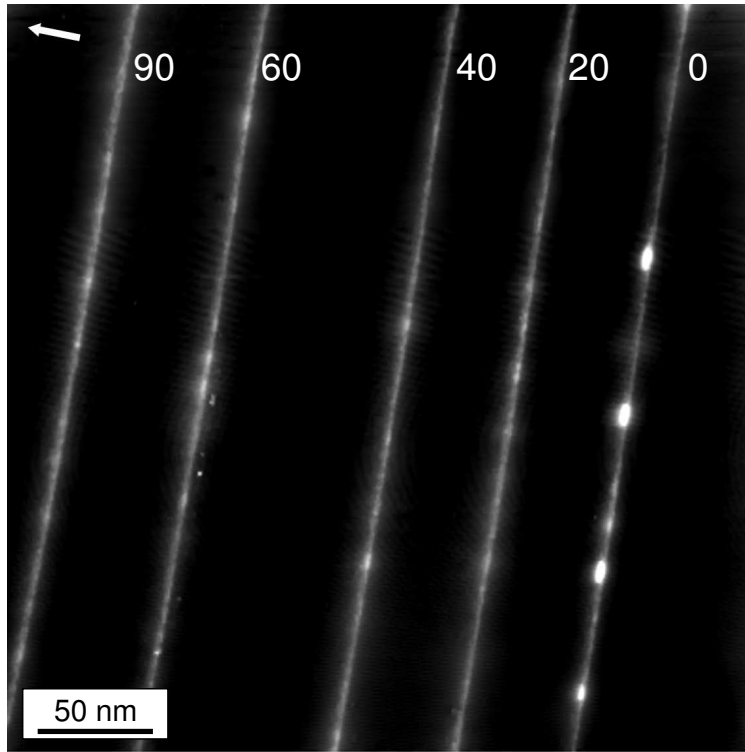


Figure 10.4: Filled states topography X-STM image of the five InAs QD layers in sample D. The InAs QDs are capped by 3 MLs GaAs at 500°C, followed by a GI and a 10 nm GaAs cap grown at 500°C plus a GaAs separation layer at 580°C. $V_{\text{sample}} = -3.0\text{ V}$. The increasing GI times of 0, 20, 40, 60, and 90 seconds are noted in the image. The arrow indicates the growth direction. The black-to-white height contrast is 0 to 0.5 nm.

that of the QDs with insertion of 20 seconds GI. No significant further decrease in QD height is observed when the GI time is increased up to 90 seconds. Hence, QD leveling during thin GaAs capping and GI takes place on a time scale of less than 20 seconds. For the present GaAs growth rate, this is comparable to the time required for growing several nanometers of GaAs to bury the QDs by continuous overgrowth. This indicates that both the driving and quenching of the QD leveling in conventional capping take place on a similar time scale. The size and shape of the buried QDs are therefore determined by a delicate interplay between driving and quenching of the QD leveling which is controlled by the GaAs growth rate and growth temperature.

A model based on the above experimental results is proposed for the growth of InAs QDs embedded in GaAs. The growth of InAs commences in the two-dimensional (2D) layer-by-layer mode until the InAs thickness reaches the critical value of 1.7 MLs for InAs QD nucleation to reduce the accumulated strain. The

InAs QDs are formed by In atoms transported massively from the 2D InAs layer, leaving a thin wetting layer on the surface. The whole system is stable and at the minimum of the total energy composed of the surface energy, the strain energy, and the interface energy. Subsequent capping of the InAs QDs by GaAs, on the other hand, introduces extra strain energy between the GaAs cap and the InAs QD layer, resulting in an unstable system and the consequent QD leveling process. In atoms are redistributed from the InAs QD tops to the area in-between them during the QD leveling. They contribute to a several nanometers thick (In,Ga)As layer [Fig. 10.1] with an exponential In composition decay due to In segregation and Ga/In intermixing during overgrowth [56], reducing the lattice mismatch and, hence, the total energy of the system. Thus, the thickness and the In composition profile of the (In,Ga)As layer in-between the InAs QDs strongly depends on the QD leveling and In segregation. It is important to note that the QD leveling is very sensitive to the substrate temperature and can be strongly suppressed at low growth temperatures, where it becomes more and more difficult to break the In-As bonds thermally. In addition to inducing the QD leveling, the GaAs cap buries the InAs QDs, thereby quenching the leveling process during the growth after the interruption. Therefore, the size and shape of the embedded InAs QDs are determined by a delicate interplay between driving and quenching of the QD leveling during capping which depends strongly on the growth rate and growth temperature of the GaAs cap.

10.4 Conclusion

In summary, we have investigated the capping process of InAs QDs grown by molecular-beam epitaxy on GaAs (100) substrates by cross-sectional scanning tunneling microscopy (X-STM). In its initial stage, GaAs capping induces leveling of the QDs to drastically decrease their height. During continuous capping the QD leveling is quenched when the QDs become buried. Both phenomena, driving and quenching of the QD leveling take place on a similar time scale and are very sensitive to the GaAs growth rate and growth temperature. This understanding opens up an efficient route for controlling the size and shape of buried QDs.

11

Atomic-scale structure of self-assembled (In,Ga)As quantum rings in GaAs

We present an atomic-scale analysis of the indium distribution of self-assembled (In,Ga)As quantum rings (QRs), which are formed from InAs quantum dots by capping with a thin layer of GaAs and subsequent annealing. We find that the size and shape of QRs as observed by cross-sectional scanning tunneling microscopy (X-STM) deviate substantially from the ring-shaped islands as observed by atomic force microscopy on the surface of uncapped QR structures. We show unambiguously that X-STM images the remaining quantum dot material whereas the AFM images the erupted quantum dot material. The remaining dot material shows an asymmetric indium-rich crater-like shape with a depression rather than an opening at the center and is responsible for the observed electronic properties of QR structures. These quantum craters have an indium concentration of about 55% and a diameter of about 20 nm, which is consistent with the observed electronic radius of QR structures. Based on the structural information from the X-STM measurements, we calculate the magnetization as a function of the applied magnetic field. We conclude that, although the real QR shape differs strongly from an idealized circular-symmetric open ring structure, there might be a chance to observe Aharonov-Bohm-type oscillations in the magnetization.

11.1 Introduction

Quantum rings (QRs) are a special class of nanostructures that have attracted a lot of attention due to the occurrence of the Aharonov-Bohm effect, which is

specific to the doubly-connected topology of a ring [13, 12, 102, 14, 15, 16, 17]. Particularly interesting are the magnetic properties of such quantum systems, which are related to the possibility of inducing persistent currents. In recent years the fabrication and investigation of self-assembled InAs QRs have been rapidly progressing and led to a large number of theoretical and experimental studies [14, 16, 11, 18, 103, 104, 68, 105].

In(Ga)As QRs are formed by capping self-assembled quantum dots (QDs) grown by Stranski-Krastanov (SK)-mode with a layer thinner than the dot height and subsequent annealing [11]. During this process, anisotropic redistribution of the QD material takes place, resulting in elongated ring-shaped islands on the surface, with crater-like holes in their centers, as was shown with atomic force microscopy (AFM) measurements [11]. The dot to ring transition has been attributed to a dewetting process which expels indium from the QD [106], and a simultaneous strongly temperature dependent Ga-In alloying process [68].

Capacitance and far-infrared spectroscopy on buried QR structures have shown evidence of the first Aharonov-Bohm oscillation [18]. Although no direct measurements were available, an electronic radius of about 14 nm was deduced, which led to the conclusion that the QR shape as determined from AFM topography is preserved when buried [18]. Until recently [107], however, no structural measurements of buried QRs have been available. Furthermore, measurements of the vertical Stark effect of excitons confined to individual QRs [104] have shown rather large dipole moments with opposite sign as compared to QDs [29]. Theoretical calculations have indicated that both the observed electronic radius and dipole moment of the QRs are inconsistent with the geometry as determined by AFM [16]. In order to resolve this discrepancy we have analyzed the shape, size and composition of buried QRs at the atomic scale by cross-sectional scanning-tunneling microscopy (X-STM). Based on the structural information from the X-STM measurements, we calculate the electron energy spectra and the magnetization of the buried QRs.

11.2 Sample description and experimental setup

Twenty layers of QRs separated by 18 nm were grown by solid source molecular-beam epitaxy (MBE) on a Si-doped n-type GaAs (001) substrate. The QRs are formed by the partial capping of InAs QDs grown at 540°C with 2 nm of GaAs and subsequent annealing at 500°C under As₂ flux [68]. On top of the structure a layer of QRs was grown for AFM measurements. The X-STM measurements are performed in an ultra-high-vacuum chamber on the orthogonal (110) and (1 $\bar{1}$ 0) cross-sectional surfaces. In X-STM the QRs are cleaved at a random position with respect to the center of the QR. Therefore, more than 100 QRs were imaged and the largest ones were selected for analysis. It can be then assumed that these QRs are cleaved near their middle. The photoluminescence spectrum shown in Fig.

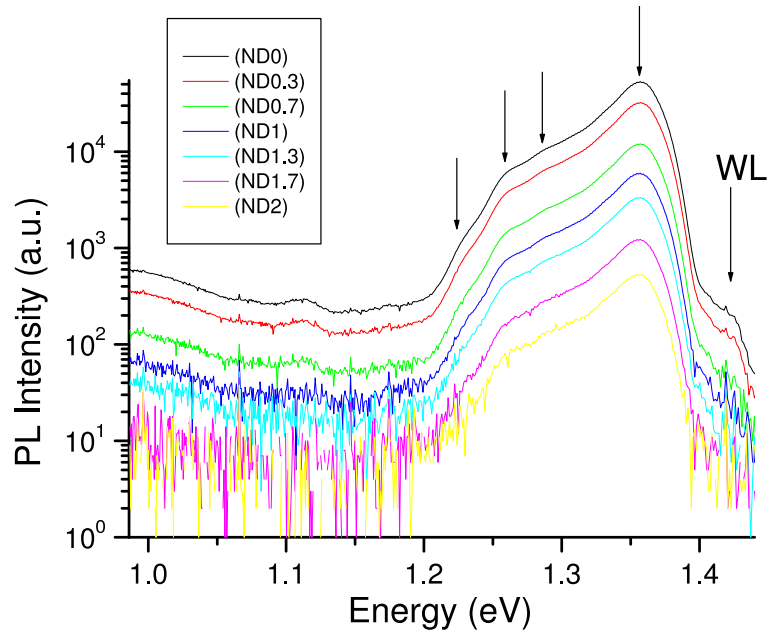


Figure 11.1: PL spectra of the QRs at different excitation densities. Varying the excitation densities was done with the use of ND filters. The ND factor of the filters corresponds to a reduced excitation density with a factor of 10^{ND} . The excitation density of the laser without ND filter is approximately 0.5 Wcm^{-2} . The spectra are taken at $T = 5 \text{ K}$ with a grating of 200 grooves/mm and a blaze of $1.7 \mu\text{m}$ using a exposure time of 10 s. The arrows indicate peaks in the spectrum, which probably are due to QRs with different heights and the wetting layer.

11.1, is identical to that observed for similar QR structures [107, 68]. The samples were grown by J. M. García and D. Granados, Instituto de Microelectrónica de Madrid, Spain.

11.3 Results

Figure 11.2 shows an AFM image of the surface layer of the structure. The ring-shaped islands (density 10^{10} cm^{-2}) are elongated along the $[1\bar{1}0]$ direction, with an outer size of about 100 by 70 nm and an average height of about 1 nm. The holes in the center of the islands are asymmetric as well and have a size of 30 by 20 nm and a depth of about 0.5–1.5 nm.

Figure 11.3 shows a large scale X-STM image of three of the QR layers. The horizontal rows in the image are the top rows of the cleaved (110) surface [22], which are separated by one bilayer (BL), i.e., 0.565 nm, in the $[001]$ direction. The bright spots correspond to In atoms in the top layer of the cleaved surface.

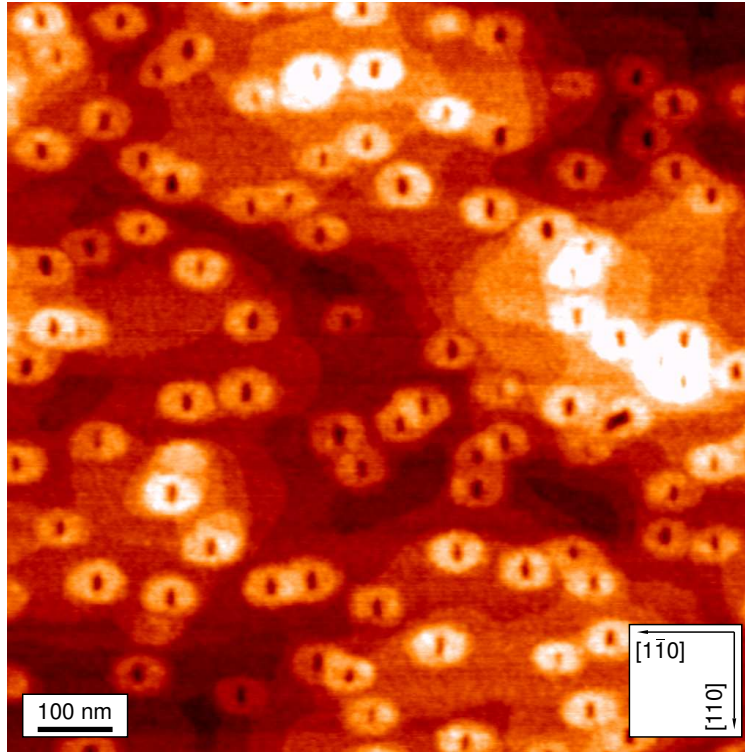


Figure 11.2: $1 \times 1 \mu\text{m}$ atomic force microscopy image showing the anisotropic distribution of InAs/GaAs dot material after 2 nm GaAs capping and 1 minute annealing at growth temperature under As_2 flux. The height scale is 0 (dark) to 2.5 nm (bright). The height of the ring-shaped islands is about 1 nm. Atomic steps can be seen in the image.

In the image the cross-sections of two flat indium-rich nanostructures can be seen. Although these structures differ considerably from the ring-shaped islands as observed by AFM, see Fig. 11.2, we will discuss how they are related to each other.

In Fig. 11.4 we present averaged height profiles taken across the middle QR layer in the growth direction between the points A and B. The profiles are averaged over a distance of 10 nm in the $[\bar{1}10]$ direction and clearly indicate two peaks in the indium concentration. The highest peak can be attributed to the wetting layer on which the QDs are formed during growth. The separation between the peaks of 3–4 BLs corresponds to the height of the partial GaAs capping layer. This indicates that the formation of the second peak in the indium concentration occurs during the growth interruption after the partial capping of the QDs. We attribute the presence of the second indium layer to the accumulation of segregated indium from the wetting layer at the surface of the partial capping

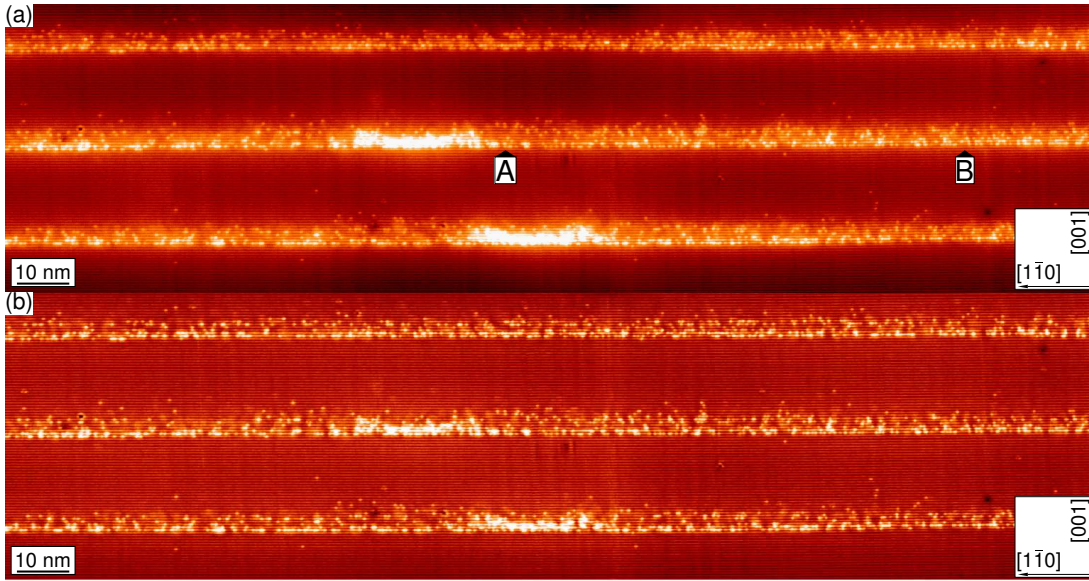


Figure 11.3: (a) Filled states topography image showing two buried QRs, $V_{\text{sample}} = -3\text{V}$. The height profiles shown in Fig. 11.4 are taken between the points A and B. (b) Same image treated with a high-pass filter.

layer and to surface migration of indium atoms that have been expelled from the quantum dots during QR formation [69, 70, 71, 72].

We find that the second indium layer is not only present nearby the nanostructures, but actually extends laterally over the entire cleaved surface. However, by closer inspection of Fig. 11.3 or from the shaded lines in Fig. 11.4, it can be seen that over the distance between points A and B, the separation between the wetting layer and the second indium layer increases with about 2 bilayers towards the nanostructure. This change in separation is in agreement with the height and diameter of the uncapped QRs as measured by AFM. Thus at least to some extent the shape of the ring-shaped islands as observed by AFM is preserved after capping.

Enlarged views of the nanostructures can be seen in Fig. 11.5, where we show filled states topography images of the orthogonal $(1\bar{1}0)$ and (110) cleavage planes, which correspond with the short and long axis of the ring-shaped islands observed by AFM, respectively.

The nanostructures have a crater-like shape which can be attributed to the remainder of the quantum dots after the QR formation process. It can be clearly seen that these quantum craters do not have an opening at the center. Furthermore, in the $[110]$ direction, we generally find that the rim of the quantum crater appears brighter and higher (8 BLs) compared to the $[1\bar{1}0]$ direction where the rim is less pronounced. We attribute this asymmetry to the preferential diffusion of the dot material in the $[1\bar{1}0]$ direction [108] as can be seen from the elongation

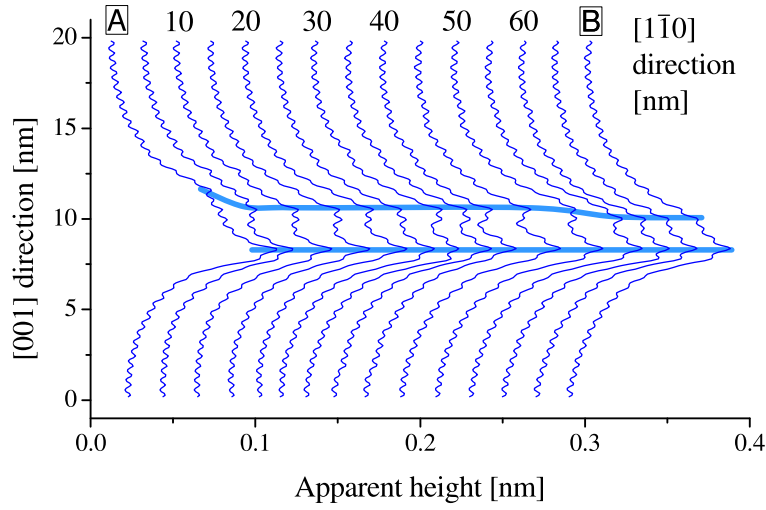


Figure 11.4: Averaged height profiles taken in the growth ([001]) direction across the InAs layer between points A and B of Figure 11.3. The height profiles are averaged over a distance of 10 nm and show two peaks in the indium concentration.

of the ring-shaped islands in Fig. 11.2. The use of As_2 or high As_4 fluxes partially compensates for this anisotropy [68]. The elongation of the ring-shaped islands at the surface implies that, compared to the [110] direction, in the $[1\bar{1}0]$ direction a larger fraction of the original InAs dot has been converted into the (In,Ga)As rim observed by AFM. Therefore it should be expected that the remaining dot material, i.e., the quantum crater, will exhibit a less pronounced rim shape in the $[1\bar{1}0]$ direction.

By imaging at a high voltage ($V_{\text{sample}} = -3\text{ V}$), electronic contributions to the contrast in the image are minimized and only the true outward surface relaxation due to the lattice mismatch (7%) between the InAs and surrounding GaAs is imaged. We use the outward relaxation of the cleaved surface, to determine the indium composition of the quantum craters [66, 28]. We model the quantum craters with a varying-thickness (In,Ga)As layer embedded in an infinite GaAs medium. The bottom of the (In,Ga)As layer is assumed to be perfectly flat and parallel to the xy -plane. The expression

$$\begin{aligned}
 h(\rho, \varphi) &= h_0 + \frac{[h_M(1 + \xi \cos 2\varphi) - h_0] \gamma_0^2}{R^2} \\
 &\times \frac{R^2 - (\rho - R)^2}{(\rho - R)^2 + \gamma_0^2}, \rho \leq R, \\
 h(\rho, \varphi) &= h_\infty + \frac{[h_M(1 + \xi \cos 2\varphi) - h_\infty] \gamma_\infty^2}{(\rho - R)^2 + \gamma_\infty^2}, \rho > R,
 \end{aligned}$$

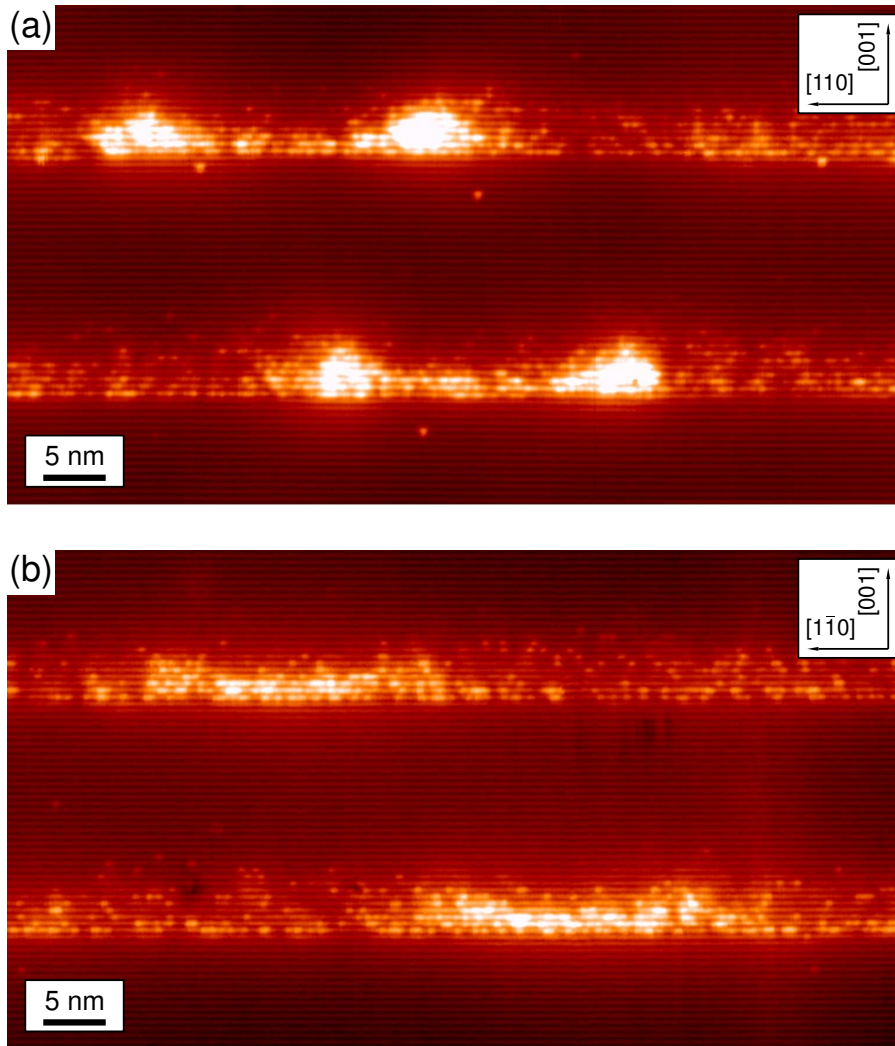


Figure 11.5: Filled states topography image of a cleaved QR in the $(1\bar{1}0)$ plane (a) and (110) plane (b), $V_{\text{sample}} = -3$ V. The height scale is 0 nm (dark) to 0.25 nm (bright).

is used to describe the height of the (In,Ga)As layer as a function of the radial coordinate ρ and the azimuthal angle φ , where R corresponds to the radius of the crater, h_0 to the thickness at the center of the crater, h_M to the rim height and h_∞ to the thickness of the (In,Ga)As layer far away from the ring, and ξ models the asymmetry in the rim height. The γ_0 and γ_∞ parameters define the inner and outer slopes of the rim, respectively. A three-dimensional finite element calculation based on elasticity theory has been used to calculate the relaxation of the cleaved surface of the modeled QR.

With $h_0 = 1.6$ nm, $h_M = 3.6$ nm, $h_\infty = 0.4$ nm, $\gamma_0 = 3$ nm, $\gamma_\infty = 5$ nm, $\xi = 0.2$ and $R = 11.5$ nm and $R = 10$ nm for the quantum craters in Figs. 11.5(a) and 11.5(b), respectively, we find that an indium concentration of $55 \pm 5\%$ results in a calculated surface relaxation that matches the measured relaxation of the cleaved surface.

Our observation that buried QRs have a smaller size and a larger height than the ring-shaped islands as revealed by AFM, offers an explanation for the observed discrepancies between the measured and theoretical values for the electronic radius and dipole moment of the QRs [16]. However, since the real shape of buried QRs deviates considerably from the rather idealized shapes used in theoretical calculations, it is questionable whether these asymmetric crater-like structures can effectively manifest the electronic properties (like the Aharonov-Bohm oscillations) peculiar to doubly connected geometry.

In a ring with reduced (as compared to the C_∞) symmetry, electron states with different magnetic quantum numbers are mixed by the perturbation related to the shape anisotropy. As a consequence, one can expect that for rings with in-plane shape anisotropy the oscillating behavior of the electron magnetic moment induced by the persistent current, μ , as a function of the applied magnetic field H is suppressed as compared to that for isotropic QRs. Since the lateral size of quantum rings substantially exceeds their height ($R \gg h_0, h_M$), we consider the lateral motion of electrons to be governed by the adiabatic potential related to the fast electron motion along the growth axis. The electron states are calculated by diagonalizing the adiabatic Hamiltonian in the basis of in-plane wavefunctions.

Figure 11.6 shows the effect of the ring-shape anisotropy on the oscillations of the electron magnetic moment induced by the persistent current as a function of H . Transition magnetic fields, which correspond to sharp jumps of the magnetic moment due to interchange between the ground and first excited electron energy levels, appreciably increase with increasing the parameter ξ of the ring-shape anisotropy. More importantly, even moderate variations of the height of the rim with the azimuthal angle φ significantly suppress oscillations of μ versus H . Due to a strong dependence of transition magnetic fields on the lateral size of QRs, oscillations of the ensemble average for the magnetic moment, $\langle \mu \rangle$, as a function of H can be further suppressed. Nevertheless, our calculations show that in relatively low magnetic fields ($H < 20$ T) the oscillatory behavior of $\langle \mu(H) \rangle$ survives for ensembles of QRs with radial dispersion as large as 10–20%.

11.4 Conclusion

In conclusion, we have performed an atomic scale analysis of the shape, size and composition of buried self-assembled QRs by cross-sectional scanning tunneling microscopy. We find that these structures show indium-rich asymmetric crater-like shapes which differ substantially from the ring-shaped islands on the surface

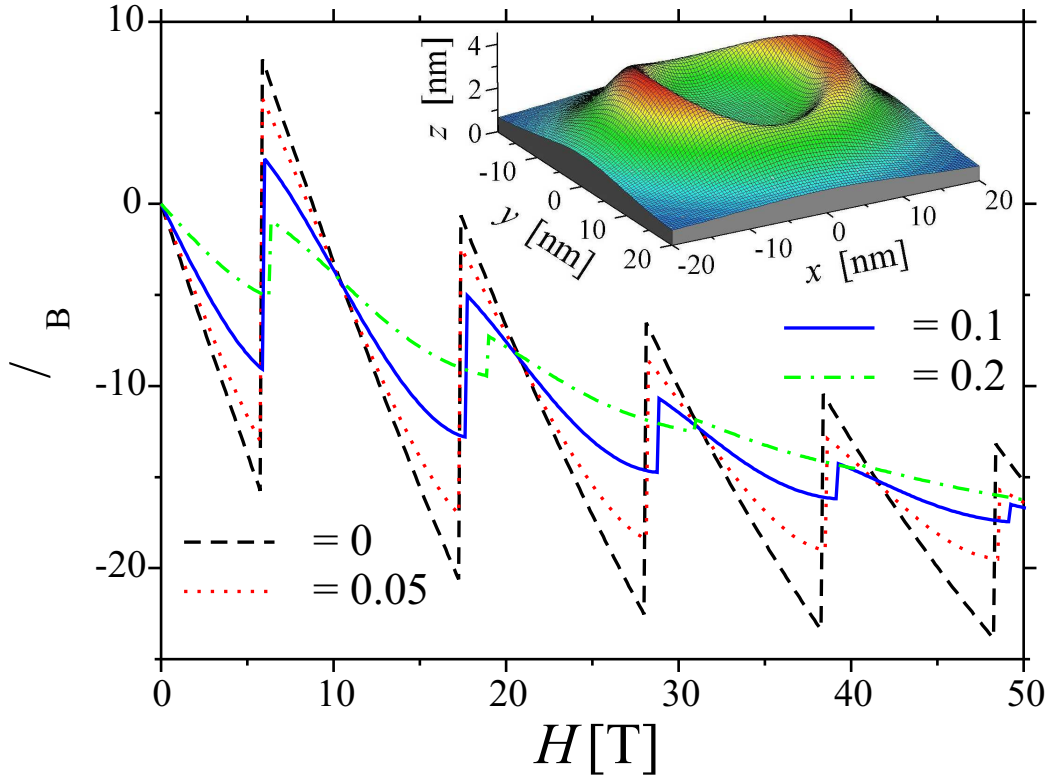


Figure 11.6: Magnetic moment induced by the ground-state persistent current as a function of the applied magnetic field for $\text{In}_{0.6}\text{Ga}_{0.4}\text{As}$ QRs with $R = 11.5$ nm, $h_0 = 1.6$ nm, $h_M = 3.6$ nm, $h_\infty = 0.4$ nm, $\gamma_0 = 3$ nm, $\gamma_\infty = 5$ nm at different values of the parameter ξ of the ring-shape anisotropy, μ_B is the Bohr magneton. Inset: the used model for the shape of QRs for $\xi = 0.2$.

of uncapped QR structures. Our conclusion that such quantum craters have a smaller size and a larger height than the ring-shaped islands, offers an explanation for the observed discrepancies between the measured and theoretical values for the electronic radius and dipole moment of the QRs [16]. Furthermore, we conclude that, although the real QR shape differs strongly from an idealized circular-symmetric open ring structure, there might be a chance to observe Aharonov-Bohm-type oscillations in the magnetization.

This work has been done in collaboration with V. M. Fomin, V. N. Gladilin and J. T. Devreese, Universiteit Antwerpen, Belgium, J. M. García and D. Granados, Instituto de Microelectrónica de Madrid, Spain.

Bibliography

- [1] J. Stangl, V. Holý, and G. Bauer, *Rev. Mod. Phys.* **76**, 726 (2004).
- [2] N. N. Ledentsov, M. Grundmann, F. Heinrichsdorff, D. Bimberg, and V. M. Ustinov *et al*, *IEEE J. Select. Topics. Quant. Electron.* **6**, 439 (2002).
- [3] M. S. Skolnick and D. J. Mowbray, *Annu. Rev. Mater. Res.* **34**, 181 (2004).
- [4] H. C. Liu, M. Gao, J. McCaffrey, S. Wasilewski, and S. Fafard, *Appl. Phys. Lett* **78**, 79 (2001).
- [5] T. Akiyama, H. Kuwatsuka, N. hatori, Y. Nakata, H. Ebe, and M. Sugawara, *Electron. Lett.* **38**, 1133 (2002).
- [6] K. Imamura, Y. Sugiyama, Y. Nakata, S. Muto, and N. Yokoyama, *Jpn. J. Appl. Phys.* **34**, L1445 (1995).
- [7] P. Michler, A. Kiraz, C. Becher, W. V. Schoenfeld, P. M. Petroff, L. Zhang, E. Hu, and A. Imamoglu, *Science* **290**, 2282 (2000).
- [8] M. Bayer, *Nature* **418**, 597 (2002).
- [9] <http://www.innovations-report.de/html/berichte/verfahrenstechnologie/bericht-32085.html>.
- [10] X. Gao, Y. Cui, R. M. Levenson, L. W. K. Chung, and S. Nie, *Nature Biotechnology* **22**, 969 (2004).
- [11] J. M. García, G. Medeiros-Ribeiro, K. Schmidt, T. Ngo, J. L. Feng, A. Lorke, J. Kotthaus, and P. M. Petroff, *App. Phys. Lett.* **71**, 2014 (1997).
- [12] M. Büttiker, Y. Imry, and R. Landauer, *Phys. Letters A* **96**, 365 (1983).
- [13] N. Byers and C. N. Yang, *Phys. Rev. Lett.* **7**, 46 (1961).
- [14] A. O. Govorov, S. E. Ulloa, K. Karrai, and R. J. Warburton, *Phys. Rev. B* **66**, 081309(R) (2002).
- [15] M. Bayer, M. Korkusinski, P. Hawrylak, T. Gutbrod, M. Michel, and A. Forchel, *Phys. Rev. Lett.* **90**, 186801 (2003).

BIBLIOGRAPHY

- [16] J. A. Barker, R. J. Warburton, and E. P. O'Reilly, *Phys. Rev. B* **69**, 035327 (2004).
- [17] S. Viefers, P. Koskinen, P. S. Deo, and M. Manninen, *Physica E* **21**, 1 (2004).
- [18] A. Lorke, R. J. Luyken, A. O. Govorov, J. P. Kotthaus, J. M. García, and P. M. Petroff, *Phys. Rev. Lett* **84**, 2223 (2000).
- [19] J. Bardeen, *Phys. Rev. Lett.* **6**, 57 (1961).
- [20] J. Tersoff and D. R. Hamann, *Phys. Rev. B* **31**, 805 (1985).
- [21] http://en.wikipedia.org/wiki/WKB_approximation.
- [22] R. M. Feenstra, J. A. Stroscio, J. Tersoff, and A. P. Fein, *Phys. Rev. Lett.* **58**, 1192 (1987).
- [23] R. M. Feenstra, *Physica B* **273**, 796 (1999).
- [24] D. M. Bruls, P. M. Koenraad, M. Hopkinson, J. H. Wolter, and H. W. M. Salemink, *Appl. Surf. Sci.* **190**, 258 (2002).
- [25] C. G. Van de Walle, *Phys. Rev. B.* **39**, 1871 (1989).
- [26] J. H. Davies, D. M. Bruls, J. W. A. M. Vugs, and P. M. Koenraad, *J. Appl. Phys* **91**, 4171 (2002).
- [27] J. H. Davies, P. Offermans, and P. M. Koenraad. Accepted for publication in *J. Appl. Phys.*
- [28] D. M. Bruls, J. W. A. M. Vugs, P. M. Koenraad, H. W. M. Salemink, J. H. Wolter, M. Hopkinson, M. S. Skolnick, F. Long, and S. P. A. Gill, *Appl. Phys. Lett.* **81**, 1708 (2002).
- [29] P. W. Fry, I. E. Itskevich, D. J. Mowbray, M. S. Skolnick, J. J. Finley, J. A. Barker, E. P. O'Reilly, L. R. Wilson, I. A. Larkin, P. A. Maksym, M. Hopkinson, M. Al-Khafaji, J. P. R. David, A. G. Cullis, G. Hill, and J. C. Clark, *Phys. Rev. Lett.* **84**, 733 (2000).
- [30] J. A. Barker and E. P. O'Reilly, *Phys. Rev. B* **61**, 13840 (2000).
- [31] K. Sauthoff, M. Wenderoth, A. J. Heinrich, M. A. Rosentreter, K. J. Engel, T. C. G. Reusch, and R. G. Ulbrich, *Phys. Rev. B* **60**, 4789 (1999).
- [32] P. Offermans, P. Koenraad, J. Wolter, M. Beck, T. Aellen, and J. Faist, *Appl. Phys. Lett.* **83**, 4131 (2003).

- [33] D. Zhou, R. Nötzel, Q. Gong, P. Offermans, P. M. Koenraad, P. J. van Veldhoven, F. W. M. van Otten, T. J. Eijkemans, and J. H. Wolter, *J. Appl. Phys.* **97**, 063510 (2005).
- [34] J. He, R. Nötzel, P. Offermans, P. M. Koenraad, Q. Gong, G. J. Hamhuis, T. J. Eijkemans, and J. H. Wolter, *Appl. Phys. Lett.* **85**, 2771 (2004).
- [35] R. Green, L. Wilson, D. Revin, E. Zibik, J. Cockburn, P. Offermans, P. Koenraad, J. Wolter, C. Pflügl, W. Schrenk, G. Strasser, C. Tey, A. Krysa, J. Roberts, and A. Cullis. Submitted to the 17th International Conference on Indium Phosphide and Related Materials, May 8-12, 2005, Glasgow, Scotland, UK.
- [36] R. Green, L. Wilson, D. Revin, E. Zibik, , J. Cockburn, P. Offermans, P. Koenraad, J. Wolter, C. Pflügl, W. Schrenk, G. Strasser, C. Tey, A. Krysa, J. Roberts, and A. Cullis. Submitted to the International Conference on Lasers and Electro-Optics, May 22-27, 2005, Baltimore, Maryland, USA.
- [37] D. Revin, L. Wilson, E. Zibik, R. Green, J. Cockburn, M. Steer, R. Airey, M. Hopkinson, P. Offermans, P. Koenraad, and J. Wolter. Submitted to the International Conference on Lasers and Electro-Optics, May 22-27, 2005, Baltimore, Maryland, USA.
- [38] R. Green, A. Krysa, J. Roberts, D. Revin, L. Wilson, E. Zibik, W. Ng, and J. Cockburn, *Appl. Phys. Lett* **83**, 1921 (2003).
- [39] N. Georgiev and T. Mozume, *J. Appl. Phys.* **89**, 1064 (2001).
- [40] R. Teissier, D. Barate, A. Vicet, C. Alibert, X. Marcadet, C. Renard, M. Garcia, C. Sirtori, D. Revin, and J. Cockburn, *Appl. Phys. Lett* **85**, 167 (2004).
- [41] T. v. Lippen, R. Nötzel, G. J. Hamhuis, and J. H. Wolter, *Appl. Phys. Lett.* **85**, 118 (2004).
- [42] Q. Gong, R. Nötzel, G. J. Hamhuis, T. J. Eijkemans, and J. H. Wolter, *Appl. Phys. Lett.* **81**, 1887 (2002).
- [43] A. J. Springthorpe, T. Garanzotis, P. Paddon, G. Pakulski, and K. I. White, *Electronics Letters* **36**, 1031 (2000).
- [44] J. D. Song, J. S. Yu, J. M. Kim, S. J. Bae, and Y. T. Lee, *Appl. Phys. Lett.* **80**, 4650 (2002).

BIBLIOGRAPHY

- [45] J. D. Song, J. M. Kim, J. S. Yu, S. J. Bae, and Y. T. Lee. Proc. of 14th Indium Pospide and Related Materials Conference. May 12-16, 2002, Stockholm, Sweden, ISBN 0-7803-7320-0, p. 335.
- [46] A. Zunger and S. Mahajan, *Atomic ordering and phase separation in epitaxial III-V alloys*.
- [47] S. W. Jun, T.-Y. Seong, J. H. Lee, and B. Lee, Appl. Phys. Lett. **68**, 3443 (1996).
- [48] R. R. LaPierre, T. Okada, B. J. Robinson, D. A. Thompson, and G. C. Weatherly, J. Cryst. Growth **158**, 6 (1996).
- [49] M. Pfister, M. B. Johnson, S. F. Alvarado, H. W. M. Salemink, U. Marti, D. Martin, F. Morier-Genoud, and F. K. Reinhart, Appl. Phys. Lett. **67**, 1459 (1995).
- [50] T. Aellen, M. Beck, D. Hofstetter, J. Faist, U. Oesterle, M. Ilegems, E. Gini, and H. Melchior. Proc. of the 29th International Symposium on Compound Semiconductors, October 7-10, 2002, Lausanne, Switzerland.
- [51] M. Beck, D. Hofstetter, T. Aellen, J. Faist, U. Oesterle, M. Ilegems, E. Gini, and H. Melchior, Science **295**, 301 (2002).
- [52] A. R. Smith, K.-J. Chao, C. K. Shih, Y. C. Shih, K. A. Anselm, and B. G. Streetman, J. Vac. Sci. Technol. B **13**, 1824 (1995).
- [53] J. H. Marsh, Appl Phys Lett **41**, 732 (1982).
- [54] Migliorato, A. G. Cullis, M. Fearn, and J. H. Jefferson, Phys. Rev. B. **65**, 115316 (2002).
- [55] M. Schowalter, A. Rosenauer, D. Gerthsen, M. Arzberger, M. Bichler, and G. Abstreiter, App. Phys. Lett. **79**, 4426 (2001).
- [56] A. Rosenauer, D. Gerthsen, D. V. Dyck, M. Arzberger, G. Böhm, and G. Abstreiter, Phys. Rev. B **64**, 245334 (2001).
- [57] J. P. Silveira, J. M. García, and F. Briones, Appl. Surf. Science **188**, 75 (2002).
- [58] J. M. Moison, C. Guille, F. Houzay, F. Barthe, and N. V. Rompay, Phys. Rev. B. **40**, 6149 (1989).
- [59] K. Muraki, S. Fukatsu, Y. Shiraki, and R. Ito, Appl. Phys. Lett. **61**, 557 (1992).
- [60] N. Grandjean, J. Massies, and M. Leroux, Phys. Rev. B. **53**, 998 (1996).

- [61] O. Dehaese, X. Wallart, and F. Mollot, *Appl. Phys. Lett* **66**, 52 (1995).
- [62] A. G. Cullis, D. J. Norris, T. Walther, M. A. Migliorato, and M. Hopkinson, *Phys.Rev. B* **66**, 081305(R) (2002).
- [63] Q. Gong, P. Offermans, R. Nötzel, P. M. Koenraad, and J. H. Wolter, *Appl. Phys. Lett* **85** (2004).
- [64] A. Lenz, R. Timm, H. Eisele, C. Hennig, S. K. Becker, R. L. Sellin, U. W. Pohl, D. Bimberg, and M. Dähne, *Appl. Phys. Lett.* **81**, 5150 (2002).
- [65] K. Pierz, Z. Ma, U. F. Keyser, and R. J. Haug, *J. Cryst. Growth* **249**, 477 (2003).
- [66] P. Offermans, P. Koenraad, J. Wolter, K. Pierz, M. Roy, and P. Maksym, *Physica E* **26**, 236 (2005).
- [67] Y. C. Kao, F. G. Celli, and H. Y. Liu, *J. Vac. Sci. Technol. B* **11**, 1023 (1993).
- [68] D. Granados and J. M. García, *Appl. Phys. Lett.* **82**, 2401 (2003).
- [69] L. G. Wang, P. Kratzer, M. Scheffler, and Q. K. K. Liu, *Appl. Phys. A* **73**, 161 (2001).
- [70] Z. R. Wasilewski, S. Fafard, and J. P. McCaffrey, *J. Cryst. Gr.* **201/202**, 1131 (1999).
- [71] E. Steimetz, T. Wehnert, H. Kirmse, F. Poser, J.-T. Zettler, W. Neumann, and W. Richter, *J. Cryst. Gr.* **221**, 592 (2000).
- [72] A. Lenz, H. Eisele, R. Timm, S. K. Becker, R. L. Sellin, U. W. Pohl, D. Bimberg, and M. Dähne, *Appl. Phys. Lett.* **85**, 3848 (2004).
- [73] J. L. Movilla, J. I. Climente, and J. Planelles, *J. Appl. Phys.* **94**, 4515 (2003).
- [74] J. M. García, T. Mankad, P. O. Holtz, P. J. Wellman, and P. M. Petroff, *Appl. Phys. Lett* **72**, 3172 (1998).
- [75] I. Hapke-Wurst, U. Zeitler, H. W. Schumacher, R. J. Haug, K. Pierz, and F. J. Ahlers, *Semicond. Sci. Technol.* **14**, L41 (1999).
- [76] A. S. G. Thornton, T. Ihn, P. C. Main, L. Eaves, and M. Henini, *Appl. Phys. Lett.* **73**, 354 (1998).
- [77] U. H. Lee, D. Lee, H. G. Lee, S. K. Noh, J. Y. Leem, and H. J. Lee, *Appl. Phys. Lett* **74**, 1597 (1999).

BIBLIOGRAPHY

- [78] F. Ferdos, S. Wang, Y. Wei, H. Sadeghi, Q. Zhao, and A. Larsson, *J. Cryst. Growth* **251**, 145 (2003).
- [79] N. Liu, J. Tersoff, O. Baklenov, A. L. H. Jr., and C. K. Shih, *Phys. Rev. Lett* **84**, 334 (2000).
- [80] O. Wolst, M. Kahl, M. Schardt, S. Malzer, and G. H. Dohler, *Phys. E.* **17**, 554 (2003).
- [81] D. Sarkar, H. P. van der Meulen, J. M. García, J. M. Becker, R. J. Haug, and K. Pierz, *Phys. Rev. B.* **71**, 081302(R) (2005).
- [82] P. Dawson, Z. Ma, K. Pierz, and E. O. Göbel, *Appl. Phys. Lett.* **81**, 2349 (2002).
- [83] T. S. Shamirzaev, A. M. Gilinksny, A. K. Bakarov, A. I. Toporov, D. A. Tenne, K. S. Zhuravlev, C. von Borczyskowski, and D. R. T. Zahn, *JETP Letters* **77**, 389 (2003).
- [84] O. Flebbe, H. Eisele, T. Kalka, F. Heinrichsdorff, A. Krost, D. Bimberg, and M. Dähne-Prietsch, *J. Vac. Sci Technol. B* **17**, 169 (1999).
- [85] T. Walther, A. G. Cullis, D. J. Norris, and M. Hopkinson, *Phys. Rev. Lett.* **86**, 2381 (2001).
- [86] E. Pehlke, N. Moll, A. Kley, and M. Scheffler, *Appl. Phys. A* **65**, 525 (1997).
- [87] P. Ballet, J. B. Smathers, and G. J. Salamo, *Appl. Phys. Lett* **75**, 337 (1999).
- [88] M. Roy and P. A. Maksym, *Phys. Rev. B* **68**, 235308 (2003).
- [89] L. R. C. Fonseca, J. L. Jimenez, J. P. Leburton, and R. M. Martin, *Phys. Rev. B* **57**, 4017 (1998).
- [90] I. Vurgaftman, J. R. Meyer, and L. R. Ram-Mohan, *J. Appl. Phys.* **89**, 5815 (2001).
- [91] W. P. Dumke, M. R. Lorenz, and G. D. Petit., *Phys. Rev. B.* **5**, 2978 (1972).
- [92] P. Lawaetz, *Phys. Rev. B.* **4**, 8460 (1971).
- [93] D. I. Westwood, M. L. Ke, F. Lelarge, F. Laruelle, and B. Etienne, *Surface Science* **352**, 802 (1996).
- [94] S.-H. Wei and A. Zunger., *Phys. Rev. B.* **60**, 5404 (1999).
- [95] J. M. Smith, P. A. Dalgarno, R. J. Warburton, A. O. Govorov, K. Karrai, B. D. Gerardot, and P. M. Petroff, *Phys. Rev. Lett.* **94**, 197402 (2005).

- [96] M. Bayer, A. Kuther, A. Forchel, A. Gorbunov, V. B. Timofeev, F. Schäfer, J. P. Reithmaier, T. L. Reinecke, and S. N. Walck, *Phys. Rev. Lett.* **82**, 1748 (1999).
- [97] A. Rastelli, E. Müller, and H. von Känel, *Appl. Phys. Lett.* **80**, 1438 (2002).
- [98] P. B. Joyce, T. J. Krzyzewski, P. H. Steans, G. R. Bell, J. H. Neave, and T. S. Jones, *Surf. Sci.* **492**, 345 (2001).
- [99] P. B. Joyce, T. J. Krzyzewski, G. R. Bell, and T. S. Jones, *Appl. Phys. Lett.* **79**, 3615 (2001).
- [100] M. Stoffel, U. Denker, G. S. Kar, H. Sigg, and O. G. Schmidt, *Appl. Phys. Lett.* **83**, 2910 (2003).
- [101] P. B. Joyce, T. J. Krzyzewski, G. R. Bell, B. A. Joyce, and T. S. Jones, *Phys. Rev. B* **58**, R15981 (1998).
- [102] L. Wendler, V. M. Fomin, and A. A. Krokhin, *Phys. Rev. B* **50**, 4642 (1994).
- [103] R. J. Warburton, C. Schäfflein, D. Haft, F. Bickel, A. Lorke, K. Karrai, J. M. García, W. Schoenfeld, and P. M. Petroff, *Nature* **405**, 926 (2000).
- [104] R. J. Warburton, C. Schulhauser, D. Haft, C. Schäfflein, K. Karrai, J. M. García, W. Schoenfeld, and P. M. Petroff, *Phys. Rev. B* **65**, 113303 (2002).
- [105] T. Raz, D. Ritter, and G. Bahir, *Appl. Phys. Lett.* **82**, 1706 (2003).
- [106] R. Blossey and A. Lorke, *Phys. Rev. E* **65**, 021603 (2002).
- [107] D. Granados, J. M. García, T. Ben, and S. I. Molina, *Appl. Phys. Lett.* **86**, 071918 (2005).
- [108] K. Shiraishi, *Appl. Phys. Lett.* **60**, 1363 (1992).

BIBLIOGRAPHY

List of main results

1. It is shown that X-STM enables the acquisition of images showing either electronic contrast or topographic contrast depending on the applied tip-sample voltage. This is confirmed by a calculation of the expected apparent height contrast of a heterojunction structure as a function of voltage.
2. The electronic contrast enables the determination of interface roughness and the structural changes during annealing of a digital alloy. It is shown that, depending on temperature, annealing can either lead to intermixing of the digital alloy or to an enhanced interface roughness and lateral composition modulation due to indium phase separation. These structural changes explain the observed changes in photoluminescence intensity after annealing.
3. It is shown that indium clustering during growth leads to unintentional softening of the barriers in a InGaAs/InAlAs quantum cascade laser structure.
4. The topographic contrast enables the determination of the strain field of a buried quantum dot by the local change in lattice constant around the quantum dot. It is shown that this strain field can be calculated using isotropic elasticity theory.
5. The topographic contrast also enables the determination of indium concentration of buried nanostructures by the outward relaxation of the cleaved surface. The outward relaxation is calculated using isotropic elasticity theory and compared with the measured relaxation in order to determine the indium concentration of buried nanostructures. It is shown that the extension to cubic elasticity theory leads to unrealistic results for the indium composition. The use of isotropic elasticity for the calculation of the outward relaxation is verified by direct counting of the indium atoms in wetting layers.
6. A detailed study of the capping process of quantum dots and the indium content of wetting layers shows that the formation of quantum dots and wetting layers depends on surface migration, strain-driven segregation and the dissolution of quantum dots during overgrowth.

7. In its initial stage, GaAs capping induces leveling of the quantum dots to drastically decrease their height. During continuous capping the quantum dot leveling is quenched when the quantum dots become buried. Both phenomena, driving and quenching of the quantum dot leveling take place on a similar time scale and are very sensitive to the GaAs growth rate and growth temperature.
8. We show new results for the composition variation in an InAs/AlAs dot and confirm the inverted trumpet-like indium distribution that previously has been assumed in InAs/GaAs quantum dots.
9. We show that the ground state photoluminescence energy of InAs/GaAs and InAs/AlAs quantum dots can be calculated based on the measured size, shape and composition of the quantum dots using a single band effective mass approach. We find that the large difference in the PL spectra and decay times of InAs/GaAs and InAs/AlAs quantum dots are explained by the structural properties of the dots.
10. We find that buried quantum rings show indium-rich asymmetric crater-like shapes which differ substantially from the ring-shaped islands on the surface of uncapped quantum ring structures. Our observation that such quantum craters have a smaller size and a larger height than the ring-shaped islands, offers an explanation for the observed discrepancies between the measured and theoretical values for the electronic radius and dipole moment of the quantum rings. Furthermore, we find that there might be a chance to observe Aharonov-Bohm-type oscillations for ensembles of buried quantum rings with radial dispersion as large as 10-20%.

Summary

In this thesis, cross-sectional scanning tunneling microscopy (X-STM) has been used to analyse the atomic-scale structural properties of a wide range of semiconductor nanostructures, like quantum wells, wires, dots and rings. Knowledge of the shape, size and composition of these nanostructures is essential in order to unravel the growth processes involved in the formation of these structures and to better understand their opto-electronic properties. The quantum cascade laser structure serves as an excellent example, since the wavelength is mainly determined by quantum confinement, i.e., by the thickness of the layers of the active region rather than by the band gap of the material. For this kind of structure, it is therefore important to have a proper knowledge of the atomic-scale properties like the thickness of the layers and the interface quality. We have used the electronic contrast observed by X-STM, between the well and barrier material of quantum cascade laser structures, to determine the interface roughness. It was found that indium clustering leads to a grading of the interfaces, which defies the use of digital grading in order to achieve a softening of the interfaces. Furthermore, the structural effects of rapid thermal annealing of digitally grown multiple quantum well laser structures were investigated.

Since the growth of three-dimensional self-assembled quantum dots and rings involves processes such as diffusion, segregation and intermixing, the accurate determination of their composition profiles is essential in order to understand their formation and opto-electronic properties. The composition of these structures and their wetting layers has been determined at the atomic scale by either counting of individual atoms, analysis of the relaxation of the cleaved surface or the lattice constant profile. The influence of partial capping, capping speed, capping temperature on the formation of quantum dot structures and wetting layers was investigated. We found that especially capping and a subsequent annealing can have a dramatic effect on the dot size and shape. In this respect, it was shown for the first time that buried quantum rings, which can be formed out of quantum dots by partial capping and subsequent annealing have an asymmetric indium-rich crater-like shape with a depression rather than an opening at the center.

SUMMARY

Nederlandse samenvatting

Dit proefschrift gaat over het gebruik van *cross-sectional scanning tunneling microscopy* (X-STM) voor het analyseren van de structurele eigenschappen, op de atomaire schaal, van een groot aantal halfgeleidernanostructuren, zoals kwantumputten, -draden, -druppels en -ringen. Kennis van de vorm, grootte en samenstelling van deze nanostructuren is van essentieel belang voor het ontrafelen van de groeiprocessen die optreden tijdens de formatie van deze structuren en voor een beter begrip van hun opto-elektronische eigenschappen. De kwantumcascadelaserstructuur is hier een goed voorbeeld van, omdat de golflengte van een dergelijke structuur met name bepaald wordt door de dikte van een groot aantal alternerende indium-aluminium-arseen en indium-gallium-arseen lagen en niet zozeer door een variatie in de samenstelling van het materiaal. Voor deze structuur, is het dus van groot belang om de werkelijke dikte en ruwheid van de lagen te meten. Met behulp van X-STM kan het elektronische contrast tussen de putten en de barrières van de kwantumcascadelaserstructuur zichtbaar gemaakt worden. Dit is gebruikt om de ruwheid van deze lagen te bepalen. Het samenklonteren van indium leidt tot minder scherpe overgangen tussen de kwantumput- en barrièrelagen, hetgeen een opzettelijke “verzachting” van deze overgangen ter verbetering van de opto-elektronische eigenschappen, overbodig maakt. Verder zijn de structurele effecten onderzocht van het kort verhitten van digitaal gegroeide kwantumput-laserstructuren ter verbetering van de optische eigenschappen.

Omdat de groei van driedimensionale zelfgeorganiseerde kwantumdruppels en -ringen gepaard gaat met processen zoals diffusie, segregatie en vermenging, is een nauwkeurige bepaling van hun samenstelling van wezenlijk belang om hun vorming en opto-elektronische eigenschappen te begrijpen. De atomaire samenstelling van deze structuren en de lagen waarop ze gevormd worden, is bepaald door middel van het direct tellen van de individuele atomen, analyse van de uitstulping van de dwarsdoorsnede van de gekliefde structuren, of de verandering in de afstand tussen de atomaire rijen van het kristal. De invloed van het gedeeltelijk overgroeien, de overgroeisnelheid en temperatuur op de formatie van kwantumdruppels en de lagen waarop ze gevormd worden is onderzocht. Met name overgroeien gevolgd door verhitten, kan een dramatisch effect hebben op de grootte en vorm van de kwantumdruppels. In dit opzicht, is voor het eerst aangetoond dat kwantumringen, die gevormd worden door kwantumdruppels gedeeltelijk te begraven en te verhitten, een asymmetrische, indiumrijke kratervorm hebben met

NEDERLANDSE SAMENVATTING

in het midden een bodem, in plaats van een opening zoals in het verleden werd aangenomen.

Acknowledgements

At this place I would like to thank everybody who has supported me during my PhD project. Special thanks go to the following people: Paul Koenraad, for his personal care and guidance. Paul's neverlasting enthusiasm and feedback has been very motivating. Without his contacts everywhere around the world, this work would not have been possible; Dominique Bruls, for teaching me the secrets of X-STM in such a gentle and patient way. He has been like a mentor to me. Furthermore, I enjoyed his coffee table stories a lot; Andrei Yakunin, because he was a very nice office mate and a good colleague; Jun He, for being such a close friend and swimming companion; Qian Gong, for our nice cooperation and computer related conversations; Najm Al-Hosiny, because it was very nice to have him in our group; Mervyn Roy, for all his calculations and help with abaqus; Vladimir Fomin, for his kindness and because I liked our weekly quantum ring sessions a lot; Dayong Zhou, for our collaboration on the quantum wires; Peter Nouwens, for his help with sample contacts and Joachim Wolter, for making my PhD project possible at all. I thank Niek Kleemans for the PL measurements on the quantum rings. I wish Niek and my colleague Cem Çelebi a lot of success and fun in their work. Also many thanks go to all other people I have collaborated with: Jin Dong Song, Mattias Beck, Thierry Aellen, Jérôme Faist, Klaus Pierz, Peter Maksym, Luke Wilson, Richard Green, John Davies, Daniel Granados, Jorge García, Vladimir Gladilin and Professor Devreese. Finally, I thank my fellow PhD's, students and other group members for making me feel at home in the group. Without them I wouldn't be the person I am today.

ACKNOWLEDGEMENTS

List of publications

Papers

Atomic-scale structure and photoluminescence of InAs quantum dots in GaAs and AlAs

P. Offermans, P.M. Koenraad, J.H. Wolter, K. Pierz, M. Roy, P.A. Maksym, submitted to Physical Review B (2005)

Formation of InAs wetting layers studied by cross-sectional scanning tunneling microscopy

P. Offermans, P.M. Koenraad, R. Nötzel, J.H. Wolter, K. Pierz, accepted for publication in Applied Physics Letters (2005)

Excited states of ring-shaped (InGa)As quantum dots in a GaAs/(AlGa)As quantum well

F. Pulizzi, D. Walker, A. Patane, L. Eaves, M. Henini, D. Granados, J. M. Garcia, V.V. Rudenkov, P.C.M. Christianen, J.C. Maan, **P. Offermans**, P. M. Koenraad, G. Hill, accepted for publication in Physical Review B (2005)

Atomic-Scale Structure of Self-Assembled In(Ga)As quantum rings in GaAs

P. Offermans, P.M. Koenraad, J.H. Wolter, D. Granados, J.M. Garcia, V.M. Fomin, V.N. Gladilin, J.T. Devreese, submitted to Applied Physics Letters (2005)

Relaxation of a Strained Quantum Well at a Cleaved Surface. Part II: Effect of Cubic Symmetry

John H. Davies, **Peter Offermans**, Paul M. Koenraad, accepted for publication in Journal of Applied Physics (2005)

Formation of InAs quantum dots and wetting layers in GaAs and AlAs analyzed by cross-sectional scanning tunneling microscopy

P. Offermans, P.M. Koenraad, J.H. Wolter, K. Pierz, M. Roy, P.A. Maksym, Physica E-Low-Dimensional Systems & Nanostructures 26, 236 (2005)

In(Ga)As sidewall quantum wires on shallow-patterned InP (311)A

D. Zhou, R. Nötzel, Q. Gong, **P. Offermans**, P.M. Koenraad, P.J. van Veldhoven, F.W.M. van Otten, T.J. Eijkemans, and J.H. Wolter, *J. Appl. Phys.* **97**, 063510 (2005)

Capping process of InAs/GaAs quantum dots studied by cross-sectional scanning tunneling microscopy

Q. Gong, **P. Offermans**, R. Notzel, P.M. Koenraad, J.H. Wolter, *Applied Physics Letters* **85**, 5697 (2004)

Formation of columnar (In,Ga)As quantum dots on GaAs(100)

J. He, R. Notzel, **P. Offermans**, P.M. Koenraad, Q. Gong, G.J. Hamhuis, T.J. Eijkemans, J.H. Wolter, *Applied Physics Letters* **85**, 2771 (2004)

InAs quantum dot and wetting layer formation in GaAs and AlAs analyzed by cross-sectional scanning tunneling microscopy

P. Offermans, P.M. Koenraad, J.H. Wolter, K. Pierz, M. Roy, P.A. Maksym *Physics of Low-Dimensional Structures* **1-2**, 1 (2004)

Digital alloy interface grading of an InAlAs/InGaAs quantum cascade laser structure studied by cross-sectional scanning tunneling microscopy

P. Offermans, P.M. Koenraad, J.H. Wolter, M. Beck, T. Aellen, J. Faist, *Applied Physics Letters* **83**, 4131 (2003)

Annealing of InGaAlAs digital alloy studied with scanning-tunneling microscopy and filled-states topography

P. Offermans, P.M. Koenraad, J.H. Wolter, J.D. Song, J.M. Kim, S.J. Bae, Y.T. Lee, *Applied Physics Letters* **82**, 1191 (2003)

Real-space measurement of the potential distribution inside organic semiconductors

M. Kemerink, **P. Offermans**, J.K.J. van Duren, P.M. Koenraad, R.A.J. Janssen, H.W.M. Salemink, J.H. Wolter, *Physical Review Letters* **88**, 096803 (2002)

Measuring the potential distribution inside soft organic semiconductors with a scanning-tunneling microscope

M. Kemerink, **P. Offermans**, P.M. Koenraad, J.K.J. van Duren, R.A.J. Janssen, H.W.M. Salemink, J.H. Wolter, *Physica E-Low-Dimensional Systems & Nanostructures* **13**, 1247 (2002)

Oral conference presentations

Atomic-scale structure and formation of self-assembled In(Ga)As quantum rings

P. Offermans, P.M. Koenraad, J.H. Wolter, D. Granados, J.M. Garcia, V.M. Fomin, V.N. Gladilin, J.T. Devreese, invited presentation by P. Offermans and

Proceedings of the 12th International Conference on Modulated Semiconductor Nanostructures, July 10–15 2005, Albuquerque, New Mexico

Determination of the indium composition of InAs quantum dots and wetting layers on GaAs and AlAs by cross-sectional scanning tunneling microscopy

P. Offermans, P. M. Koenraad, T. Mano, Q. Gong, R. Nötzel, J. H. Wolter, K. Pierz, oral presentation by P. Offermans and Proceedings of the 3rd International Conference on the subject of quantum dots (QD2004), May 10–13 2004, Banff, Canada, *Physica E-Low-Dimensional Systems & Nanostructures* **26**, 236 (2005)

Digital alloy InGaAs/InAlAs laser structures studied by cross-sectional scanning tunneling microscopy

P. Offermans, P.M. Koenraad, J.H. Wolter, J.D. Song, J.M. Kim, S.J. Bae, Y.T. Lee, M. Beck, T. Aellen, J. Faist, oral presentation by P. Offermans and Proceedings of the 12th International Conference on Scanning Tunneling Microscopy/Spectroscopy and Related Techniques, July 21–25 2003, Eindhoven University of Technology, Eindhoven, The Netherlands, 677 (2003)

Cross-sectional STM on InGaAs/InAlAs laser structures

P. Offermans, P.M. Koenraad, J.H. Wolter, J.D. Song, J.M. Kim, S.J. Bae, Y.T. Lee, M. Beck, T. Aellen, J. Faist, oral presentation by P. Offermans and proceedings of the 13th International Conference on Microscopy of Semiconducting Materials, March 31–April 3 2003, University of Cambridge, Cambridge, England, Institute of Physics Conference Series, 653 (2003)

Other conference contributions

The Aharonov-Bohm effect in self-assembled InGaAs/GaAs quantum rings

V.M. Fomin, V.N. Gladilin, J.T. Devreese, **P. Offermans**, P.M. Koenraad, J.H. Wolter, D. Granados, J.M. García, submitted to the American Physical Society March Meeting, March 21–25, 2005, Los Angeles, California, USA

The Aharonov-Bohm effect in self-assembled InGaAs/GaAs quantum rings

V.M. Fomin, V.N. Gladilin, J.T. Devreese, **P. Offermans**, P.M. Koenraad, J.H. Wolter, D. Granados, J.M. García, submitted to the 16th International Conference on Electronic Properties of Two-Dimensional Systems, July 10–15, 2005, Albuquerque, New Mexico, USA

InGaAs-AlAsSb Quantum Cascade Lasers Emitting at 4.4 μm

D.G. Revin, L.R. Wilson, E.A. Zibik, R.P. Green, J.W. Cockburn, M.J. Steer, R.J. Airey, M. Hopkinson, **P. Offermans**, P.M. Koenraad, J.H. Wolter, submitted to the International Conference on Lasers and Electro-Optics, May 22–27, 2005, Baltimore, Maryland, USA

MOVPE grown quantum cascade lasers: performance and structural perfection

R.P. Green, L.R. Wilson, D.G. Revin, E.A. Zibik, and J.W. Cockburn, **P. Offermans**, P.M. Koenraad, J.H. Wolter, C. Pfügl, W. Schrenk, G. Strasser, C.M. Tey, A.B. Krysa, J.S. Roberts and A.G. Cullis, submitted to the International Conference on Lasers and Electro-Optics, May 22–27, 2005, Baltimore, Maryland, USA

Single Mode Performance and Structural Quality of MOVPE grown InP based Quantum Cascade Lasers

R.P. Green, L.R. Wilson, D.G. Revin, E.A. Zibik, J.W. Cockburn, **P. Offermans**, P.M. Koenraad, J.H. Wolter, C. Pfügl, W. Schrenk, G. Strasser, C.M. Tey, A.B. Krysa, J.S. Roberts and A.G. Cullis, submitted to the 17th International Conference on Indium Phosphide and Related Materials, May 8–12, 2005, Glasgow, Scotland, UK

Intermixing, decomposition and segregation during InAs dot formation on GaAs and AlAs analyzed by cross-sectional STM

P. Offermans, P.M. Koenraad, T. Mano, Q. Gong, R. Nötzel, J.H. Wolter, K. Pierz, D.G. Ruiz, D. Granados, J. Garcia, M. Roy, and P.A. Maksym, Proceedings of the 12th Int. Symp. “Nanostructures: Physics and Technology”, St. Petersburg, Russia, 229 (2004)

Modeling of the magnetization behavior of realistic self-organized InAs/GaAs quantum craters as observed with cross-sectional STM

V.M. Fomin, V.N. Gladilin, J.T. Devreese, **P. Offermans**, P.M. Koenraad, J.H. Wolter, Proceedings of the 27th International Conference on the Physics of Semiconductors, July 26–30, 2004, Flagstaff, Arizona

Simulation of XSTS imaging of self-assembled quantum dot electronic states

M. Roy, P.A. Maksym, D. M. Bruls, **P. Offermans**, P. M. Koenraad, Proceedings of the 12th International Conference on Scanning Tunneling Microscopy/Spectroscopy and Related Techniques, July 21–25 2003, Eindhoven University of Technology, Eindhoven, The Netherlands, 707 (2003)

Composition profiling of III–V nanostructures using cross-sectional STM

P.M. Koenraad, D.M. Bruls, **P. Offermans**, J.H. Davies, J.H. Wolter, Proceedings of the 7th International Conference on Nanometer Scale Science and Technology and 21st European Conference on Surface Science (NANO-7/ECOSS-21), Malmo, Sweden, FR-R-002 (2002)

The STM as a tool to measure the potential distribution inside soft organic semiconductors

M. Kemerink, **P. Offermans**, J.K.J. van Duren, R.A.J. Janssen, P.M. Koenraad, H.W.M. Salemink, and J.H. Wolter, Proceedings of the 11th International Conference on STM/Spectroscopy and Related Techniques, 15–20 July 2001, Vancouver, Canada 106, (2001)

Curriculum vitae

Peter Offermans

born 20 September 1977 in Heerlen, the Netherlands

1989–1995 *Secondary education*, Gymnasium B, Bisschoppelijk College te Sittard

1995–2001 *Applied Physics*, Eindhoven University of Technology

Internal project, Eindhoven University of Technology, Physics of Nanostructures, "Labwindows programmatuur voor de MOKE opstelling"

External project, University of California San Diego, Department of Applied Mechanics and Engineering Science, "Oscillations of a neutrally buoyant sphere in a linearly stratified fluid"

Master project, Eindhoven University of Technology, Semiconductor Physics, "Scanning tunneling spectroscopy study of the charge transport properties of thin conjugated polymer films"

2001–2005 *PhD*, Eindhoven University of Technology, COBRA Inter-University Research Institute, Semiconductor Physics